UNIVERSITÀ DEGLI STUDI DI TRIESTE

DIPARTIMENTO DI FISICA

Corso di Laurea Magistrale in Fisica

Curriculum in Fisica della Materia Condensata

Noise Correlation Spectroscopy for Impulsive Stimulated Raman Scattering

Spettroscopia a correlazione di fluttuazioni applicata allo scattering Raman impulsato stimolato

Candidato:
FILIPPO GLEREAN

Relatore:
Prof. DANIELE FAUSTI

Correlatore:
Dott.ssa GIORGIA SPARAPASSI

Anno Accademico 2016-2017

"*Allegro, sicuro, ardito.*"

Saggezza familiare

Abstract

Coherent optical phonons in bulk solid systems play a crucial role in understanding and designing light-matter interactions. Optical excitation of coherent lattice vibration in transparent materials is commonly described by impulsive stimulated Raman scattering (ISRS).
The central idea of the proposed *Noise Correlation Spectroscopy* (NCS) is to use ISRS to imprint in ultrashort light pulses a statistical correlation between different spectral components. A statistical analysis on a repeated set of single shot measurements will provide the clear signature of the light-matter interaction, while allowing to identify and discard correlations intrinsic to the laser source. Spectral resolution is not limited by the pulse bandwidth, but on the spectral profile of the introduced noise. Temporal resolution of the experiment is solely determined by the pulse duration.
This thesis is aimed at a proof of principle of the NCS performing measurements on an α-quartz sample. A preliminary characterization of the system properties is also achieved through pump&probe frequency-resolved measurements and the development of theoretical models.

Contents

Chapter 1

Introduction

The development of femtosecond lasers brought entirely new possibilities into the practice of time-resolved vibrational spectroscopy, enabling to conduct observations on time scales that are not only shorter than vibrational lifetimes or dephasing times, but shorter than individual vibrational oscillation periods.
The displacement of the atoms along the vibrational eigenmodes of a crystal can be chaotic, due to thermal disorder, or can be characterized by a precise correlation between all the atomic positions. When all the atoms in a crystal oscillate in phase, they constitute a collective excitation commonly dubbed *coherent phonon*.
The propagation of light pulses in solids is accompained by intense THz lattice vibrations, showing a high degree of spatial and temporal coherence. It is therefore possible, in principle, to monitor materials and molecules at various stages of vibrational distortion.

The most common experiment on coherent phonons is the pump& probe one. It involves two ultrashort (femtoseconds/picoseconds long) laser pulses. The stronger *pump* pulse creates a vibrational wave which perturbs the weaker *probe* pulse that follows behind. The effects on the probe as a function of the time-delay between the two pulses are measured. In this way the dependence on the phase of the vibration excited by the pump is investigated.

Owing to the Heisenberg uncertainty principle, the ultrashort pulses required for the pump&probe measurement are characterized by a broad bandwidth. The wide spectrum of modes of the radiation is a fundamental requirement for the excitation to take place. In fact, the involved process is the Impulsive Stimulated Raman Scattering, which results from the coupling between two photons of different energy.
Moreover, the multimode nature of the pulses allows to improve the pump&probe approach performing frequency resolved measurements [1].

Impulsive Stimulated Raman Scattering

Impulsive Stimulated Raman Scattering (ISRS) is a process through which excitation of coherent lattice or molecular vibrations take place whenever a sufficiently short laser pulse passes through a Raman-active solid or molecular liquid or gas. It is therefore a generally important aspect of ultrashort-pulse interactions with matter.

A general Raman interaction is an inelastic scattering through which a photon of frequency ω_1 is annihilated and a new one is created at ω_2 (fig. 1.1a). If $\omega_2 - \omega_1 = \Omega > 0$ a phonon of frequency Ω is created and the radiation loses energy (Stokes process). Conversely, if $\omega_2 - \omega_1 = -\Omega$ a phonon is destroyed (Anti-Stokes process). Thus, Raman process conserves the photon number, but not their energy.

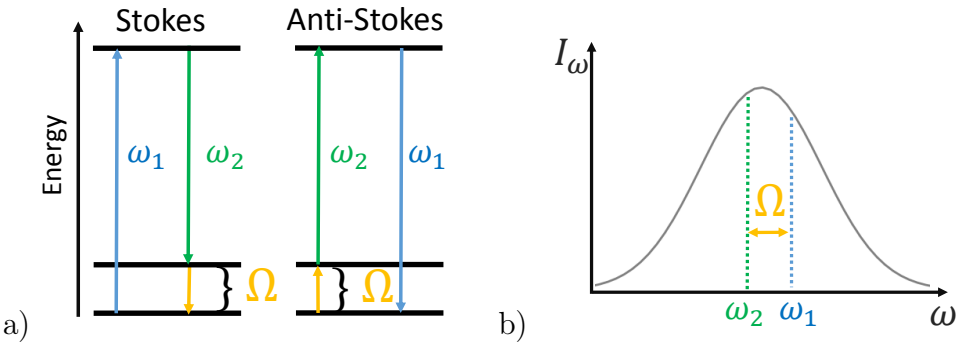

Figure 1.1: Example of a pair of frequency components contributing to ISRS.
a) Relation between photon (ω_1,ω_2) and excitation (Ω) frequencies.
b) Distribution of the modes inside the pulse bandwidth.

The stimulated character of Raman processes pertains to the way the resonance is created. The spontaneous (low-efficiency) case involves a single off-resonance field. In the stimulated one, instead, the Raman active mode is driven into resonance by two incident (off-resonance) fields tuned such as their energy difference matches the vibrational one ($|\omega_2 - \omega_1| = \Omega$).
In the impulsive case, stimulated scattering occurs not through coupling between two discrete frequencies, but among the continuous distribution of Fourier components within the spectral bandwidth of the ultrashort pulse. Since the pulse duration is less than the vibrational period, the spectral bandwidth of the pulse necessarily exceeds the vibrational frequency so that many frequency components are available to play the roles of ω_1 and ω_2 (fig. 1.1b).

Due to the stimulated nature of ISRS, the scattered intensity of a single mode ω is a function of the incident fields at $\omega \pm \Omega$. As a consequence

of this, correlations between the frequencies differing by the vibrational one are introduced. In this thesis we discuss the possibility to retrieve spectroscopic information through the statistical analysis of these correlations. Namely, we discuss the *Noise Correlation Spectroscopy*.

Noise Correlation Spectroscopy

Obtaining the Raman modes spectrum through a pump&probe measurement requires a scan over the delay between the two pulses. The probe transmittivity recorded is typically modulated at the vibrational frequency, which is then Fourier transformed. A complete Raman spectrum can be collected at a fixed pump&probe delay performing a scan in the energy difference between two distinct input fields (Coherent Raman Scattering [2]). However, in this setting the energy resolution is limited by their bandwidth. Consequently, this approach is unsuitable for ultrafast time-resolved studies, because to the short pulse duration correspond a broad bandwidth. In order to overcome this difficulty, we propose to develop a *Noise Correlation Spectroscopy* (NCS). We do this refering also to the work of other groups [3][4], which recently pursued a very similar approach.
The ISRS introduces correlations between pairs of frequencies comprised in the bandwidth of ultrashort light pulses. In particular, between those whose energy difference resonate with a low-energy Raman mode. The aim of NCS is to retrieve the information about the excitations of the considered sample, performing a statistical analysis of these correlations.

The fundamental NCS data are sets of repeated single-shot frequency-resolved intensity spectra. These are collected for the transmitted pulse together with a copy of the relative incident one. The latter is particularly useful to analyze the source correlations, so as to discriminate the interaction features only.
For each couple of frequencies, the correlation coefficient is calculated on the datasets. It quantifies how much the intensities of two modes are dependent from each other, analyzing the consequences of a random fluctuation on the considered mode onto the others. Actually, as highlighted by the name, noise has a crucial role in NCS and it will be deeply discussed in this thesis. For the moment, we help the intuition reporting in fig. 1.2 a schematic example of how a localized fluctuation in the incident pulse allows to reveal the relative correlations in the transmitted one.

In this thesis we discuss the NCS from both theoretical and experimental point of view. In order to describe the processes involved, in par-

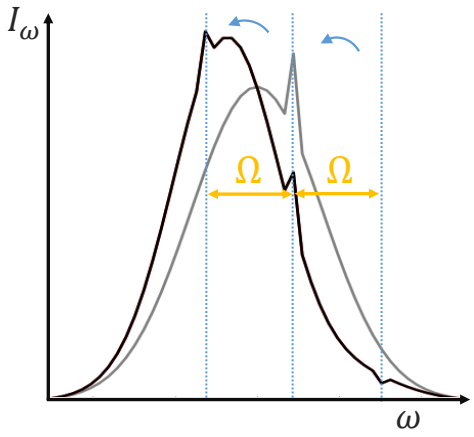

Figure 1.2: Working principle of Noise Correlation Spectroscopy.
A localized fluctuation in the incident pulse (grey) reflects in distinguishable features at the frequencies correlated by the ISRS process in the transmitted one (black). In particular in the present Stokes configuration, the positive fluctuation stimulates depletion of the high frequency mode and emission in the low frequency one.

ticular the ISRS, a classical and a quantum model of the photon-phonon interaction is developed. Basing on the models numerical simulations of the NCS results are implemented.
These are supported by experimental test measurements on α-quartz. A preliminary characterization of the quartz sample is also performed with pump&probe frequency-resolved measurements.

Reading Guide

The thesis is structured in the following way.

- In chapter 2 we model in a both classic and quantum formalism the light-vibration excitation and interaction processes. The starting point is the model of the driven harmonic oscillator. (A detailed discussion of it is reported in appendix A)

- Chapter 3 is dedicated to the description of the experimental setup specifically developed in the *T-Rex* laboratory at Elettra Sincrotrone Trieste. It enables us to perform pump&probe frequency-resolved single-shot measurements of both incident and transmitted pulse.

- The result of the characterization of the system through pump&probe frequency-resolved measurements are presented in chapter 4.
  In the first part, literature about the employed quartz sample is

presented. Then, with reference to these informations, the experimental results are reported and discussed. The Raman spectrum of quartz is studied by means of Fourier Analysis. We focus on the distinguishable spectral effects and to the symmetry properties of the various observable modes. In the end, also a study as a function of the pulse duration is performed.

- In chapter 5 we develop the NCS. Firstly, we define the statistical analysis employed. Then, numerical simulations of the NCS results are implemented. Various typologies of intensity fluctuations, including intrinsic source correlation, and the sample related ISRS process are simulated. Results from the test measurements on quartz are presented and compared to the simulations.

- In the end, we discuss the conclusions and the perspectives of this novel method proposed.

Chapter 2

Theory of Photon-Phonon Raman Interaction

In our experiment ultrashort laser pulses interact with the phonons present in an examined sample. The light pulses have a wide multimode frequency spectrum. Two modes of the radiation can interact in the sample if their energy difference matches one of the present phonons. Precisely, this happens through Impulsive Stimulated Raman Scattering. It consists in the distruction of a photon of frequency ω and the creation of one of frequency $\omega \pm \Omega$, where Ω is the one of the distructed/created phonon.

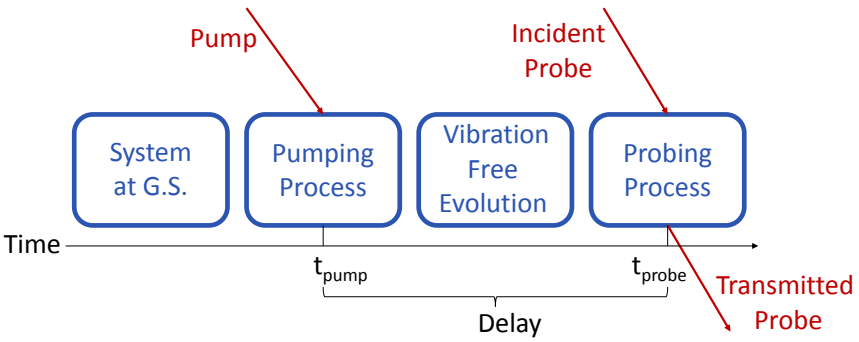

Figure 2.1: Scheme of a standard pump&probe experiment in transmission configuration.

We study the ISRS phonon-photon interaction perfoming a pump& probe experiment (fig. 2.1). A first intense pulse, the pump, excites collective atomic vibrations in the sample lattice, which initially were in the ground state. The presence of these vibrational modes periodically modulates the sample structure and, consequently, also the effects relative to light interaction. These are observed employing another (less intense)

ultrashort pulse, the probe, which is measured in transmission. In particular, the time dependence is studied as a function of the controlled delay between the pump and probe pulse.

In this chapter we build the theory useful to describe the interaction of the ultrashort pulses with the phonons of the considered sample. Firstly, we treat our system in a classical way. We describe the light-matter interaction exploiting the driven harmonic oscillator formalism and Maxwell equations.

In the end, we translate the discussion into a quantum language. It is useful to understand the quantum nature of ISRS process.

2.1 Phonon-Photon Interaction in the Classical Formalism

In this section, we describe our system by means of classical fields. The vibrational modes are considered harmonic oscillators, which are driven by the force exerted by the pulse electromagnetic waves. In 2.1.1, we explain in detail the link between force and electric field.
The interaction of the electric field in the sample is described by the polarization field. It is a function of the polarizability, which is modulated by the vibration excited in the sample. Taking this into account in the Maxwell formalism, we can finally evaluate the effects on the transmitted pulses.

2.1.1 Electric Field Driving Force

The presence of the pulse electric field $\mathbf{E}$ induces a polarization field $\mathbf{P}$ in the sample, which is ruled by the expression:

$$P_i = \alpha_{ij} E^j \tag{2.1}$$

where α_{ij} is the polarizability tensor.
The energy required to establish the polarization in the dipole approximation is

$$U^{int} = -\mathbf{P} \cdot \mathbf{E} = -\alpha_{ij} E^j E^i. \tag{2.2}$$

The polarizability is a quantity sensitive to the presence of the phononic excitations. We take account of this performing a perturbative expansion

in the vibrational amplitude $\mathbf{Q}$, around the equilibrium polarizability α_{0ij}. The resulting expression is

$$\alpha_{ij}(Q^k) = \alpha_{0ij} + \Big(\frac{\delta\alpha}{\delta Q^k}\Big)|_{Q^k=0}{}_{ij} Q^k \tag{2.3}$$

where only terms up to first order are considered.

The force is minus the spatial derivative of the potential energy. Hence, using the two previous equation we write it as

$$F_k = -\frac{dU^{int}}{dQ^k} = (\frac{\delta\alpha}{\delta Q})_{0\ ij,k} E^i E^j \tag{2.4}$$

and so we obtain the force as a function of the generic electric field.
In our experiment, we employ ultrashort-multimode pulses. Their field can be generally expressed as linear combination of plane waves. We write a sum over the set of modes of the radiation of frequency ω

$$\mathbf{E}(t,z) = \sum_\omega \mathbf{E}_\omega e^{-i\omega(t-\frac{n}{c}z)} + c.c. \tag{2.5}$$

where a beam propagating along the z direction is considered. We simplify the notation defining the variable $t' = t - \frac{n}{c}z$.

$$\mathbf{E}(t') = \sum_\omega \mathbf{E}_\omega e^{-i\omega t'} + c.c. \tag{2.6}$$

Using the last relation, the force explicitly results

$$F_k(t') = (\frac{\delta\alpha}{\delta Q})_{0\ ij,k} (\sum_\omega E^i_\omega e^{-i\omega t'} + c.c)(\sum_{\omega'} E^j_{\omega'} e^{-i\omega' t'} + c.c) \tag{2.7}$$

Considering the driven harmonic oscillator, the most effective contributions are those resonant with the proper frequency. We take this in account posing the condition $\omega' = \omega \pm \Omega$, where Ω is the phonon frequency. Applying it we are left with

$$F_k(t') = (\frac{\delta\alpha}{\delta Q})_{0\ ij,k} \sum_\omega \Big(E^i_\omega E^j_{\omega-\Omega} e^{-i\Omega t'} + E^i_\omega E^j_{\omega+\Omega} e^{+i\Omega t'} + c.c.\Big) \tag{2.8}$$

Considering real Fourier components for the electric field we can rewrite the force.

$$\begin{aligned} F_k(t') &= (\frac{\delta\alpha}{\delta Q})_{0\ ij,k} \Big(\sum_\omega E^i_\omega (E^j_{\omega-\Omega} + E^j_{\omega+\Omega})\Big)(e^{-i\Omega t'} + e^{+i\Omega t'}) \\ &= 2(\frac{\delta\alpha}{\delta Q})_{0\ ij,k} \Big(\sum_\omega E^i_\omega (E^j_{\omega-\Omega} + E^j_{\omega+\Omega})\Big) \cos(\Omega t') \end{aligned} \tag{2.9}$$

From the last expression, we see that the resulting force is a sinusoidal function. It has frequency Ω and we define its amplitude f_k.

$$f_k = 2(\frac{\delta\alpha}{\delta Q})_{0\,ij,k}\Big(\sum_{\omega} E^i_{\omega}(E^j_{\omega-\Omega} + E^j_{\omega+\Omega})\Big) \tag{2.10}$$

2.1.2 ISRS Pumping Process

The ultrashort pulses employed have a wide spectrum of frequencies. Among them, the electric fields, whose frequency difference matches the phonon one, couple themselves and generate a force oscillating in resonance with the vibrational mode. Namely, this is the ISRS process.
The pump process can be described as the effect on an harmonic oscillator, initially at rest, resonantly driven at the phonon frequency Ω by the pump pulse.

The differential equation ruling the process is

$$\ddot{\mathbf{Q}}(t') + \Omega^2\mathbf{Q}(t') = \mathbf{F}(t') \tag{2.11}$$

where we used the combined temporal and spatial variable $t' = t - \frac{n}{c}z$.

In Appendix A, we find the solution which describes our configuration. We consider a system with proper frequency Ω and initial amplitude $\mathbf{Q}_0$. A sinusoidal force (frequency Ω, amplitude $\boldsymbol{f}$) is applied for a short time interval τ to it. The obtained expression for the oscillator amplitude after the interaction is

$$\mathbf{Q}(t') = \sqrt{(\mathbf{Q}_0 - \frac{\tau\boldsymbol{f}}{2\Omega})^2 + \frac{\mathbf{Q}_0\boldsymbol{f}\tau}{\Omega}\Big(1 - \sin(\Delta\phi)\Big)}\cos\Big(\Omega t' + \Phi\Big) \tag{2.12}$$

where $\Delta\phi$ is the phase difference between initial oscillation $\mathbf{Q}(t')$ and force $\mathbf{F}(t')$, Φ is the new phase acquired by the phonon after the interaction. Its explicit expression is reported in the appendix.
In our case, for the description of the pump-photon interactions the specific quantities are

$$\begin{cases} Q_{0k} = 0 \\ f_k^{pump} = 2(\frac{\delta\alpha}{\delta Q})_{0\,ij,k}\Big(\sum_{\omega} E^i_{\omega}(E^j_{\omega-\Omega} + E^j_{\omega+\Omega})\Big) \end{cases} \tag{2.13}$$

where we used the solution of eq. 2.10.
As a consequence of this, the effect of interaction on the phonon oscillation is

$$Q_k(t') = \frac{\tau f_k^{pump}}{2\Omega} \sin(\Omega t') \tag{2.14}$$

and we underline that we set a sine function, because the instant of maximum cosine force is the one when to the vibration, initially at rest, is imparted the maximum momentum. Therefore, we can describe this with the relation

$$\Delta\phi_{pump-vib} = \phi_{pump} - \phi_{vib} = \pi/2. \tag{2.15}$$

In order to describe the dynamical response of the system we turn to eq. 2.3, which states the polarizability dependence on the vibrational amplitude. Inserting there the expression obtained for $\mathbf{Q}$, we get the explicit modulation of polarizability after the pump process.

$$\begin{aligned} \alpha_{ij}(t') &= \alpha_{0ij} + (\frac{\delta\alpha}{\delta Q})_{0\ ij,k} Q^k(t') \\ &= \alpha_{0ij} + (\frac{\delta\alpha}{\delta Q})_{0\ ij,k} \frac{\tau f_{pump}^k}{2\Omega} \sin(\Omega t') \end{aligned} \tag{2.16}$$

We conclude that the excitation of a vibrational mode results in an oscillation of the polarizability around the equilibrium value α_0, at the phonon frequency Ω. Inserting the complete expression for the force amplitude, we can obtain explicitly the dependence on the pump electric field components

$$\begin{aligned} \alpha_{ij}(t') &= \alpha_{0ij} + \frac{\tau}{\Omega}(\frac{\delta\alpha}{\delta Q})_{0\ ij,k}{}^{k}(\frac{\delta\alpha}{\delta Q})_{0\ lm,} \Big(\sum_{\omega} E_{\omega}^{l}(E_{\omega-\Omega}^{m} + E_{\omega+\Omega}^{m}) \Big) \sin(\Omega t') \\ &= \alpha_{0ij} + \frac{\tau}{\Omega}(\frac{\delta\alpha}{\delta Q})_{0\ ij,lm}^{2} \Big(\sum_{\omega} E_{\omega}^{l}(E_{\omega-\Omega}^{m} + E_{\omega+\Omega}^{m}) \Big) \sin(\Omega t') \end{aligned} \tag{2.17}$$

where we use the pump electric field written as in eq. 2.6 and introduce the notation $(\frac{\delta\alpha}{\delta Q})_{0\ ij,lm}^{2}$ for the resulting fourth rank non-linear polarizability tensor.

2.1.3 Polarizability Modulation Probing

In the previous discussion, we have formalized the pump process. We have seen that vibrational modes are excited by the pump pulse.
The vibration displaces the ions in the lattice around their equilibrium

position. Owing to this, a modulation in the polarizability is present. We explicitly quantified its temporal and spatial dependence in eq. 2.16. In a pump&probe experiment we test these properties of the perturbed sample with another light-pulse, which impinges it at a controlled delay with respect to the pump. We detect the traces of the interaction process in the transmitted intensity spectrum.

In the following we analytically derive the spectral effects on the probe, which are the result of the pulse propagation through our pumped sample. We do it using Maxwell equations for dielectric materials. In particular we explicit the polarization field dependence on the modulating polarizability.

We consider the first, third and fourth Maxwell's equations:

$$\begin{cases} \nabla \cdot \mathbf{E} = \frac{\rho}{\epsilon_0} & \text{(I)} \\ \nabla \times \mathbf{E} = -\frac{\partial \mathbf{B}}{\partial t} & \text{(III)} \\ \nabla \times \mathbf{B} = \mu_0 \mathbf{J} + \frac{1}{c^2}\frac{\partial \mathbf{E}}{\partial t} & \text{(IV)} \end{cases} \tag{2.18}$$

where $\mathbf{E}$, $\mathbf{B}$ are electric and magnetic field of the probe pulse, ρ, $\mathbf{J}$ charge and current in the sample.
We perform the rotor of the third equation, insert the fourth and simplify the laplacian considering the system neutral ($\rho = 0$).

$$\begin{aligned} \nabla \times \nabla \times \mathbf{E} = \nabla(\nabla \cdot \mathbf{E}) - \nabla^2 \mathbf{E} = -\frac{\partial}{\partial t}(\nabla \times \mathbf{B}) = \\ = -\nabla^2 \mathbf{E} = -\mu_0 \frac{\partial \mathbf{J}}{\partial t} - \frac{1}{c^2}\frac{\partial^2 \mathbf{E}}{\partial t^2} \end{aligned} \tag{2.19}$$

The current is function of the polarization field $\mathbf{P}$. Thus, we consider the relations $\mathbf{J} = \frac{\partial \mathbf{P}}{\partial t}$ and $\mathbf{P} = \alpha \mathbf{E}$, where α is the polarizability.

$$\begin{aligned} \nabla^2 \mathbf{E} = \mu_0 \frac{\partial^2 \mathbf{P}}{\partial t^2} + \frac{1}{c^2}\frac{\partial^2 \mathbf{E}}{\partial t^2} = \\ = \mu_0 \frac{\partial^2 \alpha \mathbf{E}}{\partial t^2} + \frac{1}{c^2}\frac{\partial^2 \mathbf{E}}{\partial t^2} \end{aligned} \tag{2.20}$$

Keeping in mind the perturbative expansion of the polarizability (eq. 2.3, for simplicity we consider only the scalar formulation),

$$\alpha(Q) = \alpha_0 + (\frac{\delta \alpha}{\delta Q})_0 Q \tag{2.21}$$

we obtain

$$\nabla^2 \mathbf{E} = \mu_0 \alpha_0 \frac{\partial^2 \mathbf{E}}{\partial t^2} + \frac{1}{c^2}\frac{\partial^2 \mathbf{E}}{\partial t^2} + \mu_0 (\frac{\delta \alpha}{\delta Q})_0 \frac{\partial^2 Q \mathbf{E}}{\partial t^2}. \tag{2.22}$$

We collect together the two terms with the second-order derivative of the electric field. We rewrite the sum of their coefficients considering the relations for polarizability $\alpha_0 = \epsilon_0\chi$ and refractive index $n = \sqrt{1+\chi}$, where χ is the dielectric susceptibility.

$$\frac{1}{c^2} + \mu_0\alpha_0 = \frac{1}{c^2}(1 + \frac{\alpha_0}{\epsilon_0}) = \frac{1}{c^2}(1+\chi) = \frac{n^2}{c^2} \tag{2.23}$$

Taking this into account, we get the propagation equation in the form

$$\nabla^2\mathbf{E}(t') - \frac{n^2}{c^2}\frac{\partial^2\mathbf{E}(t')}{\partial t^2} = \mu_0(\frac{\delta\alpha}{\delta Q})_0\frac{\partial^2 Q(t')\mathbf{E}(t')}{\partial t^2} \tag{2.24}$$

where the typical equation for linear dielectrics is corrected by the term on the right, which introduces the non-linear effects.
In our specific case, $\mathbf{E}$ and Q are both functions of the variable $t' = t - \frac{n}{c}z$. Moreover, the probe pulse impinges with variable delay with respect to the starting time of the phonon oscillation. We consider this explicitly adding the term $\Delta t = t_{probe} - t_{pump}$.

$$\nabla^2\mathbf{E}(t') - \frac{n^2}{c^2}\frac{\partial^2\mathbf{E}(t')}{\partial t^2} = \mu_0(\frac{\delta\alpha}{\delta Q})_0\frac{\partial^2 Q(t'+\Delta t)\mathbf{E}(t')}{\partial t^2} \tag{2.25}$$

We now start to deeply analyze the last equation in order to understand the effects it describes.
Firstly, we evaluate the second-order derivative on the right side.

$$\nabla^2\mathbf{E} - \frac{n^2}{c^2}\frac{\partial^2\mathbf{E}}{\partial t^2} = \mu_0(\frac{\delta\alpha}{\delta Q})_0\Big(Q\frac{\partial^2\mathbf{E}}{\partial t^2} + \frac{\partial Q}{\partial t}\frac{\partial\mathbf{E}}{\partial t} + \mathbf{E}\frac{\partial^2 Q}{\partial t^2}\Big) \tag{2.26}$$

Analogously as done before, we collect the terms with the second-order derivative of the electric field. In this way we define a new refraction index $\tilde{n}$:

$$\tilde{n}^2(\Delta t) = n^2 + c^2\mu_0(\frac{\delta\alpha}{\delta Q})_0 Q(\Delta t) \tag{2.27}$$

which oscillates in time around the equilibrium value, following the phonon modulation. In the last expression, we assumed a reference frame in which the pump excitation starts at $t' = 0$.
The refraction index rules through Fresnel equations the transmittivity and reflectivity of the material. In case of normal incidence, the transmittivity t (ratio between transmitted and incident field) is:

$$\mathrm{t}(\Delta t) = \Big|\frac{\mathbf{E}^T}{\mathbf{E}^I}\Big| = \frac{2}{1+\tilde{n}(\Delta t)} \tag{2.28}$$

Therefore, controlling the pump&probe delay Δt, the probe pulse is sensitive to different refractive conditions. The result is an oscillation of the transmitted intensity in phase with the vibrational amplitude, around the unperturbed value. We show it more clearly considering that $\tilde{n} - n << n$ and performing a Taylor expansion of the transmittivity around n.

$$|\mathbf{E}^T| = |\mathbf{E}^I| \frac{2}{1+n} \Big[1 - \frac{c^2 \mu_0}{2n(1+n)} (\frac{\delta \alpha}{\delta Q})_0 Q(\Delta t) \Big] \tag{2.29}$$

Hence, we see that a correction is introduced to the linear configuration. In particular, if the equlibrium refractive index is regular in the pulse spectral region, all the modes of the radiation behave in a similar way. Furthermore, we insert the explicit expression for the amplitude in order to show the power dependence on the probe and pump incident field.

$$|\mathbf{E}^T| = |\mathbf{E}^I| \frac{2}{1+n} \Big[1 - \propto \Big(\sum_{\omega} \mathbf{E}_{\omega}^{pump} (\mathbf{E}_{\omega-\Omega}^{pump} + \mathbf{E}_{\omega+\Omega}^{pump}) \Big) \sin(\Omega \Delta t) \Big] \tag{2.30}$$

In the end, we collect all the constants in a factor γ and report the expression for the transmitted intensity I^T at the pump-probe delay Δt, as a function of probe and pump field. We define the transmitted intensity at equilibrium $I^T(0)$ and neglect the second order in γ.

$$I^T(\Delta t) = I^T(0) - \gamma |\mathbf{E}^I|^2 \Big(\sum_{\omega} \mathbf{E}_{\omega}^{pump} (\mathbf{E}_{\omega-\Omega}^{pump} + \mathbf{E}_{\omega+\Omega}^{pump}) \Big) \sin(\Omega \Delta t) \tag{2.31}$$

We observe that the transmitted intensity modulation is linear in both the pump and probe intensity.

2.1.4 Phase-dependent ISRS of the Probe

The modulation in the refractive properties of the material is not the only effect which modifies the trasmitted pulse intensity spectrum. Developing the driven oscillator formalism, we obtained the solution for the vibrational amplitude (eq. 2.12).

$$\mathbf{Q}(t') = \sqrt{(\mathbf{Q}_0 - \frac{\tau \boldsymbol{f}}{2\Omega})^2 + \frac{\mathbf{Q}_0 \boldsymbol{f} \tau}{\Omega} \Big(1 - \sin(\Delta \phi) \Big)} \cos\Big(\Omega t' + \Phi \Big) \tag{2.32}$$

We described the pump process setting the condition of null initial amplitude Q_0. Now, we can extend this approach to the probe case. We set

as initial amplitude the one resulting from the pump excitation. Then, we consider the force relative to the probe pulse.
In this configuration, the initial oscillation has a definite phase relation. In addition, the force phase depends on the field one. Hence, varying the delay between pump and probe permits to control the phase $\Delta\phi$ between pump phonon and probe force. As a function of $\Delta\phi$, the vibrational amplitude can be resonantly increased or dumped. The involved process is again the ISRS, whose cross-section is resonanlty amplified by the presence of the excited phonon.
In particular, the process is most effective when $|\Delta\phi| = \pi/2$. Actually, this can be intuitively understood in this terms. When the force is in phase with the velocity ($\Delta\phi = -\pi/2$) the first is always applied in the direction of motion and so the oscillation rises. Conversely, when in phase opposition ($\Delta\phi = \pi/2$) it dumps it. Between this two situations it has no effect, because half the period pushes in the direction of motion and half in the other one.

As regards the transmitted pulse, in this specific conditions we expect it to change its spectral shape. In fact, when the vibration is amplified the pulse leaves energy in the sample. Conversely, to the phonon dumping corresponds an energy gain. Considering that the photons number is constant, this should result in a red/blue-shift.
We give an analytical description of the resonant ISRS effects starting again from eq. 2.25.

$$\nabla^2\mathbf{E}(t') - \frac{n^2}{c^2}\frac{\partial^2\mathbf{E}(t')}{\partial t^2} = \mu_0(\frac{\delta\alpha}{\delta Q})_0\frac{\partial^2 Q(t'+\Delta t)\mathbf{E}(t')}{\partial t^2} \tag{2.33}$$

The dependence on the variable t' and the pump-probe delay Δt are explicitly reported.
In the previous discussion, we have seen that evaluating the term on the right hand side is useful to define an effective refractive index $\tilde{n}$, which describes a phonon dependent transmittivity modulation.
Now, we solve the differential equation in order to describe the effects of the propagation through the sample.
Considering the variable $t' = t - z\frac{n}{c}$, the following differential relations are valid:

$$\begin{cases} \frac{\partial f(t')}{\partial t} = \frac{\partial f(t')}{\partial t'} \\ \frac{\partial^2 f(t')}{\partial z^2} = -\frac{n^2}{c^2}\frac{\partial^2 f(t')}{\partial t^2} = -\frac{n}{c}\frac{\partial^2 f(t')}{\partial z \partial t'} \end{cases} . \tag{2.34}$$

Properly substituting these in the propagation equation, we obtain

$$-2\frac{n}{c}\frac{\partial^2\mathbf{E}(t')}{\partial z\partial t'} = \mu_0(\frac{\delta\alpha}{\delta Q})_0\frac{\partial^2 Q(t'+\Delta t)\mathbf{E}(t')}{\partial t'^2} \tag{2.35}$$

The result can be easily integrated in space, considering a sample with thickness z. We use the initial conditions $\mathbf{E}(t', z=0) = \mathbf{E}^I(t')$.

$$-2\frac{n}{c}\Big(\frac{\partial\mathbf{E}(t',z)}{\partial t'} - \frac{\partial\mathbf{E}^I(t')}{\partial t'}\Big) = z\mu_0(\frac{\delta\alpha}{\delta Q})_0\frac{\partial^2 Q(t'+\Delta t)\mathbf{E}(t')}{\partial t'^2} \tag{2.36}$$

We now integrate over t', which depends also on the spatial dimension and accounts for the light propagation time through the sample. We remind that the polarizability modulation with respect to the equilibrium value ($(\frac{\delta\alpha}{\delta Q})_0 Q$) is a small quantity. Therefore, we can consider a tiny modification of the electric field and approximate it equal to the incident one ($\mathbf{E}^I$) inside the r.h.s integral. In addition, we set the initial condition $\mathbf{E}(t'=0) = \mathbf{E}^I(t')$.

$$\mathbf{E}(t') - \mathbf{E}^I(t') = -\frac{cz\mu_0}{2n}(\frac{\delta\alpha}{\delta Q})_0\frac{\partial Q(t'+\Delta t)\mathbf{E}^I(t')}{\partial t'} \tag{2.37}$$

In order to understand the field spectral effects due to the interaction, we study its frequency components. Both the incident and transmitted field can be expressed with a Fourier expansion.

$$\mathbf{E}(t) = \int d\omega \mathbf{E}_\omega e^{i\omega t} \tag{2.38}$$

We remind that the explicit dependence of the vibrational amplitude is a sine function (eq. 2.14).

$$Q(t'+\Delta t) = Q_0\sin(\Omega(t'+\Delta t)) \tag{2.39}$$

We insert these and start to solve the derivative in the r.h.s. of eq. 2.37.

$$\begin{aligned}
&\frac{\partial Q(t'+\Delta t)\mathbf{E}^I(t')}{\partial t'} = \\
&= Q_0\int d\omega \mathbf{E}^I_\omega\Big(\sin(\Omega(t'+\Delta t))\frac{\partial e^{i\omega t'}}{\partial t'} + \frac{\partial\sin(\Omega(t'+\Delta t))}{\partial t'}e^{i\omega t'}\Big) = \\
&= Q_0\int d\omega \mathbf{E}^I_\omega\Big(i\omega\sin(\Omega(t'+\Delta t)) + \Omega\cos(\Omega(t'+\Delta t))\Big)e^{i\omega t'} = \\
&= \frac{Q_0}{2}\int d\omega \mathbf{E}^I_\omega\Big((\omega+\Omega)e^{i(\omega+\Omega)t'}e^{i\Omega\Delta t} - (\omega-\Omega)e^{i(\omega-\Omega)t'}e^{-i\Omega\Delta t}\Big)
\end{aligned} \tag{2.40}$$

We can explicitly see the dependence on the ISRS matching frequencies $\omega \pm \Omega$. We can riformulate the last expression changing the integration variable from ω to $\omega \pm \Omega$.

$$\begin{aligned} &\frac{\partial Q(t'+\Delta t)\mathbf{E}^I(t')}{\partial t'} = \\ &= \frac{Q_0}{2}\int d\omega\omega\Big(\mathbf{E}^I_{\omega-\Omega}e^{i\Omega\Delta t} - \mathbf{E}^I_{\omega+\Omega}e^{-i\Omega\Delta t}\Big)e^{i\omega t'} \end{aligned} \tag{2.41}$$

In the end, Fourier expanding also the first and second term in eq. 2.37, we obtain an equation for the frequency spectrum of the transmitted field.

$$\mathbf{E}_\omega(\Delta t) = \mathbf{E}^I_\omega + \frac{cz\mu_0}{4n}(\frac{\delta\alpha}{\delta Q})_0 Q_0\omega\Big(\mathbf{E}^I_{\omega+\Omega}e^{-i\Omega\Delta t} - \mathbf{E}^I_{\omega-\Omega}e^{i\Omega\Delta t}\Big) \tag{2.42}$$

We notice the dependence from the fields at $\pm\Omega$ typical of ISRS. In particular the contributions have opposite sign. This implies a shift in the spectral distribution from the high frequencies to the low ones, and vice versa.
From the last expression we can evaluate the measured intensity spectrum. We define the coupling constant $k_\Omega = \frac{cz\mu_0}{2\tilde{n}}(\frac{\delta\alpha}{\delta Q})_0 Q_0\omega$ and calculate the squared modulus.

$$I(\omega,\Delta t) = I^I(\omega) + k_\Omega\cos(\Omega\Delta t)\mathbf{E}^I_\omega[\mathbf{E}^I_{\omega+\Omega} - \mathbf{E}^I_{\omega-\Omega}] \tag{2.43}$$

We observe that the signal oscillates at the phonon frequency as a function of the pump&probe delay. The quantity $\Omega\Delta t$, can also be considered as the phase difference between the forces exerted respectively by probe and pump, $\Delta\phi_{probe-pump}$. Taking into account the vibration phase and eq. 2.15, we can write

$$\begin{aligned} \Omega\Delta t = \Delta\phi_{probe-pump} &= \phi_{probe} - \phi_{vib} + \phi_{vib} - \phi_{pump} = \\ &= \Delta\phi_{probe-vib} - \Delta\phi_{pump-vib} = \\ &= -\Delta\phi_{vib-force} - \pi/2 = -\Delta\phi - \pi/2 \end{aligned} \tag{2.44}$$

where we use the notation $\Delta\phi_{vib-force} = \Delta\phi$ in order to be consistent with the one from eq. 2.32.
Consequently, in agreement with the driven oscillator model, the pulse is red-shifted when the phase between vibration and force is $\Delta\phi = -\pi/2$, and blue-shifted when $\Delta\phi = \pi/2$.

In the end, we observe the intensity modulation power dependence on pump and probe field. In order to model it we explicit the pump dependence inside Q_0. All the constant factors are collected together in the γ' factor.

$$\begin{aligned} &I(\omega,\Delta t) - I^I(\omega) = \\ &+\gamma'\cos(\Omega\Delta t)\Big(\sum_{\omega'}\mathbf{E}^{pump}_{\omega'}(\mathbf{E}^{pump}_{\omega'-\Omega} + \mathbf{E}^{pump}_{\omega'+\Omega})\Big)\mathbf{E}^I_\omega[\mathbf{E}^I_{\omega+\Omega} - \mathbf{E}^I_{\omega-\Omega}] \end{aligned} \tag{2.45}$$

We see that in both cases the intensity result from the second power of the electric field, explaining the linear dependence on both pump and probe intensity.

2.1.5 Observable Spectral Effects

In this part, we summarize the results suggested by the developed classical formalism. In particular, we focus on the features detectable in the measured transmitted probe pulse.
We have seen that the pump pulse excites a coherent oscillation of the lattice through ISRS. Although we do not detect it, the transmitted pump pulse is red-shifted because of the energy lost in the sample[1] .
The presence of the vibrational mode modulates, at its proper frequency, the polarizability of the material. We test it with a probe pulse. It impinges at a controlled delay with respect to the pump, in order to be sensitive to the phase of the coherent phonon.

From the theory previously discussed, we expect two main effects. The first (2.1.3) is a transmittivity modulation due to the oscillation of the refractive index. Actually, it is a function of the polarizability. As a consequence of this, the transmittivity changes. We report the final expression for the transmitted intensity as a function of the pump&probe delay.

$$I^T(\Delta t) = I^T(0) - \gamma|\mathbf{E}^I|^2\Big(\sum_{\omega}\mathbf{E}_{\omega}^{pump}(\mathbf{E}_{\omega-\Omega}^{pump}+\mathbf{E}_{\omega+\Omega}^{pump})\Big)\sin(\Omega\Delta t) \quad (2.46)$$

The transmitted intensity oscillates at the phonon frequency Ω, around its equilibrium value $I_T(0)$. When in phase, $\Omega\Delta t = \pi/2$, less light is transmitted and more reflected. Conversely, when $\Omega\Delta t = -\pi/2$ the transmitted light increases. Furthermore, we underline the effect is the same for the whole spectrum.
The modulation is linear in the incident probe and pump (approximately) intensity.

The second probing process is characteristic of a multimode pulse, because it is a result of the ISRS, which consists in the interaction between photons of different frequency. This typology of interaction of the probe pulse can resonantly create or destroy phonons in the sample. This

[1]The spectral shifts of pump and probe pulses are both due to ISRS. However, we underline that they are not exactely identical in nature. Actually, the pump acts on the thermal ground state of the sample, the probe on a coherent excitation which has a definite vibrational phase.

results, respectively, in an energy loss or gain in the pulse. We report the transmitted intensity spectrum depending on the pump&probe delay.

$$I(\omega, \Delta t) - I^I(\omega) = \\ + \gamma' \Big(\sum_{\omega'} \mathbf{E}^{pump}_{\omega'} (\mathbf{E}^{pump}_{\omega'-\Omega} + \mathbf{E}^{pump}_{\omega'+\Omega}) \Big) \mathbf{E}^I_\omega [\mathbf{E}^I_{\omega+\Omega} - \mathbf{E}^I_{\omega-\Omega}] \cos(\Omega \Delta t) \tag{2.47}$$

When $\Omega \Delta t = 0$ the phonon velocity is in phase with the force resulting from the probe field. The Stokes process is enhanced: phonons are created and the probe pulse is red-shifted. Conversely, with $\Omega \Delta t = +\pi$ the Anti-Stokes process prevails and the probe spectrum is blue-shifted.

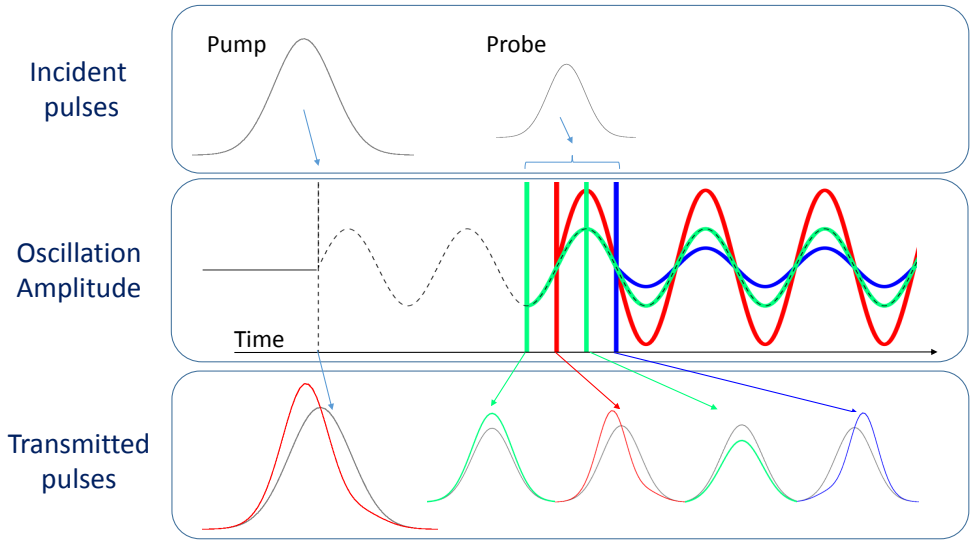

Figure 2.2: Summary of the interaction effects in the transmitted pulses. The pump pulse excites a coherent vibration (described as an harmonic oscillator) and it is red-shifted. The probe pulse is sensitive to the phase of the coherent phonon. It is sensitive to a modulation of the transmittivity. It can also be red/blue-shifted if it changes the vibrational energy owing to the ISRS.

In fig. 2.2 we sum up the relevant configuration characterizing the pump& probe measurement.
The relevant point to keep in mind is the fact that the refraction modulation and the resonant ISRS effect have different spectral feature and are $\pi/2$ shifted one to another.

We underline that the fourth-rank polarizability tensor $(\frac{\delta \alpha}{\delta Q})^2_{0_{ij,lm}}$, included in the factors γ and γ' can have peculiar symmetry properties.

These are useful to distinguish between the two probing effects.
Indeed, the ISRS hardly changes the photon polarization. It is a stimulated process, and so the new photons are not likely to be created in modes initially not occupied. Conversely, due to the refractive effect, the signal can be moved to the other polarization. This results from the anisotropic modulation of polarizability, which follows from the symmetry properties of the vibrational mode. In such a case, the refractive effects can be selected working with polarizers and analyzers to control the incident and output orientation.
We will discuss these issues in chapter 4, where we present the symmetry properties relative to the employed α-quartz sample and perform polarization selective measurements.

2.2 Quantum Formulation of the Classical Model

In this section, we riformulate the discussion previously developed, translating from the classical to a more fundamental quantum language. We quantize the classical fields in terms of operators. The system Hamiltonian is defined and applied to the quantum states in order to describe the interaction effects.
This quantum model is the result of a collaboration with the theoretical group of prof. F. Benatti [29].

2.2.1 Quantization of the Interaction Energy

The starting point is the classical interaction energy U^{int} as a function of polarizability and electric field, resulting from eq. 2.2, 2.3. The explicit polarizability dependence as a function of the vibrational displacement $\mathbf{Q}$ is shown.

$$U^{int} = -\Big(\alpha_{0ij} + \Big(\frac{\delta\alpha}{\delta Q^k}\Big)|_{Q^k=0}{}_{ij} Q^k\Big) E^i E^j \tag{2.48}$$

We can summarize the translation into a quantum language as the replacement of classical quantities with operators:

$$\begin{aligned} U^{int} &\rightarrow \hat{\mathcal{H}}^{int}, \\ \mathbf{E} &\rightarrow \hat{\mathbf{E}}, \\ \mathbf{Q} &\rightarrow \hat{\mathbf{Q}}. \end{aligned} \tag{2.49}$$

We want to obtain an expression for the interaction Hamiltonian $\hat{\mathcal{H}}^{int}$ as a function of the operators electric field, $\hat{\mathbf{E}}$, and phonon position, $\hat{\mathbf{Q}}$. The quantization of radiation and vibration fields is performed in terms of bosonic creation and annihilation operators.

The electromagnetic field is considered as a collection of harmonic oscillators, each representing a mode of the radiation. A mode of frequency ω and polarization λ, is described using the operators $\hat{a}^\dagger_{\omega,\lambda}$ and $\hat{a}_{\omega,\lambda}$, respectively creation and destruction. They obey the following commutation relation:

$$\big[\hat{a}_{\omega,\lambda}, \hat{a}^\dagger_{\omega',\lambda'}\big] = \delta_{\omega,\omega'}\delta_{\lambda,\lambda'} \tag{2.50}$$

The number of photons present in a mode is $\hat{N}_{\omega,\lambda} = \hat{a}^\dagger_{\omega,\lambda}\hat{a}_{\omega,\lambda}$.
The total energy of the radiation is $\hat{\mathcal{H}} = \sum_\lambda \sum_\omega \omega \hat{a}^\dagger_{\omega,\lambda}\hat{a}_{\omega,\lambda}$.

The expression for the electric field operator, propagating with $\vec{k}$ momentum in the λ polarization is

$$\hat{E}_\lambda(t,z) = i\sum_\omega \sqrt{\frac{\omega}{2V\epsilon_0}}\big(\hat{a}_{\omega,\lambda}e^{-i(\omega t-\vec{k}\cdot\vec{r})} - \hat{a}^\dagger_{\omega,\lambda}e^{i(\omega t-\vec{k}\cdot\vec{r})}\big), \tag{2.51}$$

where V is the considered volume.

Analogously, we quantize also the vibrational field. The creation and annhilation operators for phonons are $\hat{b}^\dagger_{\Omega,\vec{u}}$ and $\hat{b}_{\Omega,\vec{u}}$, where Ω is the frequency and $\vec{u}$ is the normal mode coordinate. They follow the commutation relation:

$$\big[\hat{b}_{\Omega,\vec{u}}, \hat{b}^\dagger_{\Omega',\vec{u'}}\big] = \delta_{\Omega,\Omega'}\delta_{\vec{u},\vec{u'}} \tag{2.52}$$

The number of quanta of excitation present in a mode is $\hat{N}_{\Omega,\vec{u}} = \hat{b}^\dagger_{\Omega,\vec{u}}\hat{b}_{\Omega,\vec{u}}$. The vibrational energy of the mode is $\hat{\mathcal{H}} = \Omega\hat{b}^\dagger_{\Omega,\vec{u}}\hat{b}_{\Omega,\vec{u}}$.
The expression for the vibration displacement operator is

$$\hat{Q}(t,\vec{r}) = \frac{1}{\sqrt{m\Omega V_S}}\big(\,\hat{b}_{\Omega,\vec{u}}e^{-i(\Omega t-\vec{u}\cdot\vec{r})} + \hat{b}^\dagger_{\Omega,\vec{u}}e^{i(\Omega t-\vec{u}\cdot\vec{r})}\,\big) \tag{2.53}$$

while the momentum is defined as

$$\hat{P}(t,\vec{r}) = i\sqrt{\frac{m\Omega}{V_S}}\big(\,\hat{b}^\dagger_{\Omega,\vec{u}}e^{i(\Omega t-\vec{u}\cdot\vec{r})} - \hat{b}_{\Omega,\vec{u}}e^{-i(\Omega t-\vec{u}\cdot\vec{r})}\big) \tag{2.54}$$

where V_S is the sample volume and m the reduced mass of the mode. We underline that to consider the whole sample volume is a good approximation for vibrational modes with a long correlation lenght, i.e. the quartz we employ in the experimental measurements.

Replacing the above operators in eq. 2.48 we obtain the interaction Hamiltonian.

$$\begin{aligned}\hat{\mathcal{H}}^{int} = \int_{V_S} d\vec{r}\sum_{\lambda,\lambda'}\Big[\alpha_{0\lambda\lambda'} + \Big(\frac{\delta\alpha}{\delta Q}\Big)|_0{}_{\lambda\lambda'}\frac{1}{\sqrt{m\Omega V_S}}\big(\,\hat{b}_{\Omega,\vec{u}}e^{-i(\Omega t-\vec{u}\cdot\vec{r})} + \text{ h.c.}\big)\Big]\times \\ \times\sum_{\omega,\omega'}\frac{\sqrt{\omega\omega'}}{2V\epsilon_0}\big(\hat{a}_{\omega,\lambda}e^{-i(\omega t-\vec{k}\cdot\vec{r})} - \text{ h.c.}\big)\big(\hat{a}_{\omega',\lambda'}e^{-i(\omega' t-\vec{k'}\cdot\vec{r})} - \text{ h.c.}\big)\end{aligned} \tag{2.55}$$

The resulting Hamiltonian can be separated in an equilibrium, $\hat{\mathcal{H}}_0$, and time-dependent Raman one, $\hat{\mathcal{H}}_R$.

Among the many resulting terms, we retain only the one that survive integrated over many periods, namely we perform the "rotating wave approximation". In particular, for the Raman term corresponds to consider as relevant the ones oscillating at resonance with the vibration and insert the condition $\delta(\omega - \omega' \pm \Omega)$. For the momentum conservation we obtain $\delta(\vec{k} - \vec{k}' \pm \vec{u})$. However, in our configuration the vibrational frequency is much smaller than the one of the involved electric fields, $\Omega << \omega$, so we can set $\vec{u} \simeq 0$ and hence $\delta(\vec{k} - \vec{k}')$.
Taking all this into account, we can write the Hamiltonian in the following way.

$$\begin{aligned}
\hat{\mathcal{H}}^{int} &= \hat{\mathcal{H}}_0 + \hat{\mathcal{H}}_R \\
\hat{\mathcal{H}}_0 &= -\frac{V_S}{V\epsilon_0} \sum_{\omega} \sum_{\lambda,\lambda'} \alpha_{0\lambda\lambda'} \hat{a}^{\dagger}_{\omega,\lambda} \hat{a}_{\omega,\lambda'} \\
\hat{\mathcal{H}}_R &= -\frac{\sqrt{V_S}}{V\epsilon_0\sqrt{m\Omega}} \sum_{\omega} \sum_{\lambda,\lambda'} \Big(\frac{\delta\alpha}{\delta Q}\Big)|_0 \, _{\lambda\lambda'} \hat{a}^{\dagger}_{\omega,\lambda} \hat{a}_{\omega+\Omega,\lambda'} \hat{b}^{\dagger}_{\Omega,\vec{u}} + \text{h.c.}
\end{aligned} \tag{2.56}$$

The term $\hat{\mathcal{H}}_0$ is responsible for the equilibrium refractive effects. For instance, off-axis terms in the polarizability tensor are responsible for the rotation of incident polarization: photons are moved from λ to λ', or vice versa.
In the Raman Hamiltonian we can clearly see the Stokes and Anti-Stokes nature. Photons are destroyed by $\hat{a}$ at ω and created by $\hat{a}^{\dagger}$ at $\omega \pm \Omega$, together with the emission ($\hat{b}^{\dagger}$)/annihilation ($\hat{b}$) of a phonon, respectively.

2.2.2 Interaction Effects on the Quantum State of Radiation

In the following, we describe the effects of the Raman interaction Hamiltonian in the measured transmitted probe pulse. In order to do it we define the quantum state of the incident pulses. We then let the operators evolve in the interaction picture. In the end we apply them to the states to evaluate the interaction outcome.

We employ the formalism of coherent states of the radiation. They are eigenstates of the creation operator.

$$\hat{a}_{\omega,\lambda} |\alpha_{\omega,\lambda}\rangle := \alpha_{\omega,\lambda} |\alpha_{\omega,\lambda}\rangle \tag{2.57}$$

The relative eigenvalue α is proportional to the mean value of the electric field calculated on such a state.

$$\langle \hat{E}_{\omega,\lambda} \rangle \propto \alpha_{\omega,\lambda} \tag{2.58}$$

Therefore we can describe the total electric field of a multimode pulse considering the set of coherent states and their eigenvalues.

The intensity of a single mode results from the evaluation of the operator $\hat{N} = \hat{a}^{\dagger}_{\omega,\lambda}\hat{a}_{\omega,\lambda}$ on the coherent state. To evaluate the modification in the spectral shape due to the Raman process, we have to calculate this quantity after the interaction.
We work in the interaction picture. This means that we let the operators evolve with the Raman interaction Hamiltonian, while the states are mantained constant. The evoluted creation operator is:

$$\hat{A}_{\omega,\lambda} := e^{i\tau\hat{\mathcal{H}}_R}\,\hat{a}_{\omega,\lambda}\,e^{-i\tau\hat{\mathcal{H}}_R}. \tag{2.59}$$

Considering that the portion of scattered photons is very small with respect to the unperturbed ones ($\sim 10^{-7}$), we can perform an expansion of the exponential term up to first order. The new expression is:

$$\hat{A}_{\omega,\lambda} = \hat{a}_{\omega,\lambda} - i\,\tau\left[\,\hat{a}_{\omega,\lambda}\,,\,\hat{\mathcal{H}}_R\,\right] \tag{2.60}$$

Starting from the evoluted creation and destruction operators, we can obtain the new number operators.

$$\hat{N}^{int}_{\omega,\lambda} = \hat{a}^{\dagger}_{\omega,\lambda}\hat{a}_{\lambda j} - i\tau\hat{a}^{\dagger}_{\omega,\lambda}\left[\,\hat{a}_{\omega,\lambda}\,,\,\hat{\mathcal{H}}_R\,\right] + i\tau\left[\,\hat{a}^{\dagger}_{\omega,\lambda}\,,\,\hat{\mathcal{H}}_R\,\right]\hat{a}_{\omega,\lambda} \tag{2.61}$$

The explicit expression of the commutator is

$$\left[\,\hat{a}_{\omega,\lambda}\,,\,\hat{\mathcal{H}}_R\,\right] = -\frac{\sqrt{V_S}}{V\epsilon_0\sqrt{m\Omega}}\Big(\frac{\delta\alpha}{\delta Q}\Big)|_0\,{}_{\lambda\lambda'}\big(\hat{a}_{\omega-\Omega,\lambda'}\hat{b}_{\Omega,\vec{u}} + \hat{a}_{\omega+\Omega,\lambda'}\hat{b}^{\dagger}_{\Omega,\vec{u}}\big). \tag{2.62}$$

Evaluating the number operators on the coherent states we get

$$\begin{aligned}\langle\hat{N}^{int}_{\omega,\lambda}\rangle &= |\alpha_{\omega,\lambda}|^2 + \\ &+ \frac{i\tau\sqrt{V_S}}{V\epsilon_0\sqrt{m\Omega}}\Big(\frac{\delta\alpha}{\delta Q}\Big)|_0\,{}_{\lambda\lambda'}\,\alpha_{\omega,\lambda'}\big(\alpha_{\omega+\Omega,\lambda'} - \alpha_{\omega-\Omega,\lambda'}\big)\,\langle\hat{b}^{\dagger}_{\Omega,\vec{u}} - \hat{b}_{\Omega,\vec{u}}\rangle \\ &= \langle\hat{N}_{\omega,\lambda}\rangle + \frac{\tau V_S}{V\epsilon_0 m\Omega}\Big(\frac{\delta\alpha}{\delta Q}\Big)|_0\,{}_{\lambda\lambda'}\,\alpha_{\omega,\lambda'}\big(\alpha_{\omega+\Omega,\lambda'} - \alpha_{\omega-\Omega,\lambda'}\big)\,\langle\hat{P}\rangle\,.\end{aligned} \tag{2.63}$$

We see that the modulation in the photon number goes like the derivative of the incident pulse intensity and depends on the phonon momentum. Therefore, it is modulated at the vibrational frequency and it is in agreement with the driven oscillator model. When in phase with the momentum the vibrational amplitude is increased, otherwise, out of phase it is dumped. This result in alterating red/blue-shift in the probe pulse, corresponding respectively to Stokes and Anti-Stokes scattering.

Despite the same involved ISRS process and similar resulting effects, we remark that this formalism does not describe the pump excitation. Actually, while the probe couples to a coherent excitation which has a definite vibrational phase and momentum, the pump acts on the thermal ground state of the sample. A detailed tractation of this point is developed in [29].

In conclusion, the present quantum model has been implemented in order to describe interaction in the classical limit. With respect to a purely classic model, it can be useful to predict or explain peculiar quantum features.
Although, this Hamiltonian fails in describing the non resonant transmittivity modulation in phase with the phonon position. Actually, this effect is not relative to the dipole term considered. The part of Hamiltonian describing quantistically a modification in the refractive index has not been modeled by us yet. For the time being, we include it as a boundary condition on the incident radiation.

Chapter 3

Experimental Setup

The setup is designed to perform pump&probe single-shot frequency-resolved measurements. These typology of experiment requires intense ultrashort light pulses, which are generated by a chirped pulse amplification laser system. The possibility to control the pulse duration and polarization is also implemented.

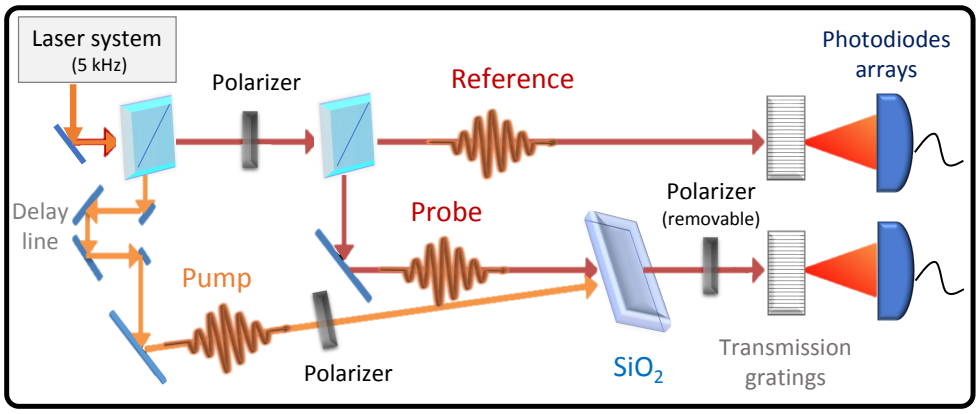

Figure 3.1: Scheme of the experimental setup.
A detailed description is reported in the text.

The scheme of the experimental setup is shown in fig. 3.1. The laser output is splitted in order to obtain the pump and probe beams. The first excites the sample, the latter, retarded by means of a delay line, tests the target at a controlled time with respect to the first stimulation. In this way, the transmitted probe signal carries informations on the time-evolution of the system.

A peculiarity of our setting is the introduction of a reference pulse copy of the probe, which is useful to distinguish in the transmitted signal only the relevant information about the interaction processes with the

sample.
Single-shot wavelenght-resolved spectra of both probe beams are measured through a transmission spectrometer. The spectrometer consists of a grating which diffracts the beam on the detector, which is a linear array provided with 256 photodiodes. A trigger properly regulates the acquisition at the laser repetition rate.

The pulse duration that can be tuned exploiting the dispersive compressor inside the laser system is measured by an intensity autocorrelator.

Half-waveplate and analyzer can be added to select the incident and signal polarizations. Polarization dependent studies are important in order to discriminate the symmetry properties of the phonon modes.

3.1 Ultrashort Pulse Generation

In this section, we present the instrumental apparatus used in our experiment for the generation of the ultrashort laser pulses. The pulse length can be tuned from less than few picoseconds, down to tens of femtoseconds.
They are initially produced by an oscillator and subsequently amplified. A complete scheme of the laser system is presented in fig 3.2.
Furthemore, exploiting the possibility to regulate the spread in time (chirp) of the different frequencies inside the multimode pulse, we can control the pulse duration. As a consequence of this, a study of the pulse lifetime dependence can be perfomed.

3.1.1 Pulsed LASER Source

The ultrashort laser pulses are produced by a Kerr-lens Mode-Locked Ti:Sapphire oscillator (VITARA-T), pumped by a continuous diode laser (VERDI). The oscillator frequency spectrum is approximately gaussian. It is centered around 800 nm and has a width of about 50 nm. The output power is 6 nJ/pulse and it is increased through a Chirped Pulse Amplification scheme (LEGEND ELITE DUO).

The amplification takes place because of stimulated emission in a Ti:Sa crystal. There, population inversion is obtained with a pulsed pump laser (REVOLUTION). The pump repetition rate sets the one of the output (5 kHz).
In order to avoid damages and non-linear effects due to the very high intensity, the ultrashort seed pulse coming from the oscillator is temporally stretched. After the amplification stage, the pulse duration is shortened again. This is achieved passing through the dispersive compressor, which works in a reversed way with respect to the stretcher.

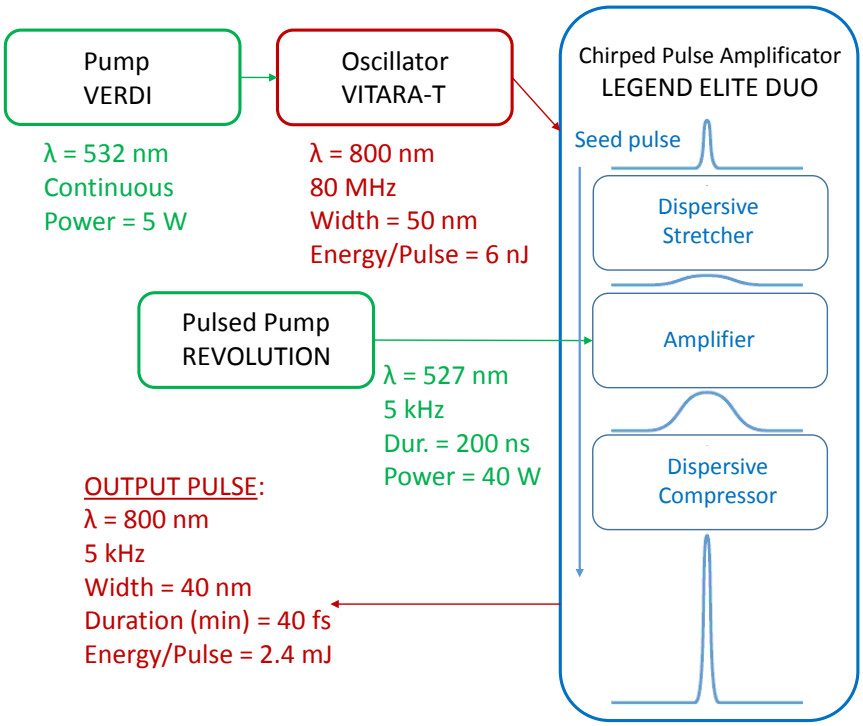

Figure 3.2: Scheme of the laser system.

The minimum pulse duration obtained with our laser system is 40 fs. The output power is about 12 W. In performing our experiments only a small part of this power is used. By means of a beam splitter, the 5% of the total intensity (about 0.12 mJ/pulse) is reflected and employed in the experiment.

3.1.2 Control and Characterisation of Pulse Duration

The compressor at the end of the laser system is tunable and it allows us to control the output pulse duration. In fact, it can regulate the time distribution of each spectral component as a nearly linear function of the wavelenght (chirp). In our experiment, we exploit this fact in order to study the pump&probe process as a function of the pulse duration.
We quantify the pulse lifetime by means of an intensity autocorrelator.

In the following we describe how the compressor and the autocorrelator work.

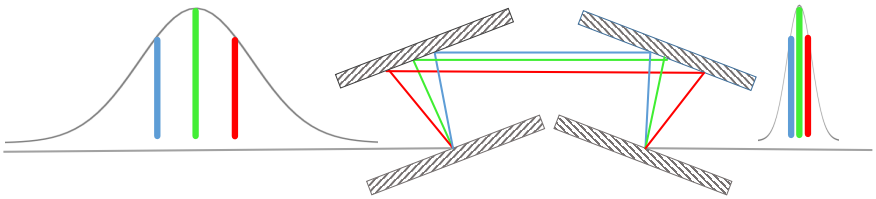

Figure 3.3: Scheme of the dispersive double grating compressor at the end of the laser system. Owing to the reflection geometry, different frequencies travel a different path and the relative timing between them is modified.

Chirp

In fig. 3.3 a scheme of the compressor is reported. Between a couple of dispersive gratings each frequency is reflected at a different angle and so travels a path of different lenght. Thus, each frequency takes a different time to go through the device.
The role of the compressor is to reach the minimum pulse duration after the chirped pulse amplification. However, it can be also used to increase the pulse lenght in a controlled way.
Depending on the particular geometry, shorter wavelenghts can be de-

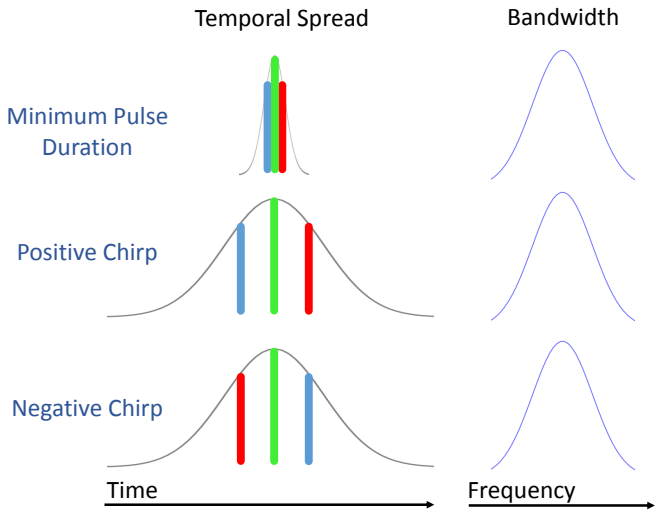

Figure 3.4: Pictorial representation of chirp. On the left, different temporal distributions of the frequencies is shown. On the right, the Fourier constant is not modified introducing a chirp.

layed with respect to the longer ones, or vice versa. A pulse prepared

in this way is defined to be positively or negatively chirped, respectively (3.4). In both cases, the overall pulse intensity is spread in a longer time range. Therefore, the pulse duration increases with respect to the Fourier Transform Limit, while the energy spectrum remains the same.

From another point of view, to introduce a chirp can be considered as to modify the phase of the components as a function of frequency. Anyway, we higlight that the refractive processes considered do not modify the degree of coherence of the pulse.

Intensity Autocorrelator

An electronic apparatus (based on, e.g., a photodiode) would be too slow for the measurement of the duration of ultrashort pulses with picosecond or femtosecond durations. Therefore optical autocorrelators are employed.

In an intensity autocorrelator, as shown in Fig. 3.5, a beam splitter divides an incoming pulse into two pulses, which are then focused into a crystal with a second order nonlinearity. By means of a delay line the relative timing of the pulses can be adjusted. If it is made small, so that they meet in the non-linear crystal, the process of second harmonic generation occurs, leading to an output with a frequency that is twice the incident one. This signal is measured by a slow photodiode detector.
If the relative time delay is increased, so that the overlap of the two pulses in the crystal is reduced, the mixing product becomes weaker. Hence, the signal dependence as a function of the delay reflects the pulse duration.

The intensity autocorrelation function $A(\tau)$ is defined as

$$A(\tau) = \int_{-\infty}^{\infty} I(t)I(t-\tau)dt \tag{3.1}$$

where I is the intensity measured by the detector at a time t and with a delay τ between the two overlapping pulses.

The crystal produces a second order non-linear field, resulting from the overlap of the two copies of the incident pulse

$$E_{NL} = \chi^{(2)}(E(t) + E(t-\tau))^2. \tag{3.2}$$

If the two pulse copies are not collinear the mixed term $E(t)E(t-\tau)$ propagates in a different direction with respect to the incident ones. Therefore, it can be detected alone. Its measured intensity is

$$\begin{aligned} I_{meas}(\tau) &= \int_{-\infty}^{\infty} |\chi^{(2)}E(t)E(t-\tau)|^2 dt \\ &\propto \int_{-\infty}^{\infty} I(t)I(t-\tau)dt = A(\tau) \end{aligned} \tag{3.3}$$

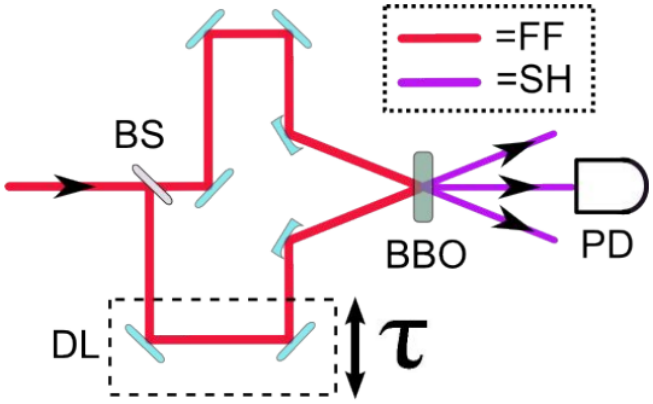

Figure 3.5: Optomechanical scheme of the intensity autocorrelator.
BS: beam splitter; DL: delay line; PD: photodiode; FF: fundamental frequency; SH: second harmonic [26].

which is an evaluation of the autocorrelation.

Precisely, a spectra as a function of τ is obtained. Its FWHM, applying the proper deconvolution factor (which for gaussian pulses is $\sqrt{2}$), gives the duration of the pulse (sigma of the temporal gaussian profile).

3.2 Spectrometer

In our experiment, we perform single-shot frequency-resolved measurements of both the interacting and reference probe pulse.

The laser beam is diffracted by transmission gratings, focused and collected in a detector.
The gratings have a groove density $G = 600$ mm^{-1}. For a beam centered around $\lambda_c = 800$ nm, the first order is diffracted approximately at an angle $\beta = 29$ °. Each wavelenght is collected in a different point on the detector by means of a lens of focal lenght $L_F = 10$ cm . The detector consists of an array with 256 photodiodes. Each diode is a silicon pixel with size $L_{pixel} = 5$ μm.

The effective resolution of the spectrometer can be estimated considering two factors: the optical and pixel resolution.
The first is related to the number of pixels covering the spectral range, the latter to the image of the input slit on the detector.

The optical resolution of the spectrometer is determined by the input

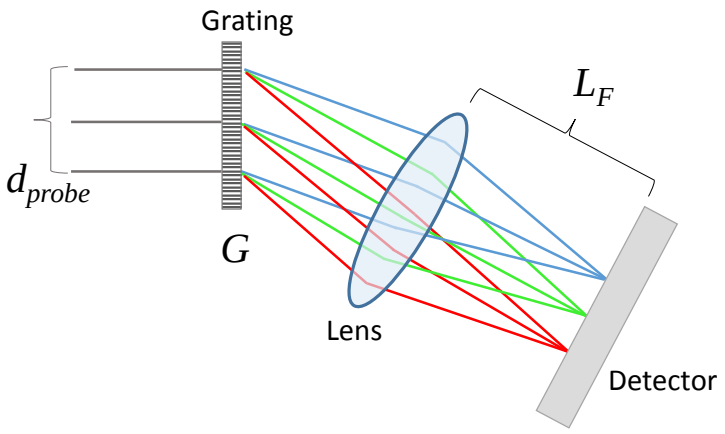

Figure 3.6: Scheme of the spectrometer.
The incident probe beam has a diameter d_{probe}. It incides on the transmission grating, which has groove density G, and it is dispersed in wavelenght. A lens, focal L_F, focuses each wavelenght in a different point on the detector. It is a linear array with 256 photodiodes.

beam size and the optics inside the spectrometer. The wider the beam, the more grating lines ($N = Gd_{probe}$) the beam illuminates and, therefore, the better the resolution. This is also referred to as the resolving power of the grating. It is calculated as

$$\Delta\lambda_{optical} = \frac{\lambda_c}{N} = \frac{\lambda_c}{Gd_{probe}} \approx 0.26 \text{ nm} \tag{3.4}$$

where a $d_{probe} = 5$ mm has been used.

The pixel resolution depends on the size of the pixels and on the dispersion and focalization geometry. Considering a pulse with a wavelenght spectrum in the range $\lambda_{min}, \lambda_{max}$, the wavelenght step between two adiacent pixels is roughly

$$\Delta\lambda_{pixel} = \frac{(\lambda_{max} - \lambda_{min})}{L_D} L_{pixel} \tag{3.5}$$

where L_D is the enlightened region on the array, given by

$$L_D = \frac{L_F}{G(\lambda_{max} - \lambda_{min})} cos(\beta). \tag{3.6}$$

In our case $\lambda_{max} - \lambda_{min} = 70$ nm, and inserting it we obtain

$$\Delta\lambda_{pixel} \approx 0.30 \text{ nm}. \tag{3.7}$$

From a practical point of view, our detectors are calibrated with respect to another reference spectrometer.
We report that in the data analysis a conversion from nm to THz is performed, in order to work with energy units. Doing this we take care of the different intensity distribution between energy and wavelenght, according to the relation $I(E) = I(\lambda)\left|\frac{d\lambda}{dE}\right|$.
The above resolutions expressed in THz result:

$$\Delta\lambda_{optical} \approx 0.12 \text{ THz}, \ \Delta\lambda_{pixel} \approx \ 0.14 \text{ THz}. \tag{3.8}$$

In addition to the frequency resolution, the other important characteristic of the present spectrometer is the capability to acquire single-shot measurements.
A trigger, synchronized with the laser repetition rate, activates all the diodes whenever an ultrashort pulse is reaching the detector. They produce a signal relative to the whole intensity spectrum at once, which is then read pixel by pixel. The information relative to a single diode is read in 0.5 μs time and so the 256 pixels array is scanned in 128 μs, which is compatible with the 5 kHz pulse rate.

3.3 Polarization Geometry Selectivity

Every phonon has its specific symmetry properties. As a consequence of this, an excited vibrational mode assumes a definite orientation with respect to the polarization of the pump pulse. The probing process, in turn, depends on the phonon geometry. Hence, the polarization of the transmitted field, depends on both pump and probe ones.

Taking into account this, we develop a polarization selective setup suitable for symmetry analysis.
In particular, in case of linearly polarized pulses, the relevant parameter is the angle between the two orientations[1]. In our setup, this is controlled by an half-waveplate which rotates the pump polarization relatively to the probe one. The latter is the one of the laser output, which is parallel to the table plane.
Moreover, an analyzer after the sample can be added[2] to select the polarization of the transmitted light.

[1] When not interested in symmetry analysis, we usually set the pump crossed to the probe in order to minimize the interference effects between the two.

[2] Performing the measurements for which the analyzer was not strictly necessary, we removed it in order to obtain a pulse more similar to the reference one.

Chapter 4

Mean-Value Pump&Probe Measurements on Quartz

In this chapter, results from pump&probe measurements on an α-quartz sample are presented. The aim of these is to set the basis for the statistical analysis of correlations. They are fundamental in order to characterize the observable effects and verify the theory developed in chapter 2.

In our experiment, an ultrashort light pulse (the pump) impulsively perturbs the lattice, exciting a coherent phonon mode. A second one (the probe) interacts with the sample properly delayed in time with respect to the pump.
The measured quantity is the trasmitted probe pulse spectrum. In particular, for a fixed pump-probe delay, the mean over a set of repeated single shot acquisitions is calculated.
As a function of the delay, a response modulating at temporal frequencies characteristic of the vibrational modes of the material is measured.

We underline that an energy resolved probe spectrum is detected. This allow us to distinguish the phase of the oscillating signal relative to each probe photon mode. In this way, we can discriminate modification in the spectral shape of the pulse.

We list the points we are going to treat in the chapter. In the next section, we report the properties of the α-quartz sample.
After that, we present the experimental data. We discuss the main features of the distinct observable effects. We also make use of Fourier analysis in order to obtain the phonon frequency spectrum of quartz. Furthermore, we will verify the non-linear order and symmetry properties predicted by the theory, respectively via fluence dependence and polarization selective studies.

In the end, a phenomenological analysis of the effects of the pulse duration is presented.

4.1 Phonon Modes of Quartz

In our experiment, we work with an α-quartz sample. Firstly, it is adequate for trasmission spectroscopy purposes because of its high transparency and photoresistance. Furthermore, since our final goal is to develop a new spectroscopic technique (*Noise Correlation Spectroscopy*), we need to rely on a well known and simple system, characterized by strong Raman lines.
Quartz can be considered as a benchmark material for the dynamic excitation of phonons via stimulated Raman scattering and it represents our ideal playground to test NCS.

Quartz undergoes a phase change at about 848 K. The low-temperature phase, with trigonal symmetry, is called α-quartz. It has a trigonal crystal structure with $D3$ symmetry and $N = 9$ atoms per unit cell. Group-theory calculations show that the $3 \times N = 27$ degrees of freedom are divided into 2 acoustic vibrations of $A2 + E$ symmetry and 16 optical vibrations of $4A1+4A2+8E$ symmetry. In particular, the quartz Raman-active vibrational modes are 4 totally symmetric modes of species A1, and 8 doubly degenerate modes of species E. In fig. 4.2 the Raman spectra of alpha-quartz are reported.

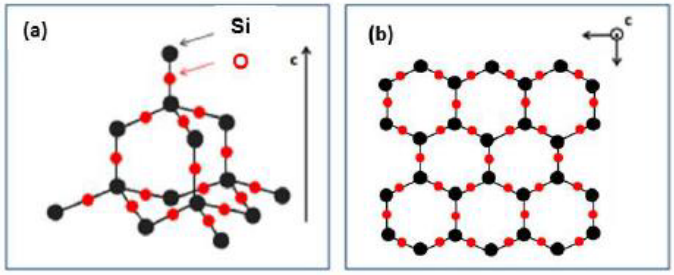

Figure 4.1: Atomic arrangement in quartz [10]. a) Crystal structure of α-quartz. b) its projection on the plane perpendicular to the c-axis.

In our experiment, the sample is a 1 mm thick α-quartz, oriented in order to have the principal symmetry axis (c-axis) parallel to the probe propagation direction. The pump direction is almost collinear with the probe one. Assuming that all the involved optical fields propagate along the z direction, we can limit our analysis to the xy plane. In this configuration, the symmetry of the system is reduced to $C3$ rotational symmetry. So, the only excited vibrational modes are those of an equilateral

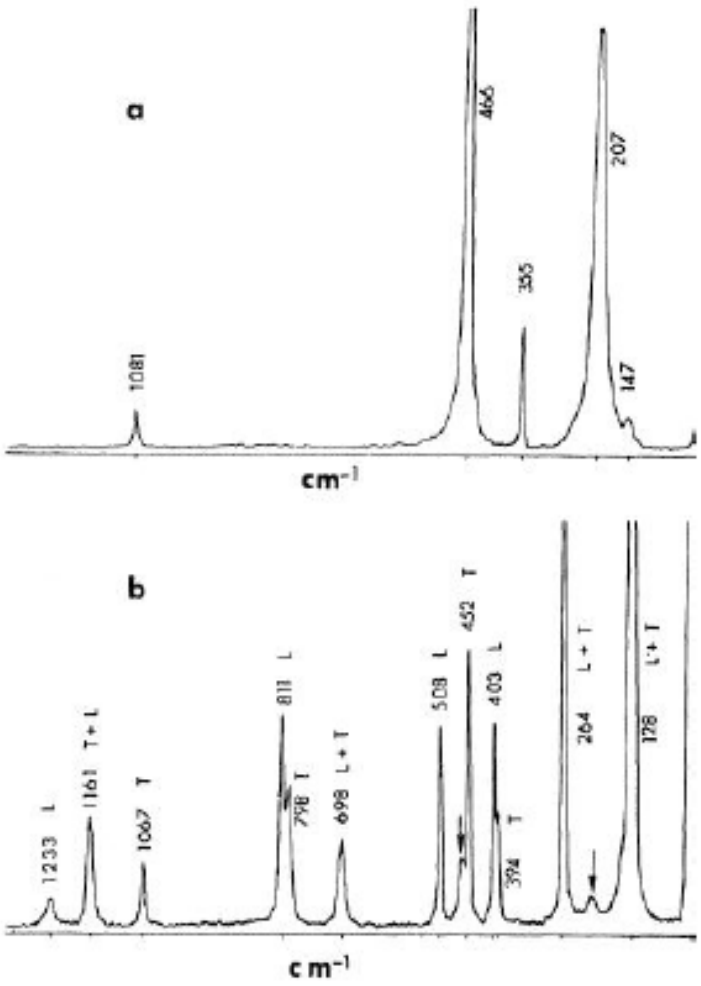

Figure 4.2: Room-temperature Raman spectra of α-quartz, reproduced by [11]. (a) A_1 modes. (b) E modes. Polarization assignments (L =longitudinal, T =transverse). The arrows indicate intense A_1 modes being transmitted due to imperfect alignment.

triangle with equal masses and equal bond strengths. Such a model crystal has three normal modes representing two types of symmetry: one with A-symmetry known as the 'breathing' mode, and two degenerate E-symmetry modes (fig 4.3). In this case the quartz polarizability tensor

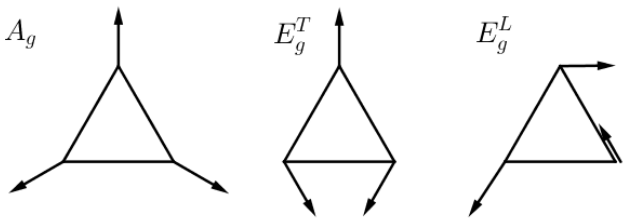

Figure 4.3: Normal mode vibrations for a system with C3 symmetry. A symmetric A_1 breathing vibrational mode and a doubly-degenerate E-symmetry vibrational mode.

(expressed with the same notation as in chapter 2) has the form:

$$(\frac{\delta\alpha}{\delta q})_{0\ ij} = A_{ij} + {E^L}_{ij} + {E^T}_{ij} = \begin{pmatrix} a+c & -c \\ -c & a-c \end{pmatrix} \tag{4.1}$$

where

$$A_{ij} = \begin{pmatrix} a & 0 \\ 0 & a \end{pmatrix}, E^L_{ij} = \begin{pmatrix} c & 0 \\ 0 & -c \end{pmatrix}, E^T_{ij} = \begin{pmatrix} 0 & -c \\ -c & 0 \end{pmatrix} \tag{4.2}$$

are the polarizability tensors relative to the totalsymmetric A mode and the longitudinal, E^L, and transverse, E^T, E symmetry modes.

From these the third order susceptibility tensor is calculated as:

$$\begin{aligned} (\frac{\delta\alpha}{\delta q})^{\ 2}_{0\ ijlm} &= A_{ij}A_{lm} + {E^L}_{ij}{E^L}_{lm} + {E^T}_{ij}{E^T}_{lm} = \\ &= \begin{pmatrix} \begin{pmatrix} a^2+c^2 & 0 \\ 0 & a^2-c^2 \end{pmatrix} & \begin{pmatrix} 0 & c^2 \\ c^2 & 0 \end{pmatrix} \\ \begin{pmatrix} 0 & c^2 \\ c^2 & 0 \end{pmatrix} & \begin{pmatrix} a^2-c^2 & 0 \\ 0 & a^2+c^2 \end{pmatrix} \end{pmatrix} \end{aligned} \tag{4.3}$$

where the external indices account for the probe polarization components, while the inner for the pump ones, relatively to a reference system defined by the 0° analyzer orientation [12].

In the following analysis of the experimental results we will repeatedly refer to this section. Actually, we will use the spectra in fig. 4.2 to address the observed phonon modes. Moreover, the discussion of the polarization dependence will be based on the expression for the third order tensor.

4.2 Data Analysis

In this section, we present the general features of a measurement, common to all the different configurations studied. We begin reporting how the raw experimental data are treated.
Then, we focus on their analysis: we observe and classify the pump&probe effects.
After that, we use Fouirer and Wavelet analysis in order to study the energy and lifetime of the different phonon modes excited.

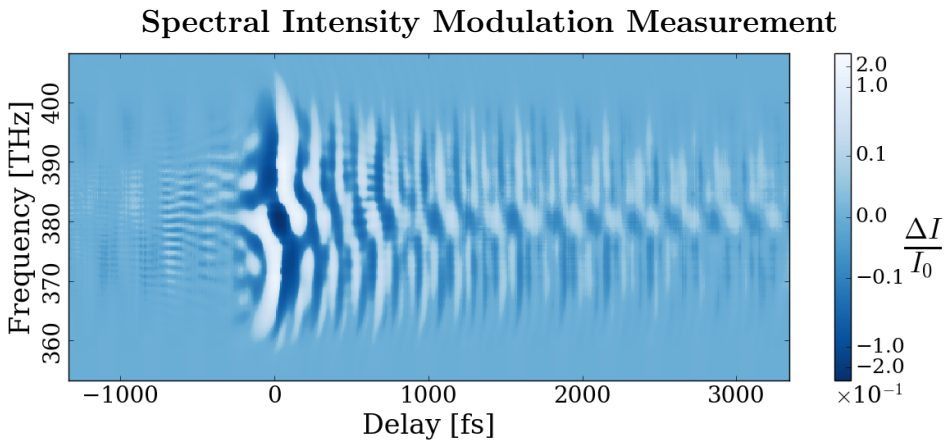

Figure 4.4: Pump&probe Frequency-Resolved Measurement.

The fundamental pump&probe datasets consist of 2D maps, which are energy-resolved measurements of the probe intensity, scanned as a function of the pump-probe delay. We work with a 0.15 THz energy-resolution and 6.7 fs delay-resolution.
The spectrum associated to a single time is the mean of many (1k-10k) single pulse acquistions, at 5 KHz repetition rate.

In the experimental setup, the probe beam is splitted in two arms: one interacts with the sample, the other one works as reference. So we collect a map for both the sample and reference channel. The reference pulse is a beam-splitted copy of the incident one. Therefore, subtracting its spectrum to the transmitted one allows to cancel out the classical fluctuations and obtain a less noisy measurement along the time-axis.

Another way to improve the results is to consider the trasmitted probe interacting with the sample before the pump excitation, namely at negative delay times. In fact, subtracting to the trasmitted probe at positive times the one at negative ones, permits to select the only changes of the trasmittivity triggered by the pump pulses. In fig. 4.4 a standard 2D pump&probe mean-value measurement is presented. The horizontal axis

represents the delay, along the vertical axis there are the energies of the spectral components of the probe pulse. The above described analysis involving the reference pulse and the negative times has been carried on, so the effects of the pump&probe process are selected. The colourscale indicates an increase (white) or a decrease (dark blue) in the probe intensity, with respect to the negative time signal.

Studying the spectral dependence as a function of the delay, we can observe some repeating features. In the following, we will demonstrate that this periodicity evolves at the phonon frequency. Moreover, the fact that we perform an energy resolved measurement allow us to discern distinct effects. Besides the complications due to phonons of different frequency, we can notice the presence of periods consisting of four main steps, reported in fig. 4.5.

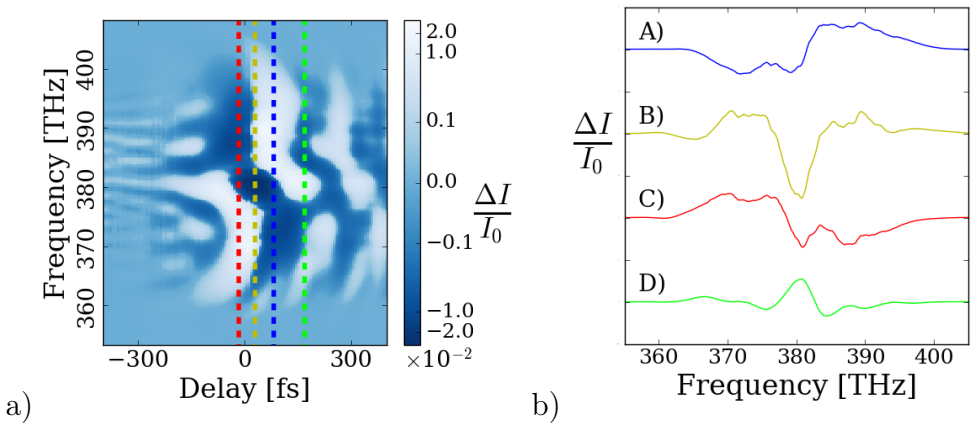

Figure 4.5: Spectral weight modulation at different delays.
a) Localization of the selected delays shown.
b) A) blue-shift, B) decreased trasmittivity, C) red-shift, D) increased trasmittivity.

We can classify these features considering whether the modulation is most effective in the side or central region of the pulse spectrum. As described in chapter 2, this two different situations correspond to the resonant ISRS of the probe and to the modulation of the refractive index, respectively. The ISRS process modifies the shape of the probe pulse, lessening the intensity on one side and rising it on the other. So the pulse is red-shifted (4.5bC) or blue-shifted (4.5bA) depending on whether it loses or gains energy interacting with the phonon. As a consequence of this, fig. 4.6a shows clearly that the two different sides of the spectrum oscillate in phase opposition.

Instead, the change in refractive index results in a global increasing

(4.5bD) or decreasing (4.5bB) of the transmittivity in the middle of the spectrum. The fact that this effect is evident only in the central region is owing to the fact that the ISRS effects are minimum there. Indeed, in fig. 4.16b we will show the refractive modulation spreads all over the spectrum, presenting a peculiar measurement in which the ISRS effects are hidden through polarization selection.

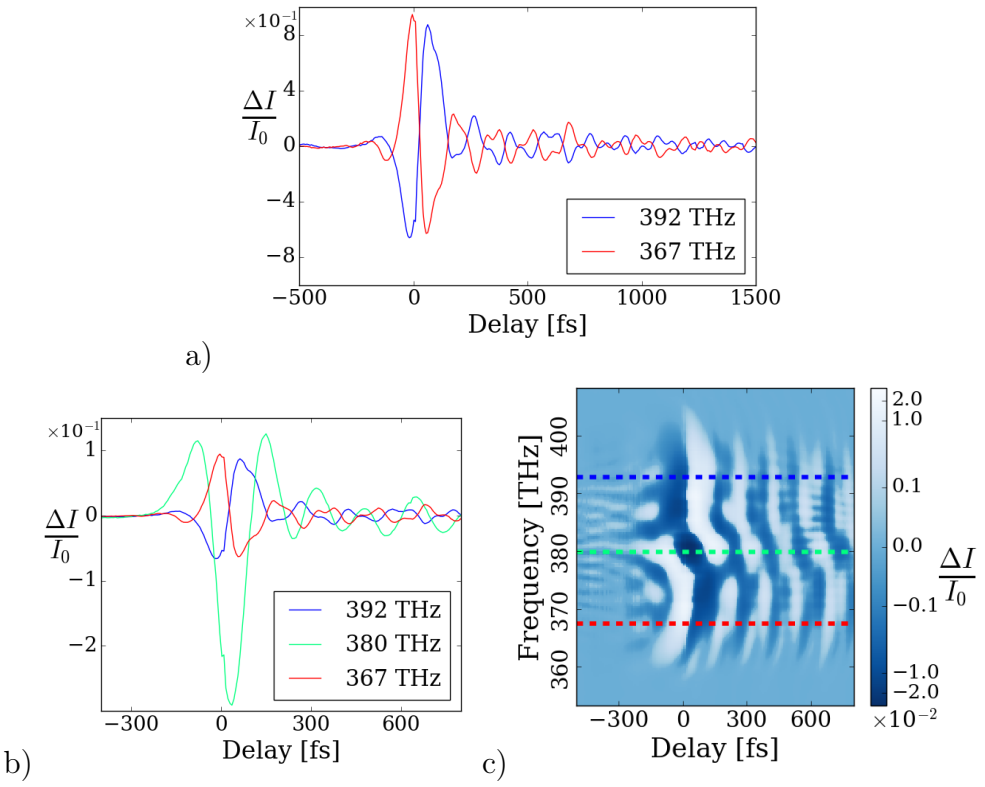

Figure 4.6: Dynamical response at selected pulse frequencies.
a) The two sides of the pulse spectrum are in phase opposition due to ISRS effect. b) The central part of the pulse oscillates (green) only due to trasmittivity modulation. Notice the $\pi/2$ phase difference with respect to the sides of the pulse, reflecting the phase difference between the trasmittivity modulation and ISRS effect. c) Localization of the shown frequencies in the pump&probe map.

We underline another fundamental difference between the probe ISRS and transmittivity modulation. Fig.4.5 suggests that their maxima are a quarter of period shifted to one another. This is evident in fig.4.6b, where the oscillation along the delay axis of the middle part of the pulse spectrum has a $\pi/2$ phase difference with respect to the sides. This can be easily seen noting that to the extremes of the central oscillation always

correspond a zero amplitude point of the side ones.

Therefore, the $\pi/2$ dephasing between the two effects is in agreement with the theory in chapter 2. As presented there, this phase-shift follows from the fact that the transmittivity modulation is in phase with the oscillation of the coherent phonon mode. Conversely, due to its resonant nature, the probe ISRS is in phase with the phonon velocity.

4.2.1 Fourier Analysis

The considerations done above are relative to a single phonon mode configuration. Actually, we are working with an α-quartz sample which has multiple modes (sec. 4.1) with different frequencies. Anyway, in first approximation the phonons are independent from each other. Thus, the preceeding discussion is still valid and can be easily generalized to a multi-phonon configuration. The observed effects are just the superposition of oscillations at different frequencies.
In order to recognize the different phonon frequency we make use of Fourier analysis.

From the pump&probe time-energy map(fig. 4.4), we calculate the Fourier Transform along the delay axis, in the positive times range. In particular, it is evaluated the FT modulus for each energy of the spectrum. The result is a 2D map (fig. 4.7): in the vertical axis is still reported the pulse spectral range, while in the horizontal one there are the frequencies of the Fourier domain.
The vertical stripes in this map correspond to specific frequencies, which indicate the energies of the phonon modes measured.

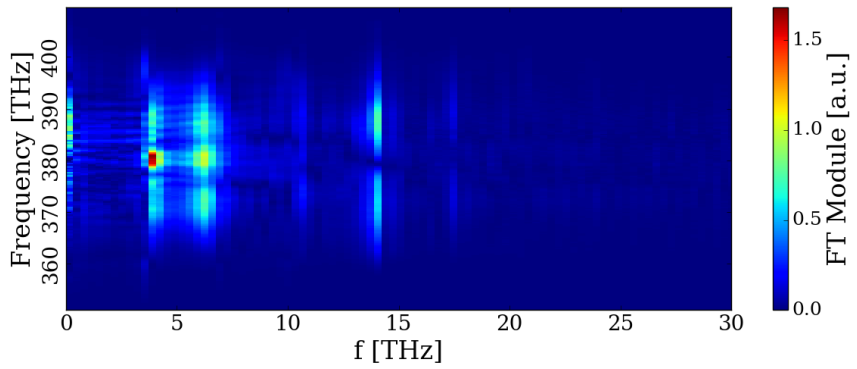

Figure 4.7: Fourier Transform of the pump&probe map along the delay axis. The vertical stripes indicate the frequencies of the detected phonon modes.

We underline that considering the modulus only we neglect the in-

formation on the imaginary part. So we lose the phase properties that characterize the different regions of the pulse spectrum. However, the fact that each energy carries the same information, allow us to average along the vertical axis. In this way we obtain the averaged phonon frequency spectrum in fig. 4.8.

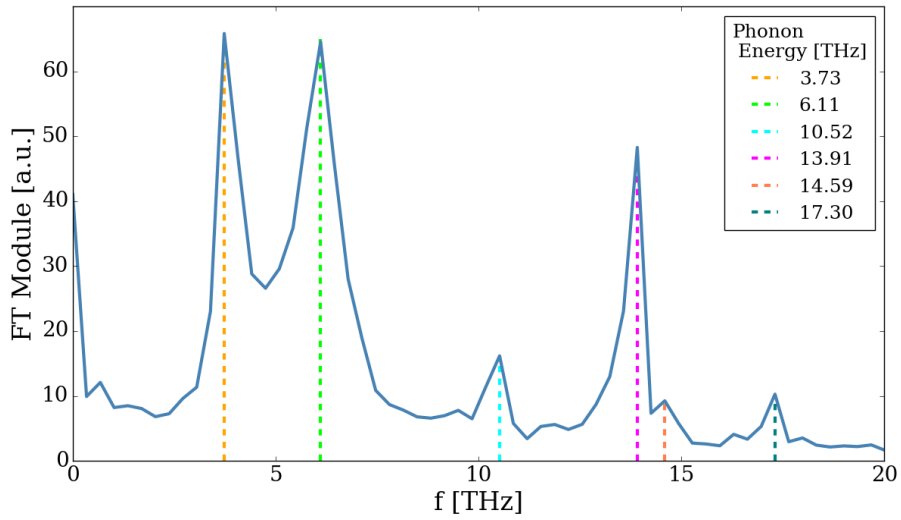

Figure 4.8: Cumulative Fourier spectrum obtained summing the map in fig. 4.7 along the pulse energies.

From the Fourier spectrum three main peaks can be recognized, at about 3.7, 6.1 and 13.9 THz. With the help of the reference phonon spectrum of quartz (fig. 4.2), we can identify them: the first is an E-symmetry mode, the second and third are A-symmetry modes.
Furthermore, due to the high quality of the measurement considered, we notice two other minor features. At about 10.5 THz a low intensity A mode is present. The shoulder at 14.6 THz and the small peak at 17.3 THz have no correspondence in the reference data. We guess they are the footprint of sum-frequency of two mode: the 3.7 THz added respectively to the 10.5 THz and 13.9 THz mode. This hypothesis is supported by the results of the phonon lifetime analysis in the next section.

In the following table there is a summary of the observed phonons: measured and reference frequencies are reported. The experimental error is the Fourier domain resolution. In addition, the symmetry of the mode is indicated.

Peak	Experiment [THz]	Reference [THz]	Symmetry
1	3.73 ± 0.34	3.84	E
2	6.11 ± 0.34	6.21	A
3	10.52 ± 0.34	10.64	A
4	13.91 ± 0.34	13.97	A
5	14.59 ± 0.34	14.48	mixed (1+3)
6	17.30 ± 0.34	17.81	mixed (1+4)

4.2.2 Phonon-Lifetime Analysis

In this section, we study the lifetime of the observed phonons. We analyze how the signal relative to each mode decays in time. As done before, we calculate the Fourier spectrum along the delay axis, averaged over the pulse energies. The key point of this analysis is to do it in a time dependent range.
In order to do it, we select a reduced part of the pump&probe delay axis, applying to the data a gaussian window 900 fs wide. Moving the window along the time axis, we obtain the evolution of the phonon frequency spectrum. The result is a 2D map, similar to what can be obtained with wavelet analysis. On one axis there is the Fourier domain. On the other one the time scale, where a point represents the delay time around which the corresponding window is centered.

In fig. 4.9 the outcome of the analysis is shown. It is very clear that the mode at 6 THz has a short lifetime compared to the others, which have lifetimes comparable or larger than the range measured.

From the map we extract the temporal decay profile for each single phonon mode. We do it integrating few time scans around the peak maximum. We normalize the signal of the first point, to better compare the different trends. They are plotted together in fig. 4.10. We observe all the modes to have an exponential decay. In order to estimate the time constant we perform a fit. The results are shown in fig. 4.11.

In the previous section, we formulated the hypothesis that some observed feature are sum-frequency signals. The fact that the 3.7, 10.5 and 13.9 THz phonons have similar slow decay reinforces this.
Indeed, the probability of such effects is quite low and long lasting phonon excitations help to detected them. Furthermore, the 17.3 THz peak is clearly observable in the decay map. It reasonably shows a long lifetime, similar to that of the modes from which should be originated (3.7 and 13.9 THz).

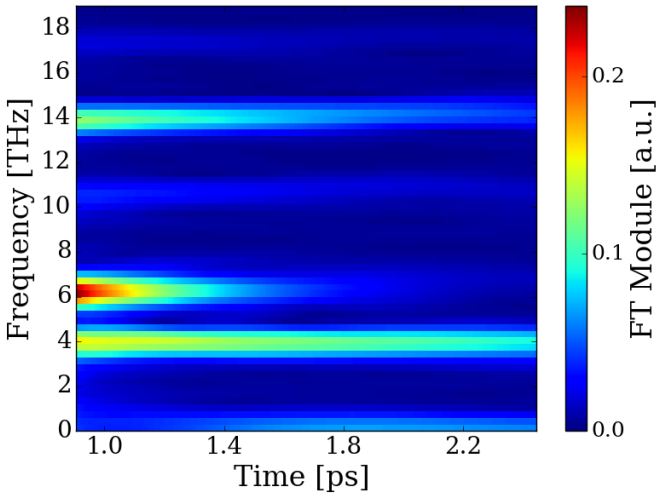

Figure 4.9: Phonon lifetime analysis.
On the horizontal axis the pump&probe delay is reported. On the vertical axis there are the frequencies of the phonon spectrum. The faster decay of the 6 THz mode can be easily noticed.

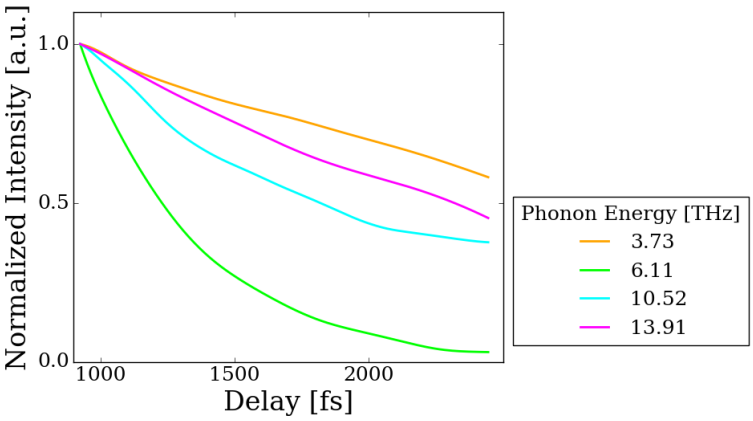

Figure 4.10: The decay profile of each detected phonon is selected from the frequency-delay map (fig 4.9). In order to distinguish the different trends the signals at the initial time are normalized to 1.

Following this way of reasoning, it is likely that also a contribution from the sum of 3.7 and 6.1 THz mode is present. In particular, it should be close to the zero delay time, when the 6.1 THz phonon gives a very strong signal. However, this is difficult to prove, because it would overlap together with the peak of the 10.5 THz mode. Anyway, the decay curve relative to it shows a different concavity in the first points of the curve. This can be a clue of a rapidly decaying signal summed to a regular exponential.

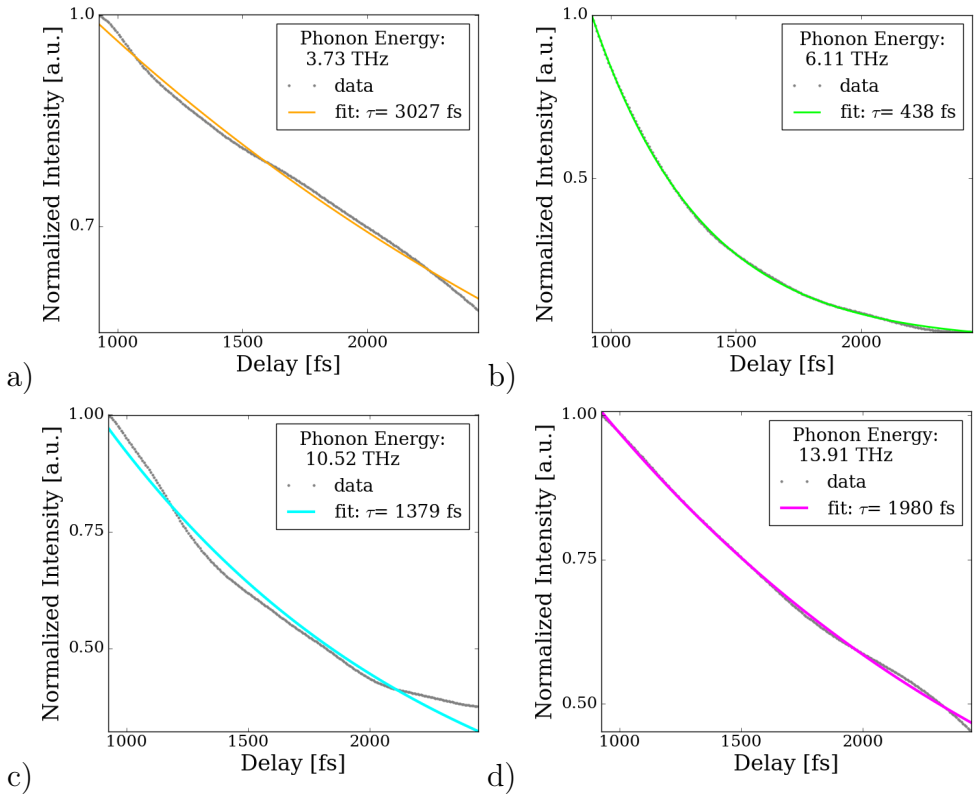

Figure 4.11: Fit of the decay profile for each detected phonon.
The exponential time constant obtained from the fit is reported in the box.
a) 3.7 THz b) 6.1 THz c) 10.5 THz d) 13.9 THz.

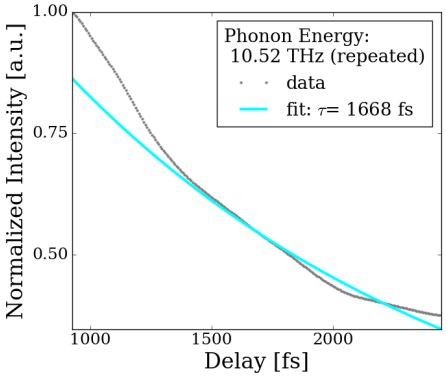

Figure 4.12: Fit for the 10.5 THz phonon excluding the initial times, where a sum-frequency contribution is believed to be summed to the exponential profile.

Taking this into account, we repeat the relative fit excluding the initial times. The result is reported in fig. 4.12.

4.3 Intensity Dependent Measurements

In this section, we are intended to verify the order of the non linear effects observed. The theory (chapter 2) predicts that both the probe ISRS and transmittivity modulation are linear in the pump and the probe fluence. In detail, we recall the expression for the pump&probe intensity modulation, presented in eq. 2.46-2.47:

$$I_\omega^T(\Delta t) = I_\omega^T(0) - \sum_n \gamma_n |\mathbf{E}_\omega^I|^2 \Big(\sum_\omega \mathbf{E}_\omega^{pump} (\mathbf{E}_{\omega-\Omega_n}^{pump} + \mathbf{E}_{\omega+\Omega_n}^{pump}) \Big) \sin(\Omega_n \Delta t) + \\ + \sum_n \gamma_n' \Big(\sum_{\omega'} \mathbf{E}_{\omega'}^{pump} (\mathbf{E}_{\omega'-\Omega_n}^{pump} + \mathbf{E}_{\omega'+\Omega_n}^{pump}) \Big) \mathbf{E}_\omega^I [\mathbf{E}_{\omega+\Omega_n}^I - \mathbf{E}_{\omega-\Omega_n}^I] \cos(\Omega_n \Delta t) \tag{4.4}$$

where we sum the contributions of the N different phonon modes present. Ω_n is the phonon frequency, γ_n the relative third order polarizability tensor and Δt the delay between pump and probe.
Indeed, both effects are proportional to the square of the pump and probe electric field. Thereby, the overall effect gives also a signal linear in intensity.
In order to discriminate between the two effects, the phase $\Omega_n \Delta t$ must be taken into account. The $\pi/2$ shift implies that when one effect is maximum, in modulus, the other does not contribute to the signal. So, in order to test separately the processes, we will analyse the amplitude of the spectral modulation at two properly distinct delays.

The fundamental parameter in this typology of analysis is the fluence f. It is defined as a function of the beam power P, repetition rate r and spot size d in the sample.

$$f[\mathrm{mJ/cm^2}] = \frac{P[\mathrm{mW}]}{r[\mathrm{Hz}] \cdot d^2[\mathrm{cm^2}]} \tag{4.5}$$

We work with a 5 kHz pulse repetition rate. The pump spot size is about 500 μm and the probe one is 200 μm. The studied power range is 30-120 mW for the pump and $40 - 650$ μW for the probe, which correspond to fluences of about $0.2 - 1.0$ mJ/cm^2 and $0.2 - 3.3$ μJ/cm^2, respectively.

Pump Intensity Dependence

The pump intensity dependence is studied in a fluence range of $0.24 - 0.96$ mJ/cm^2, with a constant probe fluence of 0.75 μJ/cm^2.

The overall linearity of the ISRS and transmittivity modulation effects is tested by means of Fourier analysis. We calculate the phonon frequency spectrum for each pump fluence setting. They are reported in fig. 4.13a. We compare the different amplitudes obtained and observe that the signal increases with the pump fluence . We select the maxima of the peaks in the spectra. We fit the maxima relative to each phonon, as a function of fluence (fig. 4.13b). The linearity is verified.
We report that in the high fluence measurements the data has been slightly modified. We subtracted the background, calculated in points close to considered peak. In fact, it is always detected also a residual pump signal. It is not present in the reference channel and so its fluctuations cannot be properly balanced. Obviously, this becomes more problematic the more intense is the pump beam.

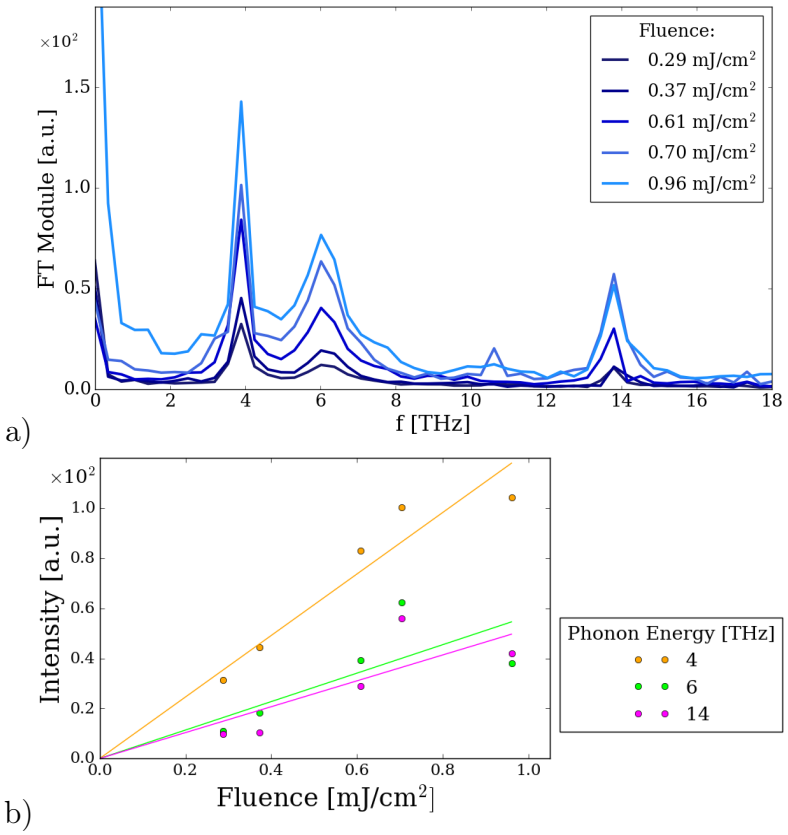

Figure 4.13: Pump intensity dependent results.
a) Fourier trasforms b) Fit of the maxima.

In order to separately check the linearity properties of the two effects, we study the modulation of the pulse spectrum at two different pump&probe delays. The first time (fig. 4.14a) correspond to a maxima

of the transmittivity modulation, when the central region of the spectrum rises. The second one (fig.4.14b) to an ISRS induced blue-shift of the pulse.
We select the maxima of the modulation, and fit them as a function of fluence. In both cases the linearity is roughly verified.
In this case the data have not been corrected accounting for the residual pump scattering. This could explain the deviation form fit of the high fluence data.

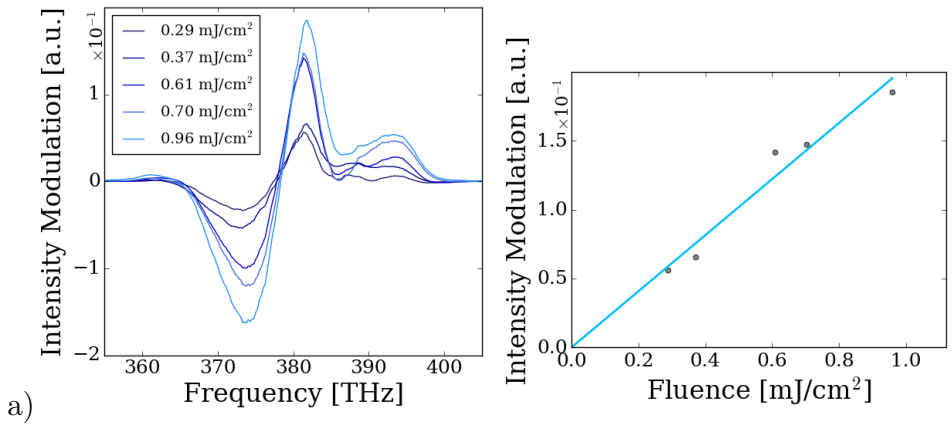

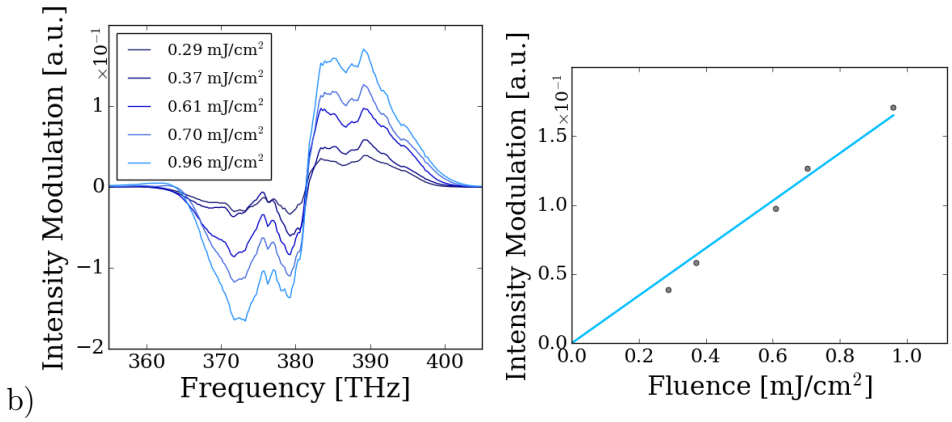

Figure 4.14: Pump intensity dependent results.
Energy profiles of oscillation at fixed delay (left) and fit of the maxima (right).
a) Refractive effect (selected delay = 102 fs).
b) ISRS effect (selected delay = 62 fs).

Probe Intensity Dependence

The probe intensity dependence is studied in a fluence range of $0.20 - 3.25\ \mu\mathrm{J/cm^2}$, with a constant pump fluence of $0.81\ \mathrm{mJ/cm^2}$.

Analogously to the pump case, we analyze the modulation of the pulse spectrum, as a function of the probe intensity. We select two different pump&probe delays in order to distinguish between the transmittivity and ISRS effect.
In the first case, (fig.4.15a) we fit the maximum amplitude in the central part of the pulse. In the other one (fig.4.15a) we focus on the high-energy side of the pulse.
As can be seen from the fits, the linear dependence of the signal on the fluence is well demonstrated.

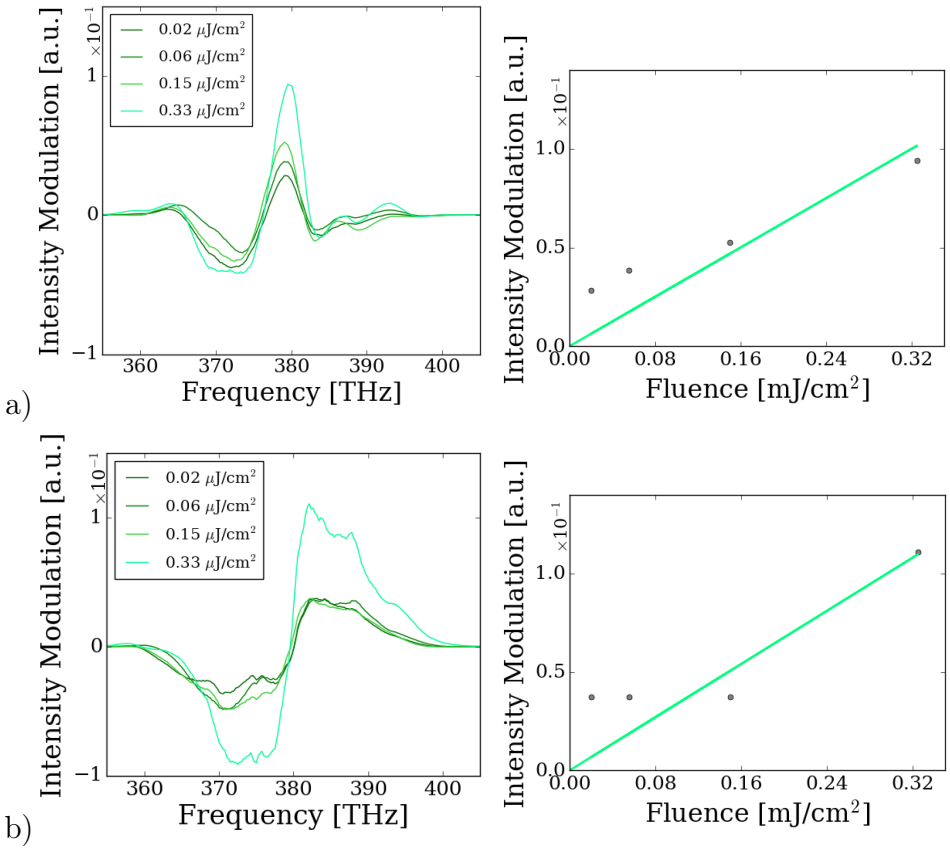

Figure 4.15: Probe intensity dependent results.
Energy profiles of oscillation at fixed delay (left) and fit of the maxima (right).
a) Refractive effect (selected delay = 163 fs).
b) ISRS effect (selected delay = 103 fs).

4.4 Polarization Dependent Measurements

In this section, we focus on the symmetry properties of the system. We exploit the selective polarization geometry of the experimental setup. The degrees of freedom we are working with are the relative angle between pump and probe incident polarization and the transmitted probe polarization. Given a specific configuration of these, the third order susceptibility tensor indicates whether a phonon mode of a definite symmetry is observable or not. We remind that in the α-quartz sample considered we have two different symmetries (A and E). The relative tensor is expressed in eq. 4.3. As already repeatedly written, the pump&probe process re-

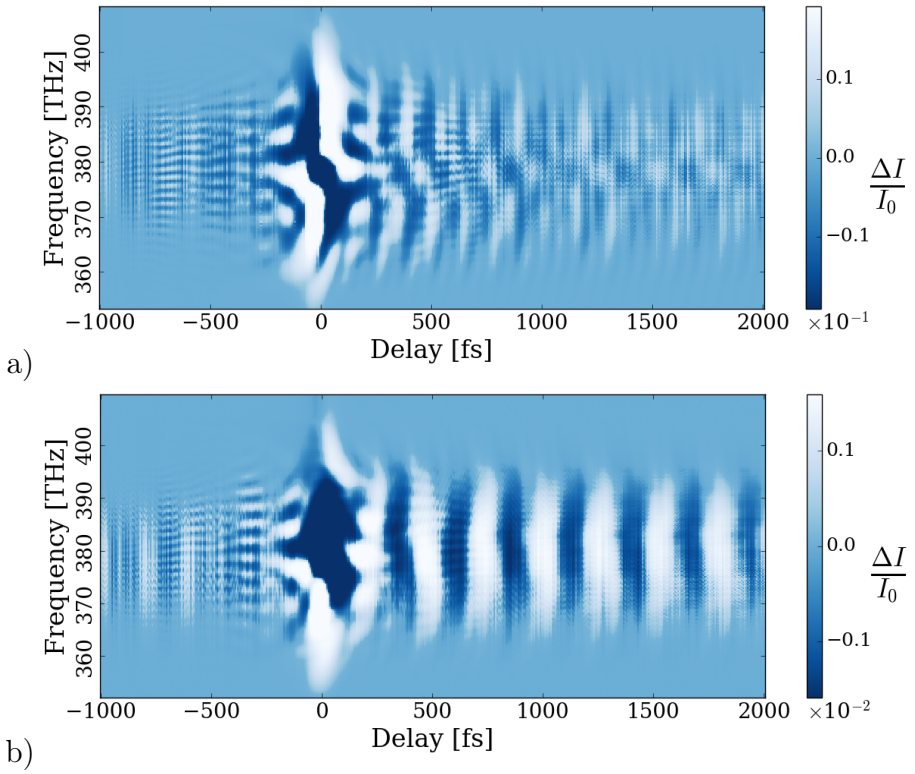

Figure 4.16: Polarization dependent measurements.
Results depending on the relative orientation between pump, probe and polarizer. The delay-frequency map of two different probe polarization configurations are presented. a) Parallel polarization b) Orthogonal polarization.

sults in two effects felt by the probe pulse. One is the modulation of the refractive index of the sample. The other the resonant ISRS, which consists in an energy exchange between probe pulse and phonon. The latter effect involves a redistribution of the photons in the probe energy

spectrum (red/blue-shift), but their polarization is unaltered. The first, instead, changes the refraction properties. In case of non-totalsymmetric phonon modes the polarization of the transmitted probe can be rotated. Taking into account the theory of chapter 2 and the properties of quartz susceptibility, we can predict the visible features. We do this for a set of particular configurations, which are reported in table 4.1. As a function of the angles between pump-probe and probe-analyzer, we specify the symmetry of the observable modes. In addition, we indicate whether the ISRS effects are present or not.

pump-probe angle [°]	probe-analyzer angle [°]	Tensor element	ISRS
90	0	$a^2 - c^2$	$\surd$
90	90	0	$\times$
67.5	0	$\frac{1}{2}(a^2 - c^2)$	$\surd$
67.5	90	$\frac{1}{2}c^2$	$\times$
45	0	a^2	$\surd$
45	90	c^2	$\times$
22.5	0	$\frac{1}{2}(a^2 + c^2)$	$\surd$
22.5	90	$\frac{1}{2}c^2$	$\times$
0	0	$a^2 + c^2$	$\surd$
0	90	0	$\times$

Table 4.1: In table are reported the detectable features as a function of the specific configuration: relative angle between pump-probe and probe-analyzer. They are formulated with reference to the theory of chapter 2 and the data relative to the quartz susceptibility.

As mentioned above, to set the analyzer in the probe extinction regime is a good way to filter out the ISRS features. Furthermore, α-quartz E symmetry modes are non total-symmetric and they cause a polarization rotation. Then, this means that measuring the cross polarization in changing polarization configuration allows to detect only refractive effects.
The peculiar condition to do so is with pump-probe angle 45°, because the considered mode results from the interaction between a parallel and an orthogonal pump field.
In fig. 4.16, measurements in this setting are presented. The two maps refer to analyzer parallel (a) or orthogonal (b) to the incident probe.
It is evident how the red/blue-shift modulation due to ISRS is reduced in (b). In addition, we highlight that in (a) both A and E symmetry phonons are visible, while in (b) only the E are selected.

We complete the study of the characteristic configurations proving the dependence in the pump-probe angle.
The total-symmetric A mode signal is constant, with no dependence on the system geometry. The E symmetry, instead, is sensitive to it.
The E symmetry phonon detected in our measurements is the 4 THz one.

We collect data for different pump-probe angles, in both analyzer settings. We calculate, as usual, the amplitude of the Fourier Transform along the delay axis, averaged over all pulse energies. The obtained photon frequency spectra are shown in fig. 4.17. It is clear that the only angle dependent signal is the one of the E phonon.

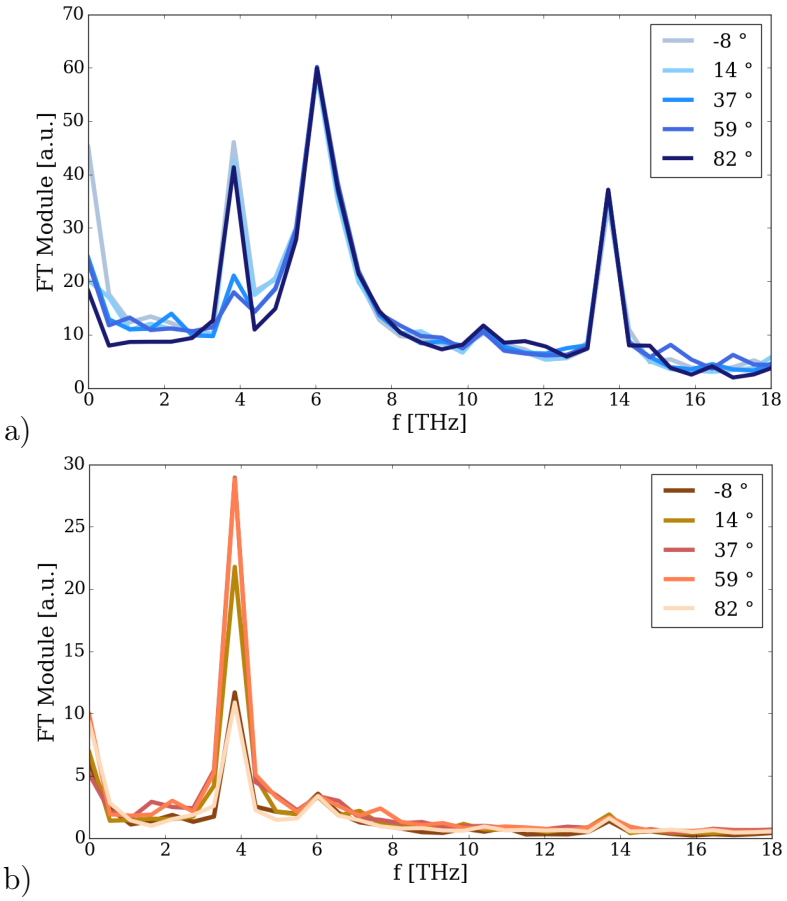

Figure 4.17: Pump-probe relative orientation dependence in the two probe polarizations configurations.
The Fourier Spectrum obtained in each different configuration is presented.
a) Parallel polarization b) Perpendicular polarization.

For each pump-probe geometry, the maxima of the 4 THz E mode and of the 6 THz A mode are identified. These data are fitted with an

ideal squared sinuosoidal function. The measured points and the fits are shown in fig. 4.18. They are presented in the form of polar plots to make symmetry angular dependence clear.

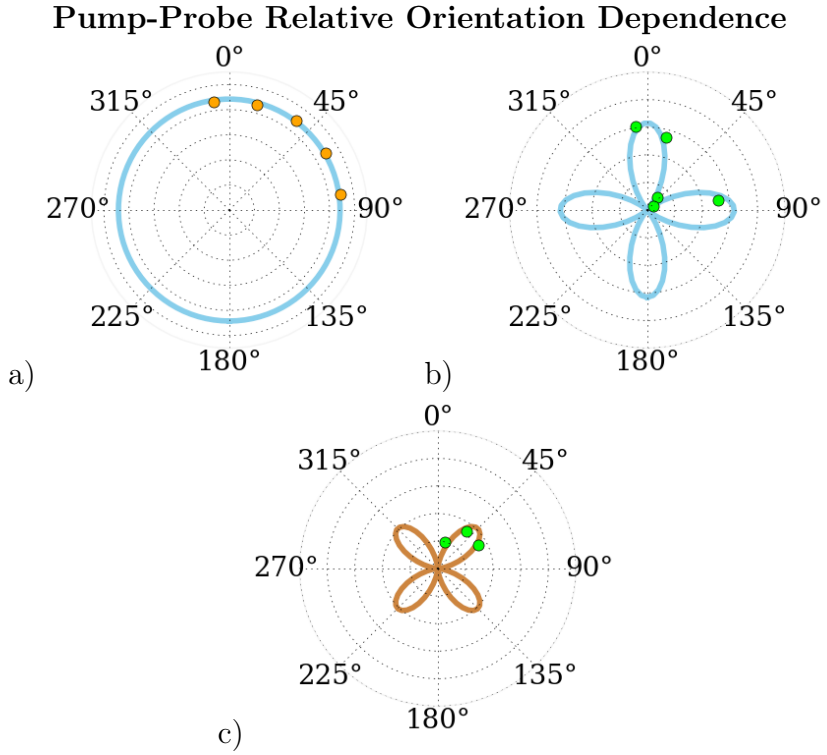

Figure 4.18: Polar plots representative of the different phonon symmetries are presented for an analizer setted parallel (a,b) or ortogonal (c) to the probe polarization (cross). Fit of the angular pump-probe dependence of the Fourier module (line) and measurements (dots) are shown. a) A-mode 6 THz phonon, b) E-mode 4 THz phonon; parallel polarization. c) E-mode 4THz phonon, cross polarization.

4.5 Chirp Dependent Measurements

The ISRS is the fundamental physical process in our experiment. It is the responsible of the phonon excitation by the pump pulse. It also rules the probe interaction with the sample.
The ISRS process is deeply related with the multimode nature of the ultrashort laser pulses employed. Actually, it is due to the interaction between couple of modes at an energy difference resonant to the phonon one.
In an ideal tractation, the different energies of the pulse spectra are treated as time coincident, or at least compressed up to the uncertainty principle limit (Fourier Transform Limited). In the following, we go beyond this approach and study the time domain response with pulses with a controlled chirp. We observe what occurs in the measurements if the frequency in the pump/probe spectral content are separated in time, while maintaining their relative coherence. This is achieved exploiting the compressor of the laser amplification system.

The instrument considered is able to delay the longer wavelenghts of the pulse with respect to the shorter ones, or vice versa. We will refer to "minimum chirp" as the condition in which the pulse has the shortest duration and it is nearly Transform Limited. Then, when the low energy components are placed before the high ones the pulse is defined to have a "positive chirp". Conversely, it has a "negative chirp".

Another key element of this analysis is the autocorrelator. It measures the temporal coherence of the laser pulse. Owing to the fact that introducing a chirp preserves the coherence, it indeed quantifies the pulse duration.

The presented measurements are collected for different chirp/duration values. The considered range is quite wide and spans from -7.5 to + 7.5 ps. The zero chirp value is 56 fs. Data are acquired with same pump and probe pulse lifetime.
Examples of the data obtained are presented in fig. 4.19- 4.20.

The pump&probe maps show very clearly that there is a modification in the shape of the signal. The stripes that at the minimum chirp are vertical tilt forward/back in case of postitive/negative chirp. In particular, we notice this effect to be proportional to the pulse duration.
This is quantified evaluating the slope of the signal lines, fitted as a function of the pulse duration, subtracted by the zero chirp one (fig. 4.21).

We remind that the considered data were acquired with equally long

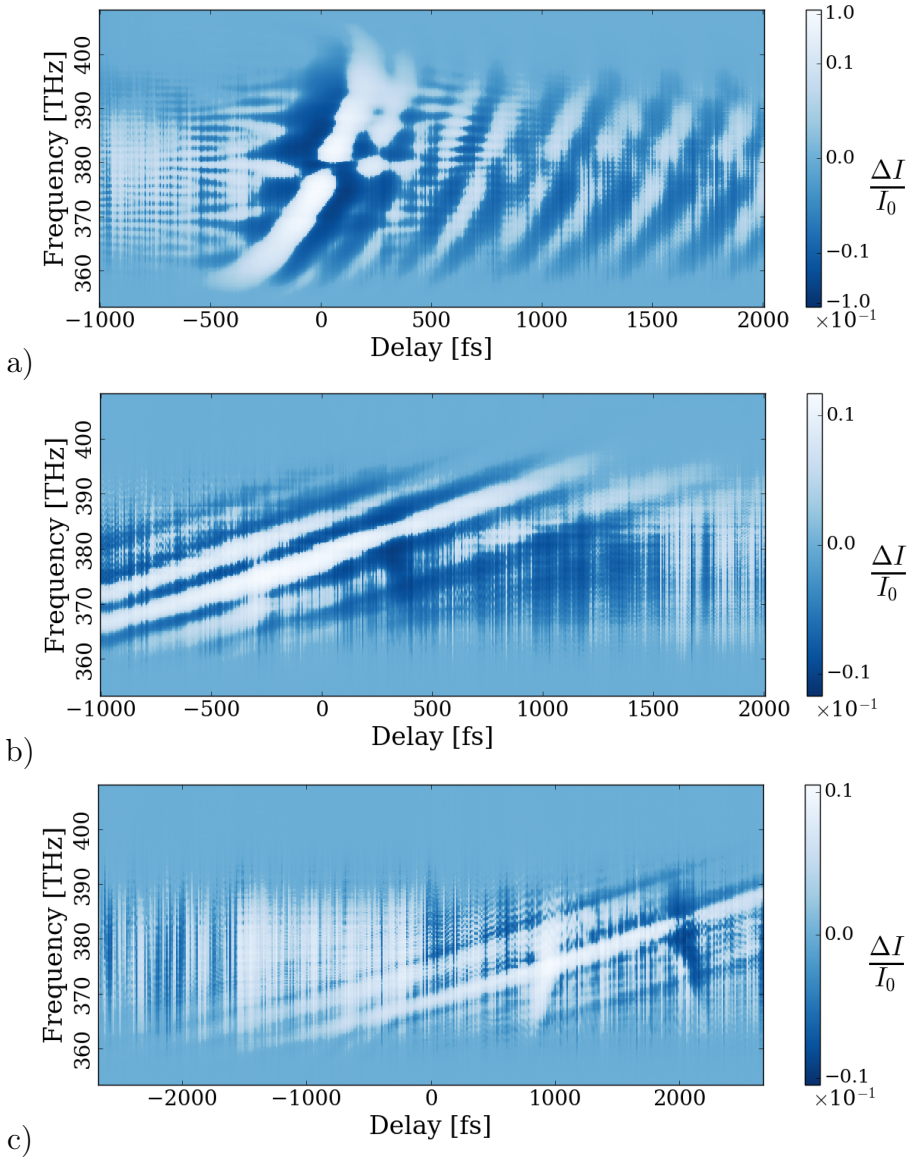

Figure 4.19: Examples of Positively Chirped Measurements.
Pulse lenght: a) 200 fs b) 1.5 ps c) 3.0 ps.

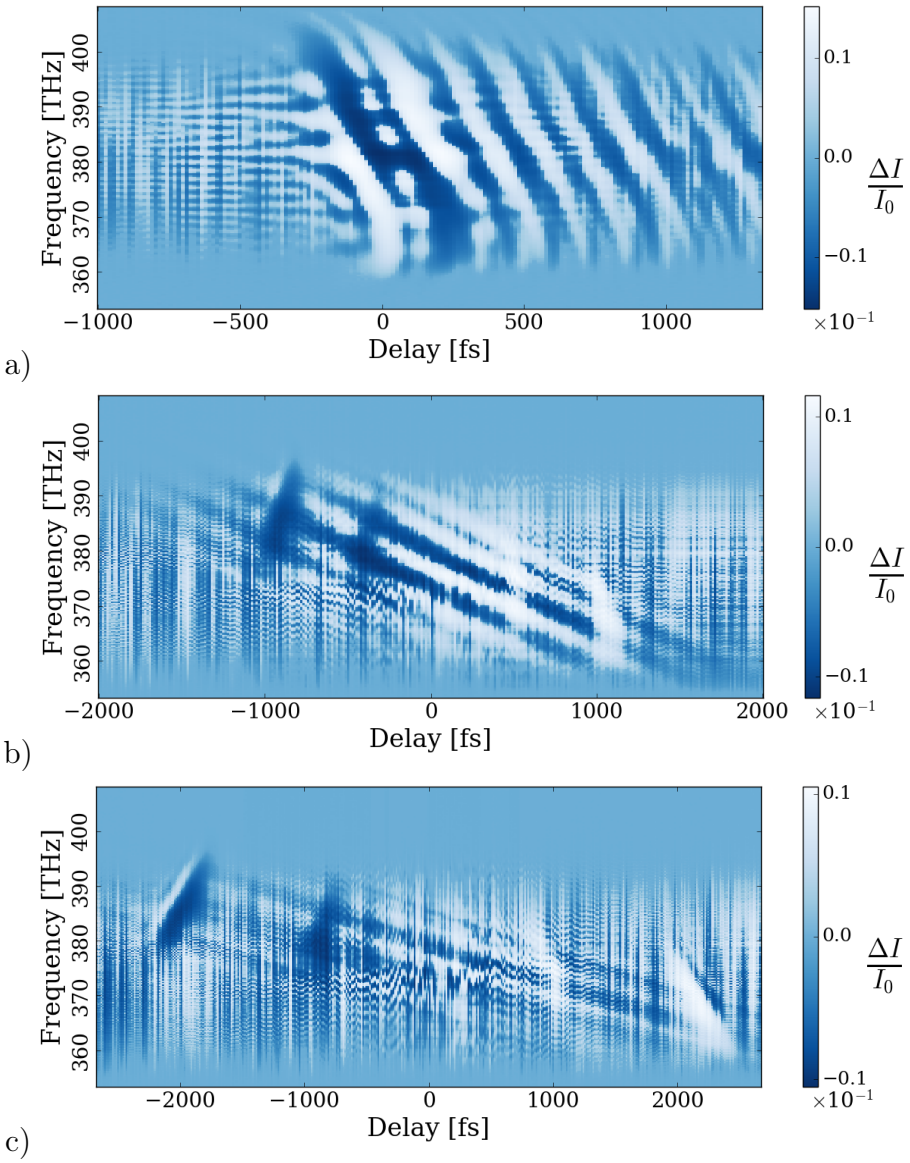

Figure 4.20: Examples of Negatively Chirped Measurements. Pulse lenght: a) -200 fs b) -1.5 ps c) -3.0 ps.

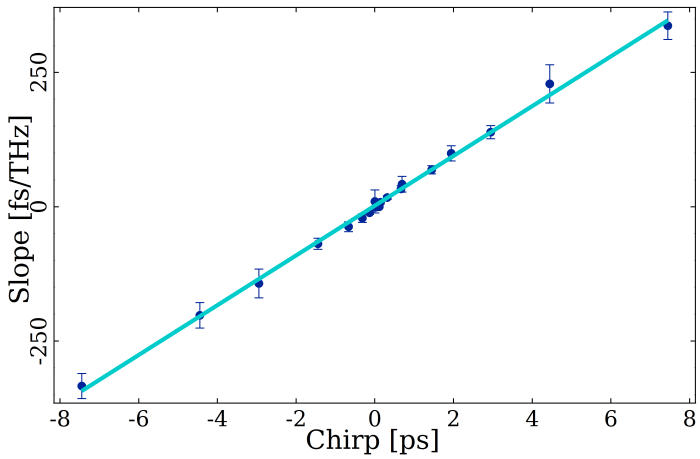

Figure 4.21: The tilt of the stripes representing the pump&probe signal is reported as a function of the chirp. A linear relation is well verified by the performed fit.

pump and probe. In order to recognize which is causing the observed effect, we unbalance the two. We do it introducing a thick glass (1/2 cm) in one of the two beams. In fact, the wavelength dependent refraction in the added component changes the time compression of the transmitted pulse.
This method allows to obtain a time difference of few hundreds of femtoseconds. So with high chirp values the two pulses have relatively similar lifetime. Two distinct compressors are needed to perfom this kind of study in that range.
Nevertheless, the time difference achieved is enough to identify the probe as the responsible of the tilt effect. We see in fig. 4.22 that with short pump and chirped probe the slope changes. Conversely, with long pump and minimized probe the stripes are vertical. In the latter case, an overall decreasing of the signal intensity is noticed.
The tilt can be explained considering modes with the same phase interacting with the sample in a similar way. Hence, their signal amplitude are related and together they produce a line. It is vertical if they have all the same delay, it is rotated if they are chirped.

The description of the excitation process by means of a long pump pulse is not so straightforward. Reasonably, the signal decreases because the pulse energy is distributed over a wide time interval. However, as a consequence of this the pump&probe effects are more difficult to study. In particular, for the longer chirp values, they are detected only in the time interval where pump and probe overlap. This region is usually neglected

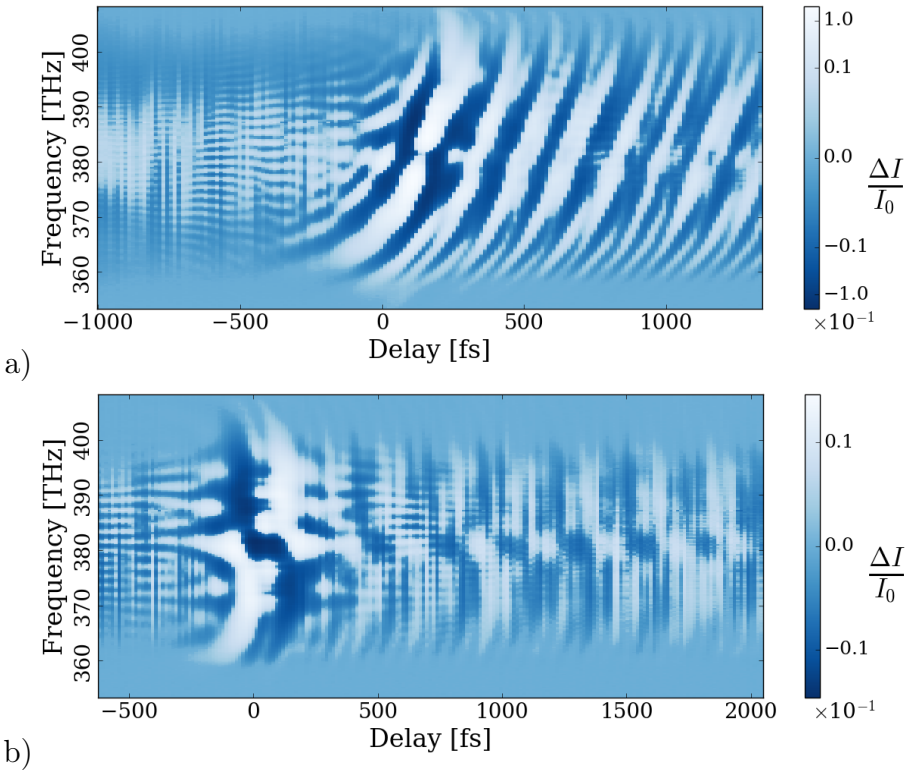

Figure 4.22: Distinction between the effects of separately chirped pump and probe. a) Chirped probe b) Chirped pump.

in standard studies, due to the complications arising from interference effects between the two pulses.
Therefore, it is very difficult to obtain some definite information.

Despite this, we notice very roughly a trend in the Fourier Transform spectra, obtained along the delay axis. The peak positions seem to move towards lower frequencies as the pulse duration increases. Fig. 4.23 shows this behaviour. We guess it is a feature of the continuous excitation during the pump-probe superposition time. We could try to verfiy it applying the theoretical models of chapter 2 outside of the impulsive limit. Anyway, this would require some further calculation we do not perform in this thesis work.

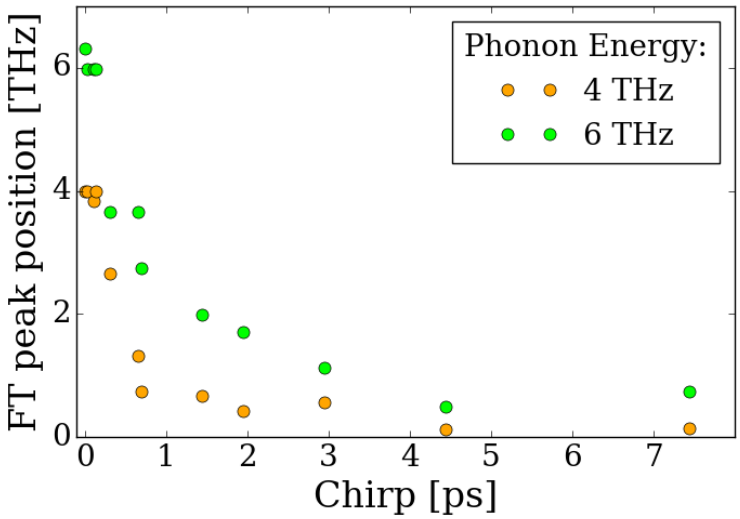

Figure 4.23: The position of the peaks in the Fourier specturm are reported against the pulse duration. It can be noticed that frequency lowers increasing the chirp.

Chapter 5

Statistical Analysis of Correlation

Ultrashort light pulses are characterized by a broad multi-mode frequency spectrum. To each mode correspond an intensity, which is the fundamental object of the study we are presenting.
The aim is to investigate with a statistical approach whether the intensities of the various frequencies inside the pulse are dependent to each other, namely if there are some correlations among the different modes. The inspiring idea is the fact that intensity correlations should arise in a mutimode pulse due to interaction processes with matter. In particular, we consider the ISRS process, which involves an energy exchange between a couple of photons with a specific frequency difference. In detail, in our case this difference is the energy of the sample phonons.
Hence, the final goal of this work is to exploit the correlation properties in order to develop a spectroscopic technique, the *Noise Correlation Spectroscopy*.
As suggested from the title, due to the statistical character of the performed analysis, we study the properties and role of the stochastic fluctuations involved.

In this chapter, we start giving the definition of correlation from the statistical point of view. At first we apply the analysis to the non-interacting (reference) light pulses. Once we have under control the unperturbed condition, we focus on distinguishing the peculiar features introduced in the light pulse by ISRS. In particular, controlling the intensity fluctuations in a proper way we will retrieve informations about the phonon spectra of the examined sample.

5.1 Correlation coefficient 2-D map

We introduce the mathematical tool employed for the statistical analysis. It is the correlation coefficient, ρ, evaluated between two stochastic variables. In the present case, the considered variable is the intensity $I(\omega)$ associated to a mode of frequency ω. From the experimental point of view, it is the signal detected by a single photodiode in the array.
Therefore, the correlation coeffcient between the intensities relative to a couple of frequencies ω_i and ω_j is

$$\rho\Big(I(\omega_i), I(\omega_j)\Big) = \frac{< I(\omega_i)I(\omega_j) > - < I(\omega_i) >< I(\omega_j) >}{\sigma_i \sigma_j} \tag{5.1}$$

where the brakets denote the mean over the single-shot repetitions, and the σ is the standard deviation relative to the considered dataset. Including the σ at the denominator normalizes the coefficient in such a way that $-1 < \rho < +1$.

The correlation coefficient quantifies how much two variables are dependent from each other.
Independent variables have zero correlation coefficient. It must be made clear that care must be taken as the reverse is not always true; i.e. a null correlation does not imply independence. Anyway, this goes beyond the purpose of our discussion.
Correlation has got a sign attribute. Its interpretation is easier expanding the stochastic variable around its mean-value $I(\omega) = \bar{I}(\omega) + \delta I(\omega)$, so that ρ can be rewritten

$$\rho\Big(I(\omega_i), I(\omega_j)\Big) = \frac{< \delta I(\omega_i)\delta I(\omega_j) >}{\sigma_i \sigma_j} \tag{5.2}$$

where we used the assumption $< \delta I(\omega) >= 0$.
It is positive if to a positive/negative fluctuation (greater/lower than average) in the first mode corresponds a positive/negative one in the second ($\delta I(\omega_i)\delta I(\omega_j) > 0$). Conversely, we have negative correlation if the fluctuation in the second is of the opposite sign ($\delta I(\omega_i)\delta I(\omega_j) < 0$).
In detail, $\rho = +1$ indicates a perfectly linear dependence between the two variables, $\rho = -1$ an inverse proportionality. An explicative scheme sums up the discussion in fig. 5.1.

Our experimental setup is designed for frequency-resolved measurements. This means that we can distinguish multiple modes. In particular, we can do it up to 256 (number of diodes in the experimental apparatus).
Calculating the correlation coefficient ρ for all the possible couples we

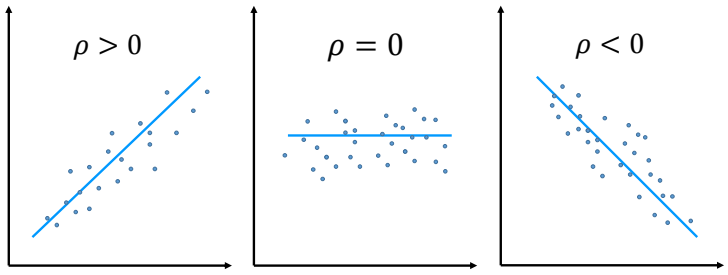

Figure 5.1: Correlation coefficient as a function of the dependence between the two considered variables. A positive correlation indicates that the two increase or decrease together. Instead, a negative correlation is relative to quantities with opposite trends.

obtain a symmetric 2-D map. The two axis are both the same frequency scale. Practically, with our spectrometer we obtain a 256x256 grid.
In the following, we will adopt a colourscale where negative correlation values are indicated in blue, positive in red and the part around zero in white.

Finally, in order to start to be familiar with the correlation map tool, we show a simple example in fig. 5.2. It is a case involving a set of independent variables. As a consequence of this, most of the map is null. Nevertheless, notice that the diagonal has always a correlation coefficient equal to +1 by definition. In fact, there is considered the trivial correlation between each mode and itself.

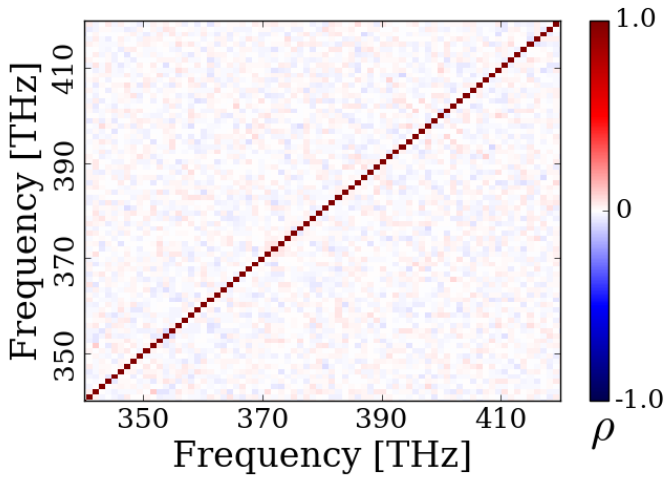

Figure 5.2: Example of 2-D correlation map.
Precisely, the one plotted is relative to a perfectly uncorrelated situation: the whole map is zero, besides the diagonal (=+1 by definition).

5.2 Noise Analysis of the Reference Pulse

In this section, we start applying the statistical analysis of correlation to investigate the properties of the incident pulse. It is a preliminary study, useful to distinguish later the features peculiar of the light-matter interaction. Nevertheless, it is also an interesting tool to perform pulse diagnostic, through which obtain informations on the present fluctuations. Furthermore, to characterize these is very important also for spectroscopic purposes. In fact, as we will see, the results obtained are deeply relying on the typology of noise.

5.2.1 Noise Simulation

The proposed analysis bases on the frequency-resolved intensity spectra of the ultrashort light pulses, namely $I(\omega)$. We assume the mean value of the incident spectra to have an ideally gaussian shape. The parameters that describe it are the central frequency ω_0, the width σ_0 and the amplitude I_0.

On the base of this, we simulate single-shot measurements spectra implementing stochastic fluctuations of the average intensity profile. We consider two main categories of noise. We define as "correlated noise" all the fluctuations that preserve the gaussian shape of the pulse. On the contrary, we dubb "uncorrelated" all noise modifying the gaussian profile.

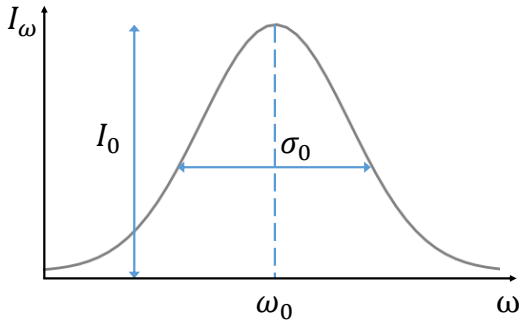

Figure 5.3: Schematic average frequency-resolved intensity spectrum of the incident pulse. The parameters of the ideal gaussian shape are indicated.

The correlated one is implemented adding a random shift to each of the gaussian parameters, namely $\delta\omega_0$, $\delta\sigma_0$ and δI_0. In order to account for the uncorrelated one we consider a more general expression, $\delta u(\omega)$. It is the sum of various independent fluctuations, each centered around

a different frequency ω' of the spectrum.

$$\delta u(\omega) = \sum_{\omega'} \delta(\omega;\omega') \tag{5.3}$$

We can describe these single variation as gaussian:

$$\delta(\omega;\omega') = I'(\omega') e^{-\frac{(\omega-\omega')^2}{2[\sigma'(\omega')]^2}} \tag{5.4}$$

The width σ' is a parameter that indicates the partial frequency range over which the single fluctuation spreads. If it is very short[1] the spectrum results very jagged, conversely if it is wide the intensity profile is smooth. We notice that this will be a key factor in determining the resolution of the NCS technique.

In summary, the simulated incident intensity spectrum of a single-shot acquisition is

$$I(\omega) = (I_0 + \delta I_0) e^{-\frac{(\omega-(\omega_0+\delta\omega_0))^2}{2(\sigma_0+\delta\sigma_0)^2}} + \delta u(\omega). \tag{5.5}$$

In fig. 5.4 we present the various typologies of simulated noise. These

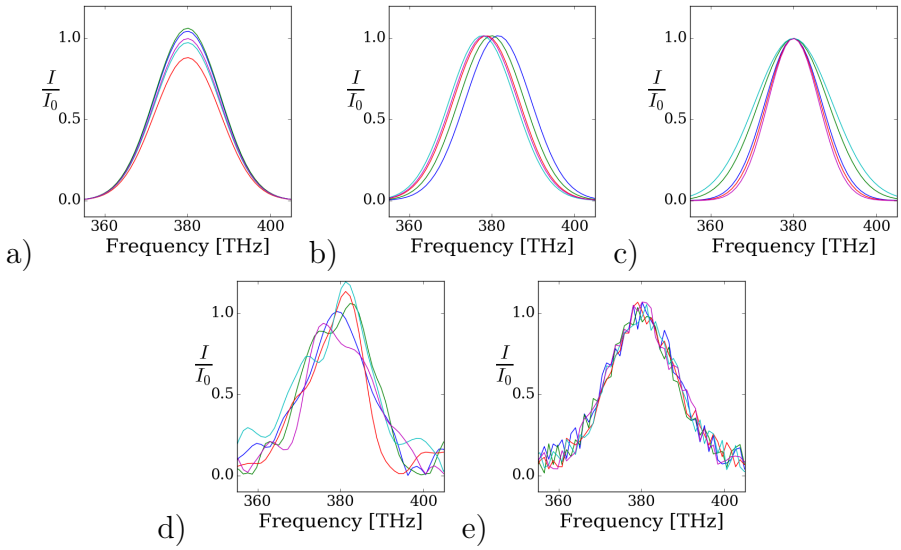

Figure 5.4: Examples of various simulated intensity fluctuacting spectra. Top: correlated noises on amplitude, width and frequency. Bottom: long range and single-mode wide uncorrelated noise.

examples are obtained introducing each contribution separately. All the correlated fluctuations and two regimes of uncorrelated noise are reported.

[1]The minimum width is obtained considering an independent random fluctuation for every single mode (pixel) of the radiation considered.

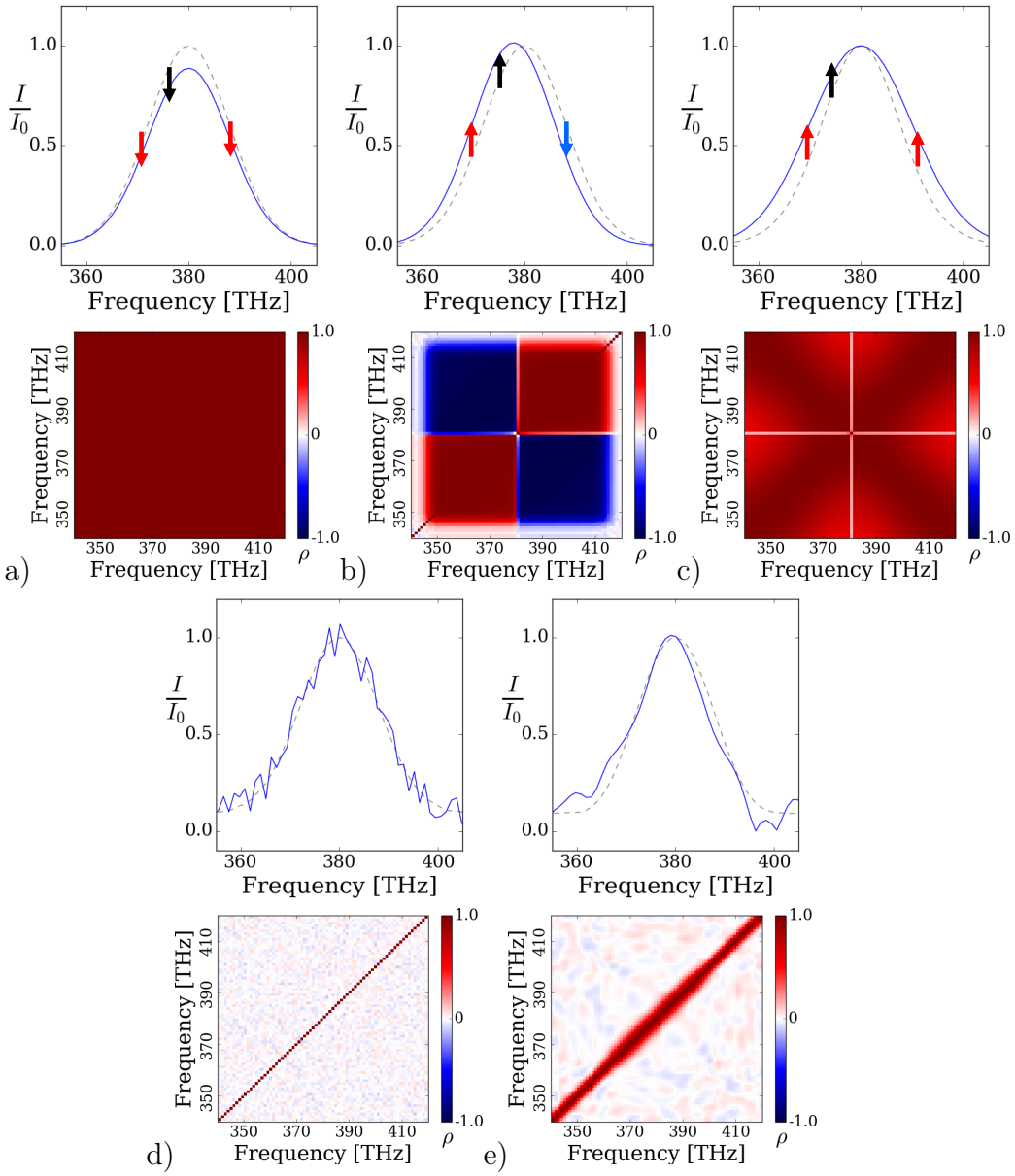

Figure 5.5: Scheme of the typical fluctuations and relative correlation map. Correlated noises (a) amplitude, b) frequency, c) width) and uncorrelated noises(d) short correlation, e) long correlation) are presented.
The correlated noises maps are interpretated in this way: the arrows account for the shift sign with respect to the average profile. With respect to a fluctuation at an arbitrary point (black), we see wheter the modes on the two different pulse sides are positively (red) or negatively (blue) correlated.

Now that we are able to simulate a dataset of single-shot spectra, we can perform on it the statistical analysis of correlation. We calculate for each noise typology the 2-D correlation map. We observe that the outcome strongly depends on the kind of noise involved. The results are shown in fig. 5.5.

These maps can be interpretated considering the way a single measure differs from the average intensity profile.
The amplitude noise has a totally positively correlated map, because all the modes have an intensity shift of the same sign. The frequency jitter presents a chequered map, with four main squares. Two of them are positive and they link modes on the same side of the average gaussian profile. On the contrary, the negative ones link two different sides of the pulse, which have fluctuations of opposite sign. The width case is similar to the amplitude one, but the fact that the variation is null at the center of the pulse.
In both the considered uncorrelated noise examples we can observe that, besides the +1 diagonal, everywhere the correlation coefficient oscillates around zero. Comparing the two regimes, we notice that these oscillations present as spots. They extend over a larger region of the map if the fluctuation width correlates a wider range of frequencies. In particular, in the limit of fluctuations associated to a single mode, the size of the spots is point-like.

5.2.2 Noise Measurements

We now complete our discussion about the incident pulse noise properties. We consider the experimental data and compare them to the previously predicted results.
The simulations shown before are obtained introducing separately the different noise typologies. Actually, the real pulses present a mixture of these. One of the goals of this section is to understand the relative weight of each noise contribution inside the measured pulses.

The experimental dataset is obtained acquiring repeated single-shot frequency-resolved intensity spectra of the reference beam. We usually work with 1k-10k repetitions.
Starting from these data, we calculate the 2-D correlation map, shown in fig. 5.6(a3). We notice that the overall outcome is very similar to the amplitude noise simulation. As a consequence of this we can claim that the amplitude fluctuations are prevailing in our setup. The correlation is vanishing at the edges, due to the presence of uncorrelated noise. Indeed, it is relevant at the low intensity tails of the pulse. We show this point introducing in the simulations a small uncorrelated contribution.

The relative map is reported in fig. 5.6(a2). In order to see whether also other kind of noises are present we have to find a way to remove the amplitude one that is hiding them.
We start calculating the average intensity spectrum over the dataset. We fit it with a gaussian function and estimate its amplitude I_0. Then, we fit each single-shot measurement and obtain the relative amplitude parameter I. After that, we apply to the single-shot data a transformation which is a function of I. In detail, we rescale the spectrum multiplying it by I_0/I. Hence, in the end every spectra has the average amplitude I_0 and so the amplitude fluctuation are cancelled.
Evaluating again the correlation map with the rescaled dataset leads to the result shown in fig. 5.6(b3). It is clearly a map representing the correlations arising from mainly frequency-noisy pulses. The corresponding simulated map, obtained adding also contribution from the uncorrelated noise, (fig. 5.6(b2)) confirms this.

Analogously, we can extend the noise filtering procedure also to the frequency kind. This time the relevant fit parameter is the central frequency ω_0. The transformation to apply to the single-shot measurement centered in ω is a frequency shift $+\omega_0 - \omega$. We notice that in most cases the shift parameter is smaller than the minimum frequency distance between two modes, so to have an effective correction an interpolation procedure is needed.
The result is a correlation map typical of the width noise (fig. 5.6(c3)).

Finally, also the width noise can be removed fitting the σ parameter and transforming the data stretching or narrowing the frequency scaling to reach the average σ_0. Also in this case interpolation of the axis is needed.
The outcome is reported in fig.5.6(d3). We are expecting a completely empty map. However, some features are still observable. Anyway, the noise filtering process are not perfect and the effects of some correlated fluctuation can also be seen. Furthemore, there are present also some correlations introduced by the electrical noise of the detectors. These can be observed acquiring measurements of the empty background.

In conclusion, the simulated noise dependent correlations have been verified. In addition, we characterized the noise properties of the employed laser pulses. We qualitatively observed that the correlated fluctuations are the most relevant (in order of importance: amplitude, frequency, width). The uncorrelated noise, instead, is relatively small.

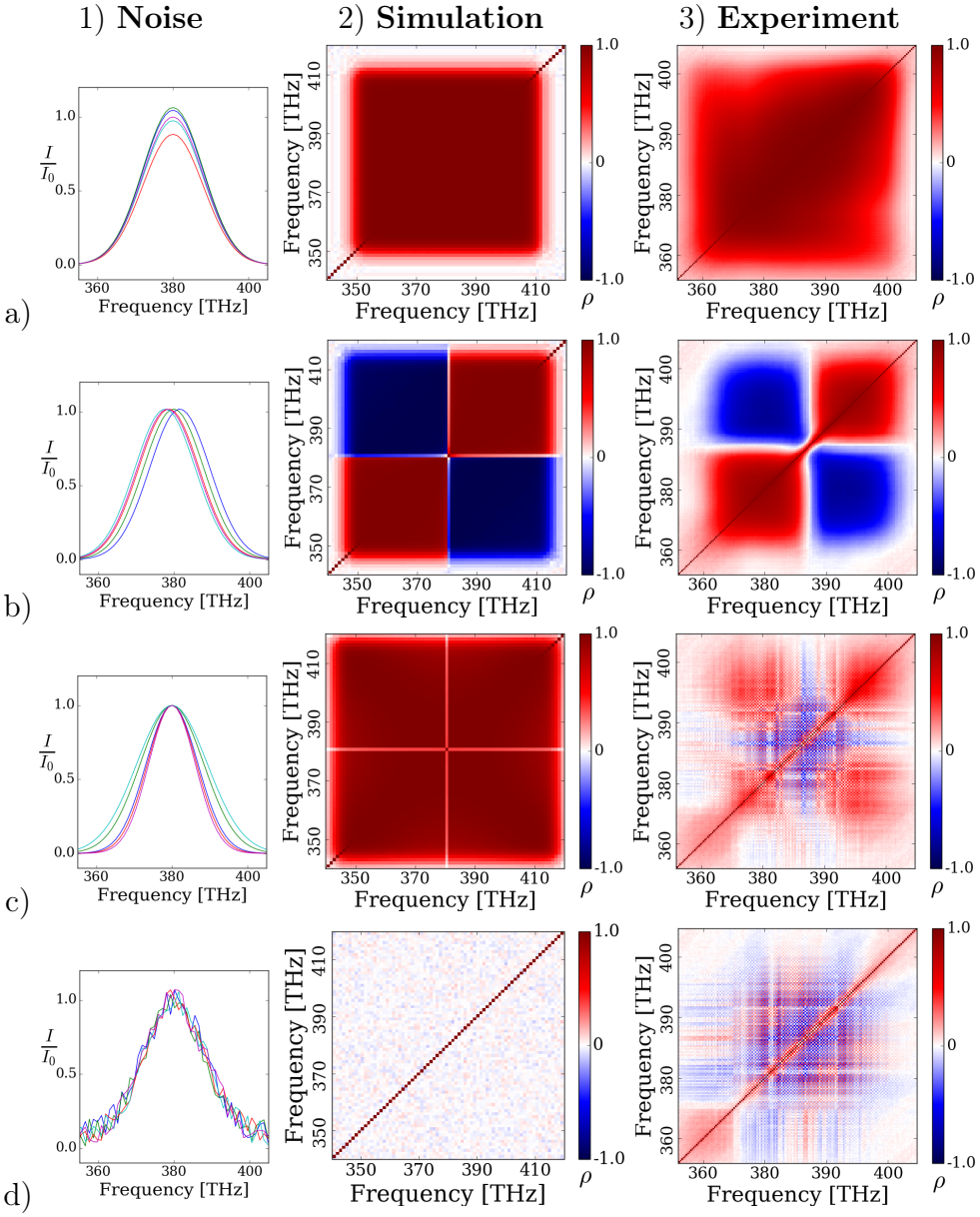

Figure 5.6: Summary of the fluctuations properties of the reference pulse. For each kind of noise, simulation and experimental data are presented. In the simulations a contribution of uncorrelated noise is introduced in order to simulate the experimental noise. The experimental data are obtained filtering one by one in a numerical way each different fluctuation typology.
The reported plot are respectively relative to: a) amplitude noise, b) frequency noise, c) width noise, d) uncorrelated noise.

5.3 Noise Correlation Spectroscopy

In the previuos part of the chapter, we introduced the correlation map calculation and employed it to do a preliminary characterization of the incident pulses. Now, we focus on the pulses transmitted by the sample. The guiding idea is the possibility to retrieve information about the interaction in the correlation map.

As before, the fundamental dataset consists of repeated single-shot frequency-resolved intensity spectra. This time the relevant ones are those of the transmitted pulse. In the present case the main interaction is Impulsive Stimuated Raman Scattering, which involves two photons and a phonon.
Owing to the ISRS process, the intensity of a transmitted photon mode of frequency ω is a function of the two photons at $\omega \pm \Omega$, where Ω is the interacting phonon energy. Hence, the intensities are not independent and correlation between them are introduced.

The reference pulse channel is still taken in consideration and is useful to obtain a clear ISRS signal. Indeed, we would like to distinguish the features peculiar of the ISRS process only. We compare the transmitted pulse map with the reference one in order to remove the common informations. Precisely, we subtract the first to the latter. A block-diagram of the logical steps proper of the NCS analysis is reported in fig. 5.7.

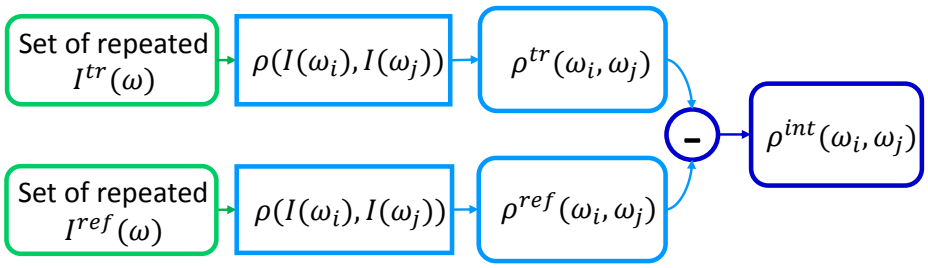

Figure 5.7: Block diagram that sums up the NCS technique.
Repeated single-shot frequency-resolved intensity spectra I are acquired for both transmitted and reference pulse. Correlation coefficient 2D-map ρ is evaluated for each channel. The interaction signal is isolated subtracting the two and the result is the NCS correlation map $\rho^{int}(\omega_i, \omega_j)$.

In the following we explore the spectroscopic capabilities of the NCS. We start with numerical simulations, which we then test experimentally. We remark that, as already done for the non-interacting analysis, we pay attention to the peculiar dependence on the different typologies of intensity noise. In fact, this is a key parameter for the final result.

5.3.1 Simulation of ISRS Transmitted Intensity

In order to better understand the relevant parameters and make some theoretical predictions, we implement the ISRS process in a numerical simulation. We build a function that takes in input the spectrum of an incident pulse, $I^{inc}(\omega)$, and returns the transmitted one, $I^{tr}(\omega)$, after the interaction with the sample.
From chapter 2, eq. 2.43, we have that the ISRS results in

$$I^{tr}(\omega) = I^{inc}(\omega) + k_\Omega E^{inc}(\omega)[E^{inc}(\omega+\Omega) - E^{inc}(\omega-\Omega)] \tag{5.6}$$

where k_Ω is the coupling constant relative to the phonon of energy Ω.
We work in a simplified way, considering the relation expressed in terms of intensities only. In detail, neglecting the phase of the field we can write $E = \sqrt{I}$, so that

$$I^{tr}(\omega) = I^{inc}(\omega) + k_\Omega \sqrt{I^{inc}(\omega)}[\sqrt{I^{inc}(\omega+\Omega)} - \sqrt{I^{inc}(\omega-\Omega)}] \tag{5.7}$$

which is the desired function.
In fig. 5.8 it is shown the above function calculated for the average incident intensity spectrum (considered as a gaussian with amplitude I_0^{inc}.) The coupling constant is chosen in order to obtain a realistic effective shift. A ratio $k_\Omega / I_0^{inc} = \pm 0.2$ is used; positive for the Stokes shift and negative for the Anti-Stokes one.

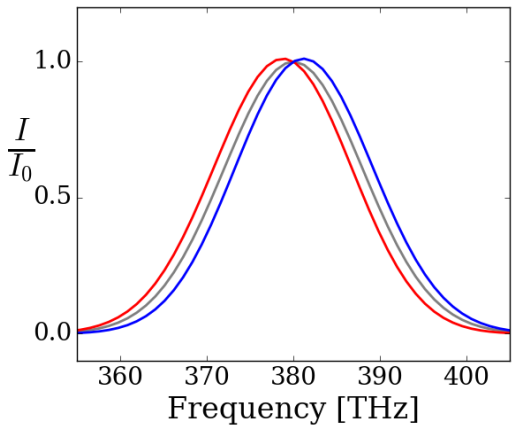

Figure 5.8: Stokes (red) and Anti-Stokes (blue) shifts of the average intensity spectrum simulated with a ratio $k_\Omega / I_0^{inc} = \pm 0.2$. The incident gaussian pulse is plotted in grey.

The input incident pulses are the one used in 5.2.1, with all the different correlated and uncorrelated noise typologies considered. We calculate

a dataset of transmitted pulse for some various fluctuation regimes. Using realistic values for k_Ω, we notice that the transmitted map is at first sight almost equal to the reference one. However, subtracting them a pure interaction correlation map ρ^{int} is obtained. There we observe some clearly distinguishable features. Furthermore, we notice that also these are deeply relying on the peculiar fluctuations involved. In fig. 5.9 we show the noise dependent ISRS maps. The reported examples are just some of the possible results. Differences can easily arise changing the parameters that quantify the weight of each noise.

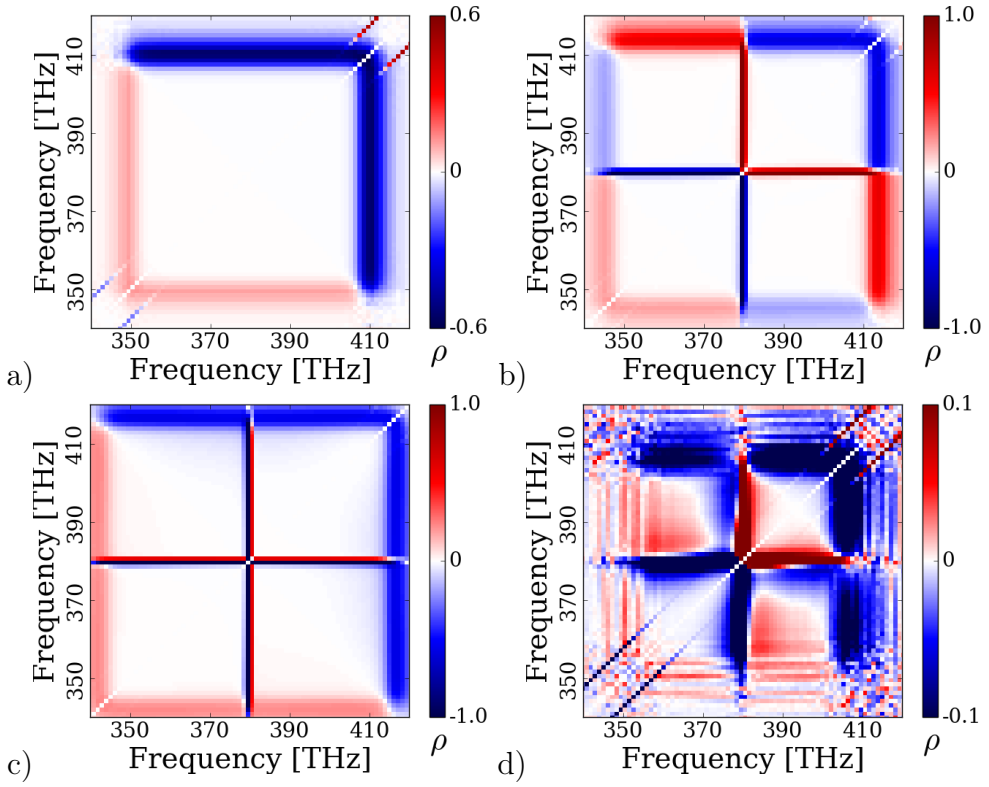

Figure 5.9: Examples of NCS correlation map for different typologies of noise.
a) amplitude+uncorrelated b) frequency
c) width d) frequency+width+uncorrelated

Among these large variety of maps, particularly interesting is the one for the uncorrelated noise, reported in fig. 5.10. Both the Stokes and Anti-Stokes situations are plotted. The considered examples are relative to the ideal case where every mode has independent random fluctuations.
We observe that the correlations emerge only in specific points of the map. They are the one that link couples of modes with a frequency difference corresponding to the phonon one. Therefore, the present cor-

relation map offers a straightforward way to extract the informations about the phonon energy.
Concerning the sign of the correlation, we notice that it is linked with the derivative of the average pulse intensity profile. In addition, it is opposite comparing the Stokes and Anti-Stokes conditions.

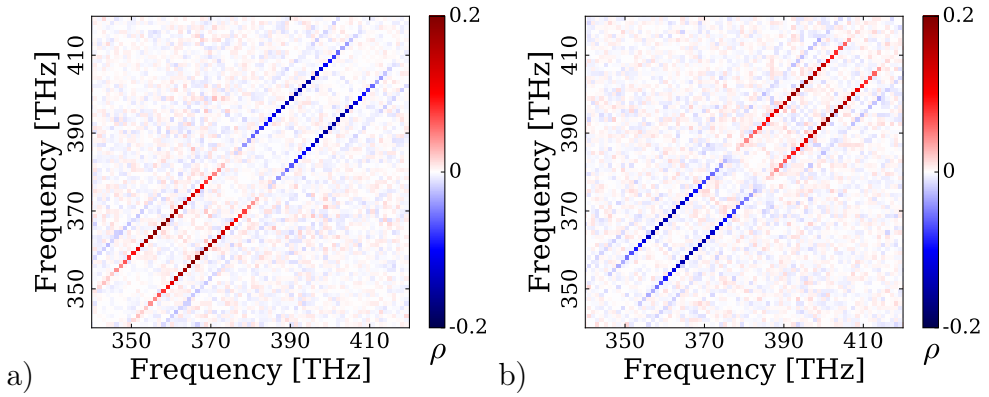

Figure 5.10: NCS Correlation map for pulses with a high uncorrelated noise. a) Stokes process. b) Anti-Stokes process.

From the practical point of view, we underline that in order to obtain this map there is no need to remove the correlated noises, but it is also effective to strongly increase the right noise component, namely the uncorrelated one. What counts is the relative weight of the different fluctuations, that reflects in a characteristic intensity profile of the single-shot measurement.

We refine our simulations in order to verify that the results obtained are not linked to the approximations made.
Firstly, we consider a finite phonon lifetime. As a consequence of this, we integrate over the phonon energies the ISRS term in eq. 5.9. We substitute the previous delta distribution with the relative broad phonon energy spectrum $g(\Omega' - \Omega)$.

$$\begin{aligned} &k_\Omega \int \delta(\Omega' - \Omega)\sqrt{I^{inc}(\omega)}[\sqrt{I^{inc}(\omega+\Omega)} - \sqrt{I^{inc}(\omega-\Omega)}]d\Omega' \rightarrow \\ &\rightarrow k_\Omega \int g(\Omega' - \Omega)\sqrt{I^{inc}(\omega)}[\sqrt{I^{inc}(\omega+\Omega)} - \sqrt{I^{inc}(\omega-\Omega)}]d\Omega' \end{aligned} \tag{5.8}$$

The simulation outcome (fig. 5.11(a)) shows an increasing of the thickness of the correlation line on the map, representative of the phonon natural bandwidth.
A similar effect is also introduced increasing the correlation lenght σ' of the uncorrelated fluctuations (see eq. 5.4). However, this time no further

informations about the phonons are added. The thicker lines visible in fig. 5.11(b) are a smoothing effect due to a poorer resolution. Actually, this means that NCS frequency resolution is limited by the fluctuation correlation lenght.

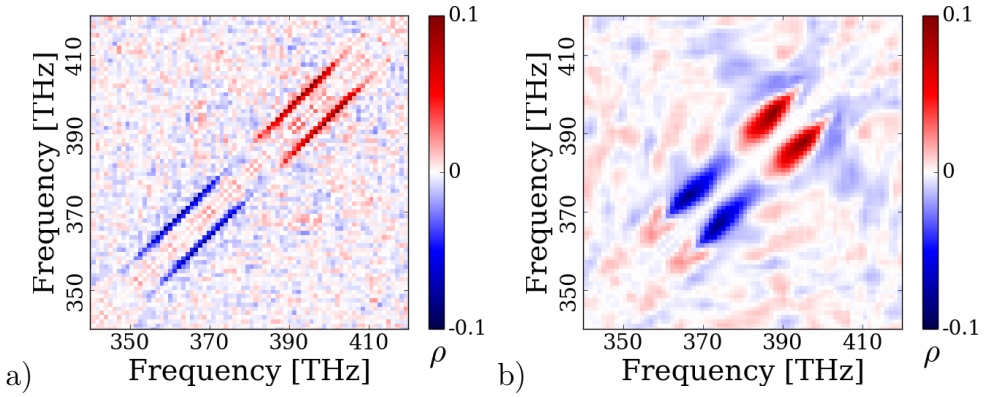

Figure 5.11: NCS Correlation map for pulses with high uncorrelated noise. a) Finite lifetime of the phonon is considered. b) Noise with a correlation lenght broader than the pixel frequency difference is employed.

Until now we have always considered a single-phonon configuration. Anyway, as also seen in chapter 4, we are working in a multiple phonon setting. We generalize our simulation in a trivial way, adding in the original expression 5.9 a sum over the various phonons present.

$$I^{tr}(\omega) = I^{inc}(\omega) + \sum_{\Omega} k_{\Omega} \sqrt{I^{inc}(\omega)} [\sqrt{I^{inc}(\omega + \Omega)} - \sqrt{I^{inc}(\omega - \Omega)}] \quad (5.9)$$

The corresponding simulated map is reported in fig. 5.12.

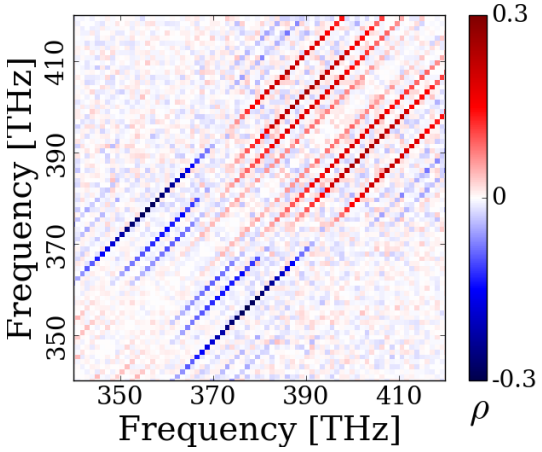

Figure 5.12: NCS Correlation map for a multi-phonon spectra.

In summary, from the several simulations performed we can fix some relevant point. NCS is potentially effective in retrieving the phonon energies involved in ISRS processes. In particular, an essential role is performed by the noise properties. The resolution is limited by the fluctuation correlation lenght, not by the ultrashort pulse bandwidth. So an high frequency resolution can be combined together with an high temporal resolution. Moreover, a multi-phonon spectra should be obtained with a single dataset of repeated measurements, without the need of an energy scan.

5.3.2 Test Measurements on Quartz

In the following, we report the NCS analysis performed on the experimental data. The transmitted pulse spectra are acquired after the interaction with the α-quartz sample. Also the reference copy of the incident pulse is collected.

We find the trace of the ISRS process working with the pump&probe setup (fig. 3.1) used to perfom the mean-value measurements in chapter 4. We choose this configuration in order to enhance the detected signal. Anyway, in principle NCS should also be applicable to the static analysis of the pump pulse. Unlike the static case, the studied probe pulses are preceeded by a pump pulse. Owing to this, the presence of a coherently excited phonon resonantly increases the signal. In addition, the datasets are acquired as a function of the pump-probe delay. This permit to study the dependence on the phase of the coherent phonon. Thus, Stokes or Anti-Stokes ISRS can be selected. Moreover, the resonant ISRS effect can be isolated from absorption effects, by subtracting the measurements at negative pump&probe times.

From the analysis of the incident (reference) pulse, we know that in our setup the correlated noises are prevailing.
The most relevant are the amplitude fluctuations. Indeed, we expect that the NCS on the measured data resembles the corresponding simulations. These are shown in fig. 5.13(b). The two maps are obtained at a proper delay for the Stokes and Anti-Stokes ISRS. Precisely, a blue-shift and a red-shift phase are selected from the pump&probe frequency-delay map (fig. 5.13(a)). We stress that the ISRS pump&probe signal is isolated subtracting the correlation map calculated at negative times.
Following the method used in 5.2.2, we normalize all the pulse in the dataset. So, we filter the amplitude noise in order to show the effects of the remaining ones. The results are shown in fig. 5.13(c).

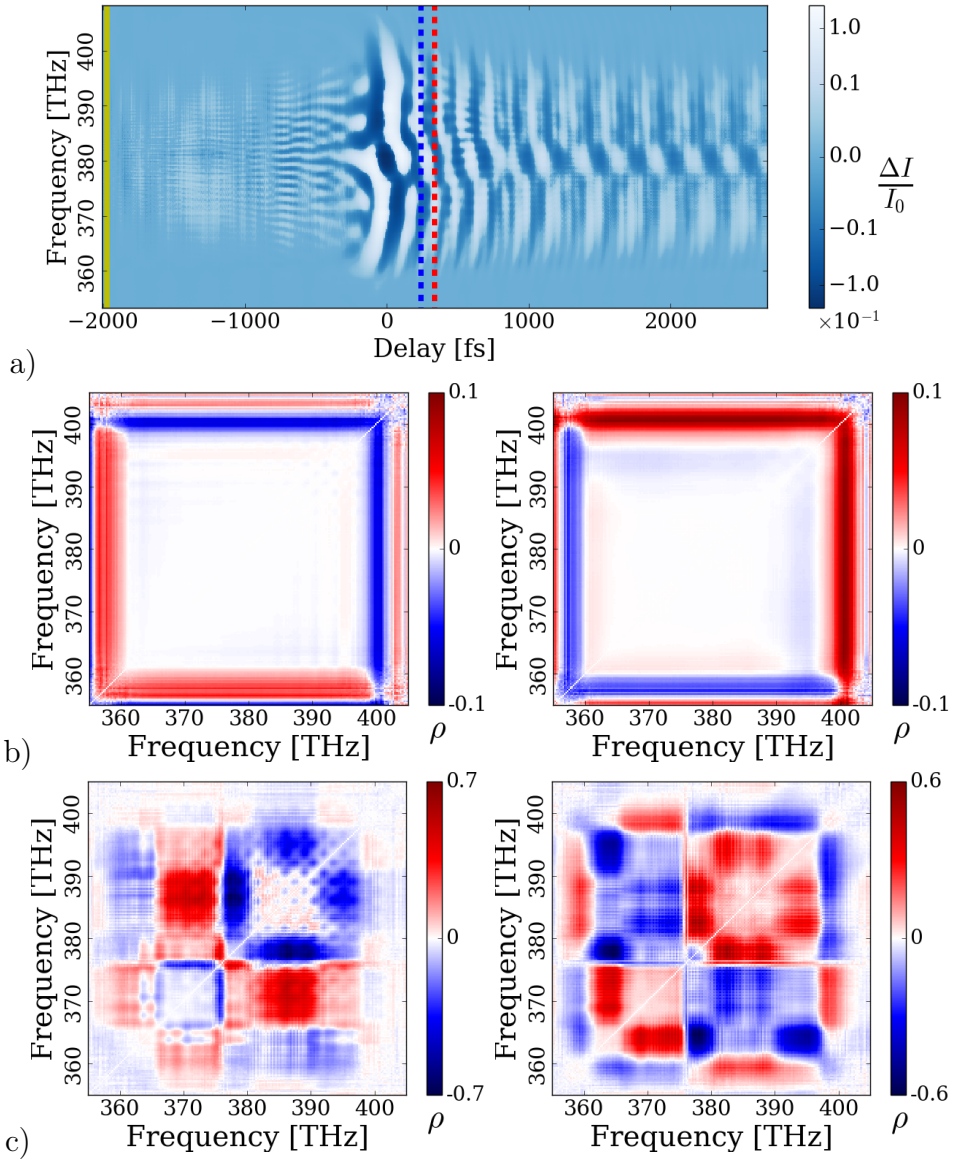

Figure 5.13: Experimental NCS correlation map for different typologies of noise.
a) Pump&probe map. The lines indicate the analyzed delays: +236 fs (Anti-Stokes blue-shift), +337 (Stokes red-shift) and -1973 fs (negative time reference).
b) Amplitude noise Stokes (left)and Anti-Stokes (right) measurements.
c) Frequency+width noise Stokes (left)and Anti-Stokes (right) measurements.

We can compare the present results with the corresponding simulation

in fig. 5.9(a) and (d). The NCS maps have indeed very similar features. Moreover, as shown in fig. 5.10, we experimentally confirm that Stokes and Anti-Stokes exhibit opposite correlation sign.

While for the correlated noises we found results in agreement with the simulations, filtering all the gaussian fluctuations is not enough to appreciate the uncorrelated features. The relative uncorrelated noise is too small, as suggested by the analysis of the incident pulse. For future developments a system capable of increasing this peculiar type of intensity fluctuations is needed.

Conclusions

In this thesis, we explore the possibilities offered by ultrafast time-resolved spectroscopy in studying low-energy excitations. We pay particular attention to the light-matter interaction processes involving ultrashort laser pulses. We model them theoretically and investigate experimentally with standard time domain techniques and the proposed novel spectroscopy named *Noise Correlation Spectroscopy*. In detail, we work with an α-quartz sample and study its coherent vibrational excitations. The setup allows us to perform pump&probe single-shot frequency resolved measurements and it has been specifically realized at the *T-Rex* laboratory at Elettra-Sincrotrone Trieste.
Ultrashort pulses last less than a picosecond. Owing to the Heisenberg uncertainty principle, to this short duration it corresponds a broad spectrum of frequency modes of the radiation. Actually, in this study these peculiar properties are important for various reasons:

- The short pulse duration results in an high time-resolution. This even allows to discriminate between the different definite phases inside an oscillation period of a THz coherent vibration.
- The wide pulse bandwidth permits stimulated excitation of vibrations, thanks to the coupling between photons whose frequency difference matches the phonon one (Impulsive Stimulated Raman Scattering).
- The possibility to perform frequency-resolved measurements of the broad spectrum adds a useful degree of freedom.
- A statistical analysis of correlation inside the multimode pulse can be performed on a set of repeated single-shot frequency-resolved measurements. This allows to retrieve spectroscopic informations about the photon-phonon interaction in an innovative and advantageous way, namely via *Noise Correlation Spectroscopy*.

In our case, the relevant light-matter interaction process is the Impulsive Stimulated Raman Scattering (ISRS).

We exploit it to pump the phonons in the sample and then probe the time-dependent modulation at the phonon frequency. Performing an energy resolved measurement allow us to distinguish the phase of the oscillating signal relative to each photon mode. We see that different regions of the spectrum oscillate with different phase. This allows us to distinguish between two main different effects.

We address them developing a both classical and quantum formalism and we manage also to distinguish them experimentally thanks to symmetry properties and polarization selectivity.
We observe that the presence of the vibration in the sample modulates the polarizability in phase with the phonon. Consequently, the refractive index is modified and so the quantity of transmitted/reflected light changes over the whole spectrum.
The second is a resonant ISRS effect. We describe it classically considering the driven harmonic oscillator and moreover we formalize it in a more fundamental quantum model. Relatively to the phonon momentum, the ISRS effect can amplify (in phase) or dump (out of phase) the pump phonon oscillation. The ISRS process conserves the number of photons, therefore the energy exchange with the sample results in a modification of the pulse spectral shape. The pulse is red-shifted in the Stokes case and blue-shifted in the Anti-Stokes one.

Hence, by means of pump&probe frequency-resolved measurements we obtain a complete phase dependent characterization of the interactions between coherent phonons and ultrashort light pulses. It could be a useful tool in controlling coherent vibrational modes and designing applications involving light-matter energy exchanges.

The above discussion refers to mean-value measurements, result of many repeated single-shot measurements averaged over the stochastic fluctuations present in the single acquisition. However, the noise can carry a lot of interesting information and in order to retrieve them we introduce the *Noise Correlation Spectroscopy* (NCS).
Actually, in our configuration the ISRS process introduces correlations between the frequencies coupled by the light-vibration interaction. We investigate them performing a statistical analysis on a set of single-shot frequency-resolved intensity spectra, in order to retrieve traces of the interaction process with the sample. In detail, we calculate the correlation coefficient between intensities for all the pairs of modes within the pulse bandwidth.

We discuss the NCS obtainable results by means of numerical simulations, based on the developed theoretical models. Particular care is taken to the simulation of the type of fluctuations present on the source

pulse. In fact the outcome is deeply relating on the noise properties.
The most interesting result is that a noise characterised by fluctuations localized over narrow regions of the bandwidth permits to obtain a clear measure of the vibrational energy. Precisely, the correlation width of the involved fluctuations defines the energy resolution of a NCS spectrometer.
Preliminary test measurements of both source and ISRS correlations are performed. The results are in agreement with simulations. The experimental proof of NCS capabilities is not completed here because the employed source, due to the high laser coherence, lacks a sufficiently large component of short-frequency correlation noise and it is dominated by long-range fluctuations. In order to achieve also this last point, we are planning to introduce the required noise shaping the incident pulse with a spatial light modulator.

If successfull, the NCS should be a very advantangeous technique. Obtaining a phonon energy spectrum with pump&probe measurements requires a time scan and its Fourier Transform. It can also be obtained at a fixed time, scanning the energy difference between two coupling input fields. In the last setting, though, the energy resolution is limited by the pulse bandwidth and so this last approach is unsuitable for ultrafast studies. NCS instead should allow to acquire a complete Raman spectrum at fixed time with both high time and energy resolution. In fact, the broad frequency spectrum of an ultrashort pulse is no more a restriction, because NCS is able to extract the information inside it. The only practical limitation could regard the number of repetitions to acquire to have a good statistics and a sufficiently high repetition rate to allow fast acquisition times.
Furthemore, we underline that the NCS approach has a very general character. It can be extended to virtually all non-linear optics techniques and, most importantly, it should be viable also in static experiments, where only the first pump pulse is employed and measured. Moreover, other typologies of low-energy excitations of electronic degrees of freedom, for instance superconducting gaps could be studied. In addition, in a RIXS-like approach even electronic transitions can be analyzed. In particular the high-energy one could be adressed changing the light energy scale and employing Free Electron Laser X-rays pulses.

Appendix A

Classical Impulsively Driven Oscillator

In chapter 2, we model our pump&probe experiment considering the formalism of the classical impulsively driven harmonic oscillator.
In this case, the oscillator is the coherent phonon in the examined sample. The ultrashort laser pulses exert a force on the system, which can excite, amplify or dump the phonon oscillation.

In this appendix, we treat the general formalism of an harmonic oscillator driven for a short time by a sinusoidal force. The detailed discussion of how an ultrashort pulse can set up a force of this kind is presented in 2.1.1. Here the goal is to obtain an expression for the phonon mode after the interaction with the impulsive force. The result is obtained as a function of the phonon initial conditions and, obviously, of the force properties. In particular, attention is paid to the phase difference between force and phonon.

The starting point is the differential equation of the driven harmonic oscillator:

$$\ddot{Q}(t) + \omega_{res}^2 Q(t) = F(t) \tag{A.1}$$

where $Q(t)$ is the amplitude of the oscillator as a function of time, ω_{res} is its proper frequency and $F(t)$ is the driving force. We set as initial conditions, at a time t_i, the properties relative to the maximum elongation: $Q(t = t_i) = Q_0,\ \dot{Q}(t_i) = 0$. Making use of Green's functions [6] we can solve the differential equation and find the solution

$$Q(t) = Q_0 \cos(\omega_{res}(t - t_i)) + \int_0^\tau dt' \frac{\sin(\omega_{res}(t - t'))}{\omega_{res}} F(t'). \tag{A.2}$$

In our analysis the force is impulsively applied only for a short time, corresponding to the pulse duration, τ. Hence, a sinusoidal force of

frequency ω_f and phase ϕ_f can be expressed as follows.

$$F(t) = \begin{cases} 0, & t_i < t < 0 \\ f\sin(\omega_f t + \phi_f), & 0 < t < \tau \\ 0, & \tau < t < t_f \end{cases} \tag{A.3}$$

Inserting the above expression in the differential equation solution we obtain

$$\begin{aligned} Q(t) &= Q_0\cos(\omega_{res}(t-t_i)) + \int_0^\tau dt' \frac{\sin(\omega_{res}(t-t'))}{\omega_{res}} F(t') = \\ &= Q_0\cos(\omega_{res}(t-t_i)) + \int_0^\tau dt' \frac{\sin(\omega_{res}(t-t'))}{\omega_{res}} f\sin(\omega_f t' + \phi_f). \end{aligned} \tag{A.4}$$

Solving the integral in the last term, it results

$$\begin{aligned} -\frac{f}{2\omega_{res}}\int_0^\tau dt'[\cos((\omega_f-\omega_{res})t' + \omega_{res}t + \phi_f) - \cos((\omega_f+\omega_{res})t' - \omega_{res}t + \phi_f)] = \\ = -\frac{[\sin((\omega_f-\omega_{res})\tau + \omega_{res}t + \phi_f) - \sin(+\omega_{res}t + \phi_f)]}{\omega_f - \omega_{res}} + \\ + \frac{[\sin((\omega_f+\omega_{res})\tau - \omega_{res}t + \phi_f) - \sin(-\omega_{res}t + \phi_f)]}{\omega_f + \omega_{res}}. \end{aligned} \tag{A.5}$$

The most effective regime is the resonant one, when the force has the proper frequency of the oscillator. That means when $\omega_f = \omega_{res}$. With this condition the above expression becomes

$$\begin{aligned} Q(t) = Q_0\cos(\omega_{res}(t-t_i)) - \frac{\tau f}{2\omega_{res}}\cos(\omega_{res}t + \phi_f) + \\ + \frac{[\sin(2\omega_{res}\tau - \omega_{res}t + \phi_f) - \sin(-\omega_{res}t + \phi_f)]}{2\omega_{res}}. \end{aligned} \tag{A.6}$$

It is reasonable to suppose that the force rises and vanishes continuously. So we make the assumption that $\sin(\phi_f) = \sin(\omega_f\tau + \phi_f) = 0$. This results in the conditions $\phi_f = n\pi$ and $\tau = n\frac{\pi}{\omega_{res}}$. Considering the latter, the third term in the phonon amplitude equation simplifies. So we are left with

$$Q(t) = Q_0\cos(\omega_{res}(t-t_i)) - \frac{\tau f}{2\omega_{res}}\cos(\omega_{res}t + \phi_f). \tag{A.7}$$

Now, we want to obtain this expression as a function of a single cosine. Through calculation in the complex plane it can be demonstrated that

the following relation holds.

$$a\cos(x+\phi_a) - b\cos(x+\phi_b) = \\ = \sqrt{(a-b)^2 + 4ab\sin^2(\frac{\phi_a-\phi_b}{2})}\cos\Big(x + \frac{\phi_a+\phi_b}{2} + \arctan(\frac{a+b}{a-b}\tan(\frac{\phi_a-\phi_b}{2}))\Big). \tag{A.8}$$

Applying it to our case leads to the final expression

$$Q(t) = \sqrt{(Q_0 - \frac{\tau f}{2\omega_{res}})^2 + 2\frac{Q_0 f\tau}{\omega_{res}}\sin^2(\frac{-\omega_{res}t_i - \phi_f}{2})}\cos\Big(\omega_{res}t + \Phi\Big) \tag{A.9}$$

where we defined Φ the new phase of the phonon field. We remind that we wrote the phonon as a cosine and the force as a sine. It is useful to consider the $\pi/2$ shift involved ($\sin(x) = \cos(x - \pi/2)$) and rewrite the solution as a function of the their effective phase difference $\Delta\phi = -\omega_{res}t_i - \phi_f + \pi/2$.

$$Q(t) = \sqrt{(Q_0 - \frac{\tau f}{2\omega_{res}})^2 + \frac{Q_0 f\tau}{\omega_{res}}\Big(1 - \sin(\Delta\phi)\Big)}\cos\Big(\omega_{res}t + \Phi\Big) \tag{A.10}$$

In conclusion, we obtained that after the interaction the oscillator still evolves at its proper frequency, but its amplitude changes as a function of the applied force. Particularly interesting is the dependence on the force phase.
We observe that the maximum amplification happens when $\Delta\phi = -\pi/2$. Instead, for $\Delta\phi = +\pi/2$ there is a maximum dumping. It means that the energy exchange between them is most effective when they are $\pi/2$ shifted. Therefore, the driving force is more effective when in phase with the oscillation velocity.

Riassunto

In questa tesi, si esplorano le possibilità offerte da tecniche di spettroscopia ultraveloce risolta in tempo per lo studio di eccitazioni di bassa energia. Si presta particolare attenzione ai processi di interazione radiazione-materia riguardanti impulsi ultracorti. Si sviluppano specifici modelli teorici e conducono esperimenti con tecniche risolte in tempo e la proposta "spettroscopia a correlazione di fluttuazioni" (*Noise Correlation Spectroscopy*). In dettaglio, si esamina un campione di quarzo, di cui si studiano le eccitazioni vibrazionali coerenti. L'apparato sperimentale impiegato consente di effettuare misure di pompa-sonda risolte in frequenza ed è stato appositamente realizzato presso il laboratorio *T-Rex*, Elettra-Sincrotrone Trieste.
Gli impulsi ultracorti hanno durata inferiore al picosecondo. Come conseguenza del principio di indeterminazione di Heisenberg, a questi tempi ridotti corrisponde un largo spettro di modi della radiazione. In questo studio tali proprietà ricoprono un ruolo determinante:

- La breve durata dell'impulso permette una elevata risoluzione temporale. Ciò permette di distinguere le diverse fasi all'interno di un periodo di oscillazione della vibrazione coerente, che ha frequenza dell'ordine dei TeraHertz (THz).

- L'estesa larghezza spettrale dell'impulso consente l'eccitazione stimolata delle vibrazioni, grazie all'accoppiamento di fotoni la cui differenza in frequenza corrisponde a quella del fonone, ovvero il processo di Raman Impulsato Stimolato.

- La possibilità di effettuare misure dello spettro risolte in frequenza offre un ulteriore utile parametro.

- Si può effettuare un'analisi statistica delle correlazioni all'interno dello spettro multimodo su misure ripetute di singolo impulso. In questo modo, attraverso la "Spettroscopia a correlazione di fluttuazioni" è possibile ottenere informazioni spettroscopiche sull'interazione fotone-fonone in modo innovativo e vantaggioso.

Nel caso considerato, il processo di interazione radiazione-materia rilevante è lo Scattering Raman Impulsato Stimolato (ISRS). Esso è impiegato per pompare i fononi nel campione e succesivamente sondare la risposta dinamica del sistema alla frequenza del fonone eccitato. Effettuare una misura risolta nell'energia della sonda, permette di distinguere la fase del segnale oscillante relativa a ciascun modo fononico. In particolare si osserva che regioni dello spettro distinte possono avere una diversa fase di oscillazione. Grazie a ciò si possono classificare due effetti principali.

Dal punto di vista teorico, questi sono descritti sviluppando sia un modello classico che uno quantistico. Sperimentalmente sono rivelati separatamente sfruttando le particolari proprietà di simmetria del campione e la possibilità di effettuare misure in funzione della polarizzazione. Si osserva che la presenza della vibrazione nel campione modula la polarizzabilità in fase con la posizione media del fonone. Di conseguenza, l'indice di rifrazione è modificato e così cambia la quantità di luce trasmessa/riflessa.
Il secondo effetto è un ISRS di tipo risonante. La sua descrizione classica prevede l'adozione del modello dell'oscillatore armonico forzato, il quale viene anche formalizzato in termini quantistici. In riferimento al momento del fonone, l'ISRS può amplificare (in fase) o smorzare (opposizione di fase) l'oscillazione fononica causata dalla pompa. Il processo ISRS conserva il numero di fotoni, perciò lo scambio di energia con il campione risulta in una modificazione del profilo di intensità dell'impulso. Esso è spostato verso le basse frequenze nel caso di processo Stokes, verso le alte frequenze nel caso Anti-Stokes.
Riepilogando, attraverso misure di pompa-sonda risolte in frequenza si ottiene una caratterizzazione completa in termini di fase della interazione tra fononi coerenti e impulsi di luce ultracorti. Essa può fornire un importante riferimento per controllare i modi vibrazionali coerenti e progettare applicazioni riguardanti scambi energetici tra luce e materia.

La discussione precedente fa riferimento a misure risultato della media di molte ripetizioni di singolo impulso. In questo modo vengono ripulite le fluttuazioni stocastiche presenti nella singola acquisizione. Tuttavia nel rumore si nascondono molte informazioni interessanti e la loro ricerca è lo scopo della "Spettroscopia a correlazione di fluttuazioni" (*Noise Correlation Spectroscopy*, NCS). Infatti il processo ISRS introduce correlazioni tra le frequenze accoppiate dalla interazione radiazione-vibrazione. Esse sono studiate attraverso un'analisi statistica di misure ripetute dello spettro di intensità di singolo impulso e risolte in frequenza. L'obiettivo è ottenere tracce dell'interazione con il campione. In dettaglio si calcola

il coefficiente di correlazione tra le intensità di ogni coppia di modi contenuta all'interno della larghezza spettrale dell'impulso.
Nella tesi si discutono i risultati ottenibili con misure NCS effettuando simulazioni basate sui modelli teorici sviluppati. Particolare attenzione è data alla simulazione delle tipologie di fluttuazioni presenti nell'impulso incidente. Difatti l'esito della misura è profondamente legato alle proprietà del rumore.
Il risultato più interessante è che un rumore caratterizzato da fluttuazioni localizzate attorno a ridotte regioni dello spettro permette di ottenere una chiara indicazione dell'energia vibrazionale. Precisamente la lunghezza di correlazione delle fluttuazioni considerate definisce la risoluzione in energia di uno spettrometro NCS.
Dal punto di vista sperimentale si effettuano misure preliminari per la verifica delle correlazioni previste sia dell'impulso sorgente che di quello interagente con il campione. I risultati sono in accordo con le simulazioni, anche se non è stato ancora possibile provare la configurazione di rumore più promettente. Data l'elevata coerenza della sorgente laser impiegata, le fluttuazioni presenti nell'impulso incidente sono correlate su molte frequenze e la componente di rumore con correlazione su piccola scala non è sufficiente per fornire un segnale distinguibile. Per risolvere questo problema si sta preparando la possibilità di introdurre il rumore con le giuste caratteristiche modificando il profilo di intensità dell'impulso con un modulatore spettrale.
Se il progetto avrà successo, NCS potrebbe davvero risultare una tecnica molto vantaggiosa. Infatti, ottenere uno spettro energetico dei fononi con misure di pompa-sonda richiede una scansione temporale e la sua trasformata di Fourier. Può altrimenti essere acquisito a un ritardo di pompa-sonda fissato scansionando la differenza in energia tra due campi in ingresso. In quest'ultima configurazione, tuttavia, la risoluzione energetica è limitata dalla larghezza spettrale dell'impulso e pertanto questo approccio è inappropriato per studi con impulsi ultracorti. NCS invece dovrebbe garantire la possibilità di ricavare uno spettro Raman a un tempo fissato e con alta risoluzione sia energetica che temporale. L'ampio spettro di frequenze non è più una restrizione perchè NCS è in grado di estrarre informazioni al suo interno. L'unico limite pratico potrebbe riguardare il numero di ripetizioni da acquisire per collezionare una statistica sufficiente con la rapidità necessaria alla particolare configurazione considerata.
Si sottolinea come la NCS proposta abbia un carattere molto generale. Infatti può essere virtualmente estesa a tutte le tecniche di ottica nonlineare e, soprattutto, applicata anche in esperimenti statici, nei quali un singolo impulso è impiegato e misurato. Inoltre possono essere analizzate

varie tipologie di eccitazione a bassa energia di gradi libertà elettronici, come ad esempio le gap superconduttive. Con un approccio di tipo RIXS potrebbero essere studiate anche le transizioni elettroniche. Sarebbe possibile considerare anche quelle di alta energia, modificando la lunghezza d'onda e impiegando raggi X impulsati di sorgenti laser a elettroni liberi (FEL).

Bibliography

[1] K.G. Nakamura et al., *Spectrally resolved detection in transient-reflectivity measurements of coherent optical phonons in diamond*, Physical Review B 94, 024303 (2016).

[2] E.O. Potma, S. Mukamel, *Theory of Coherent Raman Scattering*, *Coherent Raman Scattering Microscopy*, Ch.1, edited by J.X. Cheng and X.S. Xie, (CRC press, Boca Raton, 2013).

[3] X. G. Xu, S. O. Konorov, J. W. Hepburn, V. Milner, *Noise autocorrelation spectroscopy with coherent Raman scattering*, Nature Physics 4, 125 - 129 (2008).

[4] N. Rohringer, V. Kimberg, *Stochastic stimulated electronic x-ray Raman spectroscopy*, Structural Dynamics 3, 034101 (2016).

[5] C. Weninger, N. Rohringer, *Stimulated resonant x-ray Raman scattering with incoherent radiation*, Physical Review A 88, 053421 (2013).

[6] K.E. Schmidt, *Green's functions for the driven harmonic oscillator and the wave equation*, URL: http://fermi.la.asu.edu/PHY531/hogreen/hogreen.html.

[7] W. Demtröder, *Laserspektroskopie: Grundlagen und Techniken*, 5th Ed. (Springer, 2007), sec. 11.2.

[8] URL: http://www.rp-photonics.com/consulting.html

[9] T. Rasmussen, M. Rasmussen, P. Hansen, O. Jespersen, N. Rasmussen, B. Rose. *How to Design a Miniature Raman Spectrometer*. Special Issues. Volume 30, Issue 6. (2015).

[10] J. Clark. *The structure of silicon dioxide*, URL: http://www.chemguide.co.uk/atoms/structures/giantcov.html, (2009).

[11] Scott and Porto. *Longitudinal and transverse optical lattice vibrations in quartz.* Physical Review, 161 (1967).

[12] A. Rundquist, J. Broman, D. Underwood, D. Blank, *Polarization-dependent detection of impulsive stimulated Raman scattering in α-quartz*, Journal of Modern Optics, Vol. 52, No. 17, 2501–2510 (2005).

[13] W. Nie, *Optical Nonlinearity : Phenomena, Applications, and Materials*, Advanced Materials, 5, No 7/8, (1993).

[14] J.C. Diels, W. Rudolph, *Ultrashort Laser Pulse Phenomena*, Second Edition, Academic Press, (2006).

[15] Y.X. Yan, K.A. Nelson, *Impulsive stimulated light scattering. I. General theory,*The Journal of Chemical Physics 87, 6240 (1987).

[16] Y.X. Yan, E.B. Gamble, K.A. Nelson, *Impulsive stimulated scattering: General importance in femtosecond laser pulse interactions with matter, and spectroscopic applications*, J. Chem. Phys. 83, 5391 (1985).

[17] L. Dhar, J.A. Rogers, K.A. Nelson, *Time-Resolved Vibrational Spectroscopy in the Impulsive Limit*, Chem. Rev., 94, 157-193 (1994).

[18] M.M. Wefers, H. Kawashima, K.A. Nelson, *Optical control over two-dimensional lattice vibrational trajectories in crystalline quartz*, The Journal of Chemical Physics 108, 10248 (1998).

[19] R. Righini, *Ultrafast Optical Kerr Effect in Liquids and Solids*, Science, Vol. 262, Issue 5138, pp. 1386-1390 (1993).

[20] B. Huttner, S.M. Barnett, *Quantization of the electromagnetic field in dielectrics*, Phys. Rev A, vol. 46 n. 7, 4306-4322 (1992).

[21] M. Esposito, K. Titimbo, K. Zimmermann, F. Giusti, F. Randi, D. Boschetto, F. Parmigiani, R. Floreanini, F. Benatti, D. Fausti, *Photon number statisctics uncover the fluctuations in non-equilibrium lattice dynamics*, Nature Communication, 6, 10249 (2015).

[22] T. E. Stevens, J. Kuhl, R. Merlin, *Coherent phonon generation and the two stimulated Raman tensors*, Physical Review B, 65, 144304 (2002).

[23] R. Boyd, *Nonlinear Optics*, Third Edition, Academic Press (2007).

[24] R. Merlin, *Generating coherent THz phonons with light pulses*, Solid State Communications, Voi. 102, No. 2-3, pp. 207-220 (1997).

[25] M. Esposito, *A new spectroscopic approach to collective excitations in solids: pump-probe quantum state tomography*, PhD Thesis, Unversità degli studi di Trieste (2016).

[26] G. Berruto, *Pump-probe Experiments with Ultrashort Mid-Infrared Light Pulses*, Master Thesis, Università degli Studi di Trieste (2014).

[27] R. Fowles, *Introduction to Modern Optics*, Second Edition, Dover (1975).

[28] R. G. Littlejohn, *Gaussian, SI and Other Systems of Units in Electromagnetic Theory*, (2016).

[29] A. Blason, *Teoria Quantistica dello Scattering Raman Impulsato e Stimolato*, Bachelor Thesis, Università degli Studi di Trieste (2017).

Ringraziamenti

Grazie innanzitutto al mio relatore Daniele, per la presenza costante, la fiducia dimostratami fin dall'inizio e molte altre ragioni, che non elenco perchè sarà anche stanco di leggere questa tesi.
Alla mia correlatrice Giorgia dedico un grazie mille, o forse anche più, come le ore passate insieme a lavorare su questo progetto. Davvero credo sia la persona con cui ho vissuto di più in questo 2017 e non posso che scusarmi e compatirla per questo.
Ringrazio moltissimo Francesca, Alexandre (merci beaucoup) e Jonathan (thank you so much) per tutti i consigli e gli aiuti che mi hanno dato. Mi ritengo molto fortunato a far parte di questo gruppo di ricerca. Gruppo per il quale è sempre una risorsa Martina, che ringrazio per il suo lavoro precedente e i puntuali e gentili incoraggiamenti.

Ringrazio i teorici Andrea Blason e il prof. Fabio Benatti per la collaborazione e per le discussioni toste ma sempre piacevoli.

Un grazie indispensabile va a Roberto Passuello, Fulvio Billè, al mio tutor Georgios Kourousias e a tutti coloro che ci hanno soccorso per risolvere gli innumerevoli problemi pratici del nostro esperimento. In particolare questo ringraziamento va anche a Federico Cilento, per la realizzazione dei detector e per la costante disponibilità e guida in laboratorio.

E poi, grz ai coinquilini Nicola e Giacomo, è più facile sopravvivere insieme. A proposito, grazie alle nostre famiglie per i regolari e deliziosi rifornimenti alimentari.
Ringrazio tutto il microcosmo che circonda il nostro appartamento. È un piacere migliorarsi e peggiorarsi reciprocamente. Amiche e amici, compagni di studio e di vita, grazie per tutto l'aiuto che mi date senza rendervene conto e per quello chi mi avete dato senza che io me ne accorgessi.
Ringrazio infine infinitamente tutta la mia grande famiglia, la mia sicurezza. Ancor di più mamma, papà e Martina, i principali colpevoli e vittime di quella che hanno sempre definito la mia strana forma di intelligenza.